

Nonlinear optical processes with a silica toroid microcavity for optical frequency comb generation

March 2017

A thesis submitted in partial fulfillment of the requirements for the degree
of Doctor of Philosophy in Engineering



Keio University

Graduate School of Science and Technology
School of Integrated Design Engineering

KATO, Takumi



Keio University

Graduate School of Science and Technology
School of Integrated Design Engineering

**Nonlinear optical processes with a silica toroid microcavity
for optical frequency comb generation**

by

Kato, Takumi

A THESIS SUBMITTED
IN PARTIAL FULFILLMENT OF
THE REQUIREMENTS FOR THE DEGREE
Doctor of Philosophy

APPROVED, THESIS COMMITTEE:

Tanabe, Takasumi

Kannari, Fumihiko

Tsuda, Hiroyuki

Sasada, Hiroyuki

Lončar, Marko

Abstract

Laser technology was first applied to spectroscopy and is now used in various fields including medicine and microfabrication. Since the interaction between light and matter varies with laser frequency, widely tunable lasers are desired for various applications. Frequency conversion with nonlinear optical effects usually requires a high optical pump power because second- and third-order nonlinear coefficients are small. High quality factor (high- Q) microcavity devices have attracted attentions, because they allow us to compensate for small nonlinear coefficients and achieve frequency conversion with low laser power thanks to the strong confinement of light. Recently, a microcavity-based frequency comb (microcomb) has been generated that requires only a continuous-wave pump and a high- Q microcavity to obtain an optical frequency comb, which is a key technology for precise measurements. This dissertation describes nonlinear frequency conversion in a silica toroid microcavity for generation of optical frequency combs.

Chapter 1 provides the background and motivation for this work. Frequency comb technologies and related studies that use high- Q microcavities to enhance third-order nonlinearities such as four-wave mixing (FWM), stimulated Raman scattering (SRS), and third-harmonic generation (THG) are surveyed, to clarify the motivation for this study.

Chapter 2 describes the basic theory and fabrication of a silica toroid microcavity. The experimental setups to measure the nonlinear processes with a fabricated silica toroid microcavity including FWM, SRS, and THG are described.

Chapter 3 presents a demonstration of a newly proposed method for achieving mode-locking in a microcomb system. A model based on the Lugiato-Lefever equation is developed to analyze microcomb generation, and it reveals that the hysteresis behavior of a nonlinear cavity will be the key to achieving mode-locking. In contrast to previous methods, where the frequency of the input laser is scanned, it is found numerically and experimentally that mode-locking could also be achieved by adequately sweeping the

input laser power.

Chapter 4 describes a study of the gain competition between FWM and SRS that occurs in a microcavity. Considering the free-spectral-range (FSR) in addition to an analysis of maximum gains of FWM and SRS, it is found that we can suppress or enhance the modulation instability gain by changing the input power and the coupling Q in a large FSR cavity. This will allow us to control the transition from an FWM dominant state to an SRS dominant state.

Chapter 5 discusses the transverse mode interaction that occurs as a result of SRS in a silica cavity, which has broad Raman gain. It is found that in such a system the transverse mode interaction occurs from a low- Q to a high- Q transverse mode family via an SRS process when a low- Q mode is pumped. As a result, a dual-comb-like spectrum appears. The transverse mode interaction dependence on the Q value and the spatial overlap between different transverse mode families are described numerically and experimentally.

Chapter 6 describes a demonstration of visible light emission via THG. It is shown experimentally that the FWM and SRS in the near infrared region influence the spectrum shape of the generated visible light.

Chapter 7 is a summary. The knowledge obtained in each chapter is summarized and the conclusions reached in this dissertation are presented.

Contents

1	Introduction	5
1.1	High- Q microcavity	6
1.2	Optical frequency comb	9
1.3	Four-wave mixing and Microcomb	12
1.4	Stimulated Raman scattering and Raman comb	21
1.5	Third-harmonic generation and visible comb	23
1.6	Motivation and objective of this study	24
1.7	Thesis statement and overview	26
2	Silica toroid microcavity	29
2.1	Theory of quality-factor	30
2.2	Theory of coupling between optical components	31
2.3	Theory of optical modes in silica toroid microcavity	36
2.4	Theory of optical modes in tapered fiber	40
2.5	Theory of nonlinearity	43
2.5.1	Four-wave mixing	43
2.5.2	Stimulated Raman scattering	45
2.5.3	Third-harmonic generation	46
2.6	Fabrication	46
2.6.1	Fabrication of a silica toroid microcavity	46
2.6.2	Fabrication of a tapered fiber	48
2.7	Optical measurement methods	50
2.7.1	Measurement of Q -factor	50
2.7.2	Measurement of nonlinearity	52

2.8	Summary	55
3	Hysteresis behavior of microcomb generation	57
3.1	Lugiato-Lefever equation	58
3.2	Dispersion parameters of a silica toroid microcavity	59
3.3	Hysteresis behavior of microcomb generation	60
3.4	Experimental results	67
3.5	Summary	76
4	Influence of stimulated Raman scattering on microcomb generation in a silica cavity	77
4.1	Raman scattering in silica	78
4.2	Modulation instability gain	80
4.3	Numerical simulation	82
4.4	Summary	87
5	Transverse mode interaction via stimulated Raman scattering combs in a silica toroid microcavity	91
5.1	Stimulated Raman scattering	93
5.2	Experimental results	95
5.3	Numerical simulation with a coupled Lugiato-Lefever equation . . .	101
5.4	Summary	105
6	Broad bandwidth third-harmonic generation via four-wave mixing and stimulated Raman scattering	107
6.1	Third-harmonic generation	108
6.2	Experimental results	112
6.3	Dispersive wave emission	113
6.4	Summary	116
7	Summary and outlook	119
7.1	Summary	119
7.2	Outlook	121

A Polygonal silica toroid microcavities for stable coupling	123
A.1 Polygonal cavities	123
A.2 Fabrication process	124
B Theory of optical cavity	131
B.1 Derivation of a relationship between FWHM and Q -factor	131
B.2 Theory of whispering gallery mode	136
C Derivation of Lugiato-Lefever equation	141
C.1 Nonlinear Schrödinger equation	141
C.2 Lugiato-Lefever equation	145
Acknowledgement	149
List of achievements	154
Bibliography	157

Chapter 1

Introduction

A high-quality-factor (Q) optical microcavity is an efficient platform for achieving second-order and third-order nonlinear effects at a low power emitted by a compact light source, because the optical density inside the cavity is strongly enhanced by long photon life and small mode volume¹⁾. Because third-order nonlinear efficiency is proportional to the cube of light power, a high- Q microcavity is a useful device for studying four-wave mixing (FWM)^{2,3)}, stimulated Raman scattering (SRS)⁴⁻⁷⁾, and third-harmonic generation (THG)^{8,9)}.

One of the target applications of high- Q microcavities is optical frequency comb generation^{10,11)}. An optical frequency comb is composed of a number of frequencies that are perfectly equidistantly spaced in the spectrum. This technology can contribute to many high-precision applications, including metrology and spectroscopy^{12,13)}. Conventionally, the combination of a material with broadband fluorescence and a stable optical resonator, as in a Ti:Sapphire laser, has been used to achieve multi-wavelength emissions. However, a Ti:Sapphire laser generally requires a stable, high-powered light source, a robust laboratory environment, and professional skills such as careful optical alignment. The development of erbium-doped fiber lasers¹⁴⁻¹⁶⁾ made frequency comb sources compact, but further developments are still needed to lower costs, widen the operating wavelength range, and increase the repetition rate. A high- Q microcavity-based frequency comb can meet these demands^{11,17)}.

Generation of frequency combs with a high- Q microcavity is achieved by pumping with single continuous wave. Due to the enhanced optical density inside a cavity, wavelength conversion via four-wave mixing readily occurs at a low input power, typically below 1 mW. Since low-power continuous-wave lasers of various wavelengths already exist, a microcavity-based frequency comb has the potential to be used not only in the telecom region of the spectrum, but in the visible, mid-infrared, and ultraviolet regions. The mechanism of microcavity-based frequency comb generation has been investigated since 2007, and the research has explored physics-oriented¹⁷⁻¹⁹⁾, material-oriented²⁰⁻²³⁾, and application-oriented topics²⁴⁻²⁶⁾.

This dissertation focuses on microcavity-based optical frequency comb generation. A silica toroid whispering-gallery-mode microcavity was selected as the research platform. This type of cavity exhibits ultrahigh Q (over 100 million) and can be integrated with a silicon chip. This study uses the physics of wavelength conversion in a cavity via third-order non-linearity to explain cavity-based generation of optical frequency combs.

1.1 High- Q microcavity

An optical microcavity is a micro-sized optical cavity. If the cavity length and light frequency are matched, this creates a “resonance condition” that allows the light to resonate. During resonance, the cavity confines the light for a length of time determined by the cavity loss. When a cavity is small, the volume of the confined light is small; thus, an optical microcavity confines the resonant light in a microvolume. Light packed into a small volume has a very high optical density, similar to the way a gas increases in pressure when confined in a small container. A high Q corresponds to a long light confinement time, called “photon lifetime.” This is defined as the time it takes for the light to dissipate to $1/e$ of its original intensity. A Q of 10^6 corresponds to a photon lifetime of 0.823 ns (10^{-9} s) at a wavelength of 1550 nm. When a continuous wave that satisfies the resonance

condition enters a cavity, the light reaching the cavity first and the light entering the cavity 0.823 ns later simultaneously exist in the cavity. This overlap causes a local enhancement of the optical power inside the cavity. Therefore, a high- Q microcavity has two enhancement factors. One is “micro-size,” which confines light in a small volume, and the other is “high Q ,” which allows light to be trapped for a long time. These two characteristics make a high- Q microcavity a suitable platform for demonstrating nonlinear optics that require high optical density of a material.

Three types of microcavities have been investigated so far as shown in Figure 1.1: the Fabry-Perot cavity, the photonic crystal cavity, and the ring cavity¹⁾. A simple Fabry-Perot cavity consists of two parallel mirrors that reflect light many times. This type of cavity requires mirrors with a reflectivity higher than 99%. It is not easy to fabricate such highly reflective mirrors on a small scale. One solution is a multilayer dielectric mirror coating, which has a reported reflectivity of over 99.9995%²⁷⁾. An advantage of this type is that an atom is able to couple to the cavity mode, because the space between mirrors allows electrical fields to be confined in a vacuum. However, complex measurement systems, such as highly reflective mirrors and objective lenses, are required. Recently, however, a fiber-type Fabry-Perot cavity was proposed as a simpler setup²⁸⁾. Another small Fabry-Perot-type structure is a micropillar cavity, composed of distributed Bragg reflectors²⁹⁾. In order to form Bragg reflectors, two different materials that have different refractive indices are alternately grown on a chip using molecular beam epitaxy. Then, a pillar structure with a typical diameter of less than 1 μm can be formed by using a semiconductor processing technology, such as reactive-ion etching. This style allows the integration of quantum dots in a cavity. A single-photon source has already been used with a micropillar cavity³⁰⁾.

A photonic crystal cavity confines light with Bragg reflection in the horizontal direction and total internal reflection in the vertical direction. Usually, the structure consists of a number of periodically-spaced air holes that work as Bragg mirrors^{31,32)}. The cavity can achieve an extremely small mode volume with a moderately high Q ^{33,34)}. Precise air holes are fabricated with electron-beam lithography, which achieves a fabrication accuracy of a few nanometers. Nowadays, the precision of photolithography has been improved, and a photonic crystal

cavity made with a Q of 1 million has been achieved with this method³⁵⁾.

A ring cavity consists of a ring-shaped circuit of an optical waveguide, such as a rib waveguide and a fiber. Light that satisfies the condition for resonance propagates around the cavity.

Although there are a number of studies on fiber-based ring cavities, the following sections focus on integrated ring cavities, because the main topic of this thesis is micro-sized cavities. Many materials are used for integrated ring cavities; for example, cavities with silicon^{36,37)}, silica^{20,38)}, silicon nitride^{39,40)}, aluminum nitride⁴¹⁾, and diamond²²⁾ have been reported. In contrast to cavities with distributed Bragg reflectors and photonic crystal cavities, ring cavities have a number of resonant frequencies spaced equidistantly in the spectrum. In other words, the free-spectral-range (FSR) of a ring cavity is theoretically constant. This is because the conditions for resonance require $2\pi * m$ of phase shift per round trip, where m is an integer. This characteristic is a key point for producing microcavity-based frequency combs, which I describe later.

A type of cavity similar to a ring cavity is a whispering gallery mode cavity. It has a whispering gallery mode as the resonant mode. This mode propagates along the edge of the boundary of a circular structure. It was first found by Lord Rayleigh in 1878, with respect to a sound wave at St. Paul's Cathedral⁴²⁾. Forty years after Rayleigh's discovery, it was found that the theory can be applied to a light wave that is guided along a boundary edge with total internal reflection⁴³⁾. A whispering gallery mode exhibits very high Q when the surface of a circular structure is smooth, because the total internal reflection is analytically lossless. To achieve this attractive high- Q cavity, droplet cavities, with a smooth boundary due to surface tension, have been researched for applications such as micro-lasers. However, the material of a droplet itself has absorption. For example, the Q of a droplet made from water is limited to 1 million at the telecom. In 1989, Braginsky et al. proposed a whispering gallery mode cavity with low absorption made from fused silica⁴⁴⁾, which is fabricated by melting a common single-mode silica fiber. The cavity exhibits a Q of higher than 100 million, and it paves the way for use of nonlinear optics with low-power lasers.

High- Q whispering gallery mode cavities have been studied as platforms for demonstrating nonlinear optics for the last twenty years. There are cavities made

from silica⁷⁾, calcium fluoride⁴⁵⁾, and magnesium fluoride⁴⁶⁾. Among them, the silica toroid microcavity is of particular interest because it exhibits a Q of higher than 100 million and can be integrated with a silicon chip. This cavity was proposed by Armani et al. in 2003 and some demonstrations of nonlinear optical effects have been reported^{47,48)}.

In this dissertation, “microcavity” will refer to a ring cavity or a whispering gallery mode cavity.

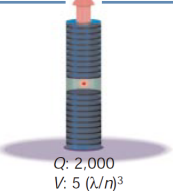
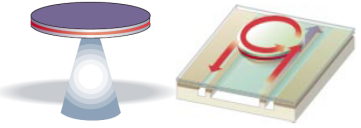
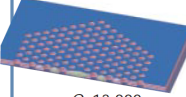
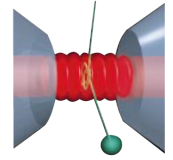
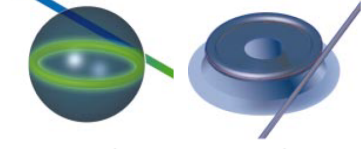
	Fabry-Perot	Whispering gallery	Photonic crystal
High Q	 <p>$Q: 2,000$ $V: 5 (\lambda/n)^3$</p>	 <p>$Q: 12,000$ $V: 6 (\lambda/n)^3$</p> <p>$Q_{III-V}: 7,000$ $Q_{Poly}: 1.3 \times 10^5$</p>	 <p>$Q: 13,000$ $V: 1.2 (\lambda/n)^3$</p>
Ultrahigh Q	 <p>$F: 4.8 \times 10^5$ $V: 1.690 \mu\text{m}^3$</p>	 <p>$Q: 8 \times 10^9$ $V: 3,000 \mu\text{m}^3$</p> <p>$Q: 10^8$</p>	

Fig. 1.1: Performance of several microcavities.

The microcavities are organized by column according to the confinement method used and by row according to high Q and ultrahigh Q . [K. Vahala, *Nature* **424**, 839-846 (2003). The figure is used with permission from Nature Publishing Group.]

1.2 Optical frequency comb

Optical frequency comb technology was developed by J. L. Hall and T. W. Hänsch in the 1990s^{49,50)}, and they won the Nobel prize in Physics in 2005. An optical frequency comb is a set of optical frequencies spaced perfectly equidistantly in the frequency domain¹²⁾. Strictly speaking, the phase of each frequency component should be locked. Thus, the relationship between the spectrum and the temporal waveform is described as in Figure 1.2. This set of lights is the most precise tool for optical measurements, spectroscopy, metrology, and optical communications.

The first frequency comb was demonstrated with a mode-locked Ti:Sapphire laser, which emits a transform-limited pulse train with a fixed repetition rate that

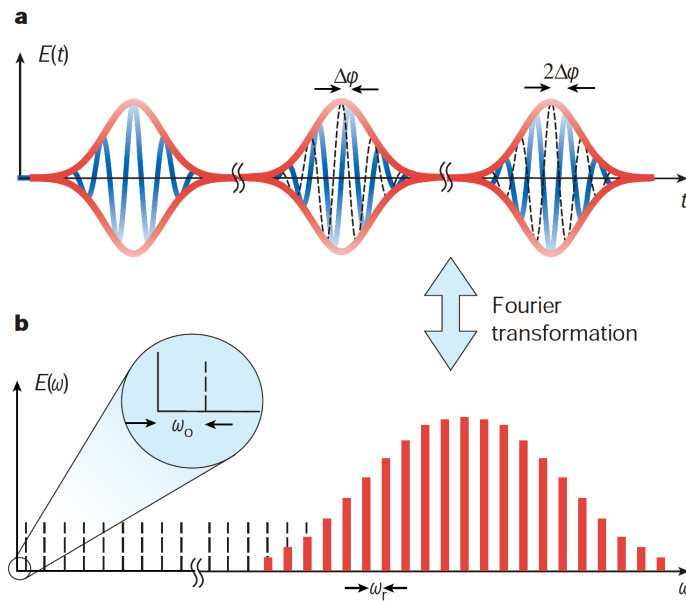


Fig. 1.2: Optical frequency comb.

a, b Consecutive pulses of the pulse train emitted by a mode-locked laser and the corresponding spectrum. In the frequency domain, the components are spaced equidistantly at intervals of ω_r . The ω_o is a carrier-envelope-offset relating to a phase shift $\Delta\phi$ of each pulse in the time domain. [Th. Udem, R. Holzwarth, and T. W. Hänsch, *Nature* **416**, 233-237 (2002). The figure is used with permission from Nature Publishing Group.]

corresponds to cavity length. When mode-locking is achieved, frequency components of the pulse train are equidistant in the frequency domain and have a flat phase relationship. If one of the frequency components is locked, a kind of atomic clock assures an absolute number of frequencies, so one can estimate absolute frequencies of other comb lines because they are spaced equidistantly. Before frequency combs emerged, very complex components were required to get an absolute frequency from a specific optical clock, such as a cesium atomic clock. In contrast, since the emergence of the frequency comb, only a Ti:Sapphire laser, an optical clock, and a few nonlinear media are required for absolute frequency measurements. Figure 1.3 shows the first direct radio frequency-optical frequency conversion using a Ti:Sapphire laser. The setup requires a methane-stabilized He-Ne laser, a Ti:Sapphire laser, and three nonlinear crystals for frequency doubling, as well as an optical frequency interval divider, to achieve a stabilized 486-nm output for the absolute frequency measurement of hydrogen 1S-2S two-photon resonance. Compared to the conventional frequency chain, the setup has become remarkably simple¹²⁾.

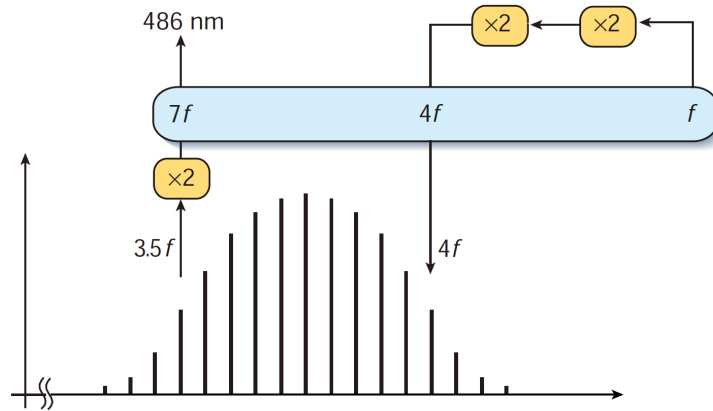


Fig. 1.3: The first direct radio frequency-optical frequency conversion using a Ti:Sapphire laser. An optical interval divider (blue box) fixes the frequency ratios to precisely $7f : 4f : f$. f is a reference value from a methane-stabilized He-Ne laser ($3.39 \mu\text{m}$). The frequency comb fixes the interval $4f - 3.5f = 0.5f$. [Th. Udem, R. Holzwarth, and T. W. Hänsch, *Nature* **416**, 233-237 (2002). The figure is used with permission from Nature Publishing Group.]

In 2000, a valuable method called the f - $2f$ self-reference method was proposed, which eliminates the necessity of some nonlinear crystals and even an optical fre-

quency interval divider^{49,50}). It was made possible by the development of a photonic crystal fiber as a method of spectral broadening. In the first demonstration, a 25-fs pulse train with a repetition rate of 625 MHz emitted from a Ti:Sapphire laser propagates in a photonic crystal fiber, which exhibits a high nonlinear coefficient. As a result, the spectrum becomes an octave (532–1064 nm). Comparison between doubling frequency of the red part of the spectrum and the blue part of the spectrum provides a carrier-envelope-offset ω_o of the frequency comb. With a frequency lock of two parameters, ω_o and the repetition rate ω_r , a stable frequency comb is obtained. The setup of this comb requires space on one optical bench.

Nowadays, frequency combs are researched with respect to not only a Ti:Sapphire laser but also a fiber laser that is much simpler than the former. The fiber lasers do away with expensive setup and the necessity for professional laser skills, because they are robust against external noise^{14–16}). Thus, fiber-based frequency combs are currently common for precise measurements. Today, a microcavity-based frequency comb¹¹) is expected to be the next new type of frequency comb. The advantages over conventional combs are as follows:

1. high repetition rate of a pulse train (large free-spectral-range),
2. elimination of complex components,
3. low fabrication cost,
4. tunability of the center frequency of a frequency comb.

Concrete explanations of microcavity-based frequency combs appear in next parts.

1.3 Four-wave mixing and Microcomb

Among nonlinear optical effects, four-wave mixing derived from third-order nonlinearity is key for microcavity-based frequency combs. The combs are called “microcombs” or “Kerr combs,” and a number of researchers have achieved their manufacture. The basic experimental setup is simple; it requires a continuous-wave laser and a microcavity connected to an optical waveguide. From single wavelength input, a microcomb occurs via four-wave mixing^{3,10}) as described in

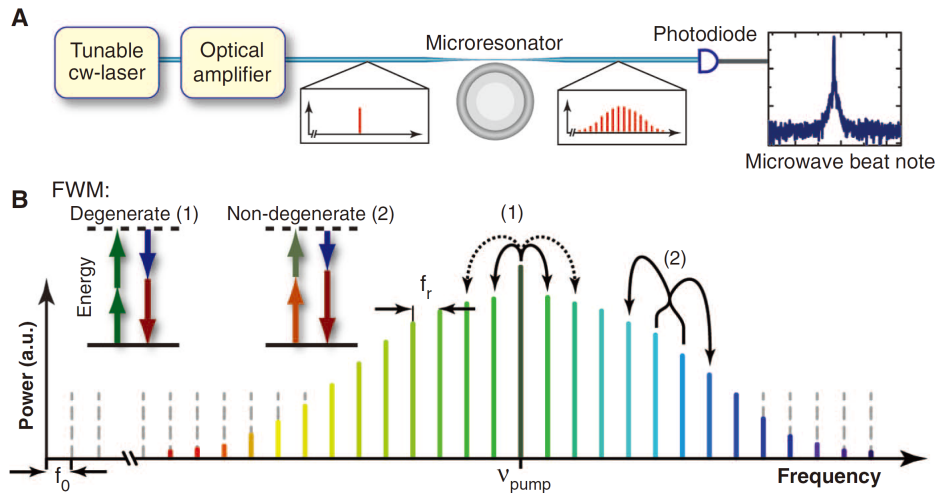


Fig. 1.4: Principle of optical frequency comb generation using optical microresonators. (A) An optical microresonator (here, a silica toroid microresonator) is pumped with a CW laser beam. The high intensity in the resonators (GW/cm^2) gives rise to a parametric frequency conversion through both degenerate and nondegenerate (i.e., cascaded) FWM. Upon generation of an optical frequency comb, the resulting beatnote (given by the inverse cavity round-trip time) can be recorded on a photodiode and used for further stabilization or directly in applications. (B) Optical frequency comb spectrum, which is characterized by the repetition rate (f_r) and the carrier envelope frequency (f_0). In the case of a microresonator-based frequency comb, the pump laser is part of the optical comb. The comb is generated by a combination of degenerate FWM (process 1, which converts two photons of the same frequency into a frequency upshifted and downshifted pair of photons) and nondegenerate FWM (process 2, in which all four photons have different frequencies). The dotted lines indicate degenerate FWM into resonator modes that differ by more than one mode number. The presence of cascaded FWM is the underlying process that couples the phases of all modes in the comb and allows transfer of the equidistant mode spacing across the entire comb. [T. Kippenberg, R. Holzwarth, and S. A. Diddams, *Science* **332**, 555-559 (2011). The figure is used with permission from The American Association for the Advancement of Science.]

Figure 1.4. The mechanism is explained by analogy with a modulation instability in fibers⁵¹⁾. When a fiber exhibits anomalous dispersion at a particular wavelength, a propagating pulse is modulated with third-order nonlinearity. This is because phase matching is induced by a balance between the phase shift of the anomalous dispersion and that of a Kerr effect. The modulation indicates a wavelength conversion. For a microcomb, the wavelength conversion occurs even though the laser input is not a pulse, because a microcavity enhances the optical power inside by as much as the peak power of a pulse that provides a large enough Kerr effect.

Since the 1990s, there have been a number of studies on wavelength conversion itself with high- Q microcavities. However, it has been difficult to specify what kinds of nonlinear effects contribute. In 2004, Kippenberg *et al.* reported pure optical parametric oscillation in a silica toroid microcavity³⁾. They mentioned that four-wave mixing and stimulated Raman scattering compete, and two parameters, a cavity detuning and a coupling efficiency between a cavity and a waveguide, control the competition. This is because how phase matching is satisfied largely influences the threshold power of four-wave mixing, whereas stimulated Raman scattering does not require phase matching. Since four-wave mixing is a completely coherent process, this research made the first step toward mode-locking of the microcomb.

In 2007, Del’Haye *et al.* introduced the concept of a microcomb with a silica toroid microcavity¹⁰⁾. They indicated that the frequency lines of a microcomb are stable enough to use for frequency metrology. Based on this proposal, intensive microcomb research has been done with silica toroids^{18,52)}, silica microspheres^{53,54)}, silicon nitride rings^{21,55)}, and others^{56,57)}. In 2011, Ferdous *et al.* proved that there are two states in the microcomb: one is a tightly coherent state, and the other is noisy⁵⁸⁾. Subsequent research¹⁹⁾ revealed that the difference between the two states derives from the evolution of the combs, as shown in Figure 1.5. A high-phase noise state is caused by different offsets of secondary combs, which are evolved from primary combs that are the first generation from a pump mode. Each primary comb line has slightly different dispersion, so that secondary comb lines don’t match with each other. The different offsets emerge as high-phase noise in radio frequencies. On the other hand, when the primary combs occur

next to the pump, all of the comb lines have the same offsets, as shown in Figure 1.5(b). State 2 indicates coherence, which can be used in practical applications. Radio frequency measurement is a simple way to assess the state of the comb.

Further research found that Turing patterns and cavity soliton states are in low-phase noise states, and a chaotic state exhibits high-phase noise. The Turing pattern is a state indicated by a periodic modulation in the temporal domain, with effectively blue detuning of the input. In a cavity soliton state with effectively red detuning, one soliton (or multiple solitons) propagates in the cavity, which is the same as mode-locking. It requires a balance between the phase shift of the anomalous dispersion and that of a Kerr effect. Thus, the engineering of a cavity dispersion is needed to achieve a mode-locked microcomb¹⁷⁾. The way to access a mode-locked microcomb has been researched experimentally¹⁷⁾, theoretically⁵⁹⁾, and numerically^{60–63)}. A simple method is a wavelength scan from blue to red detuning of an input laser, which follows the resonant wavelength shift derived from a Kerr effect and a thermo-optic effect⁶⁴⁾. The intracavity power gradually becomes large, and the detuning of the input laser finally reaches effectively red detuning. The excitation at which intracavity power is gradually changed from zero to a particular threshold value is called soft excitation⁶⁵⁾, and it is the most common way to produce a mode-locked microcomb. Recently, a method of control of the thermo-optic effect with a microheater⁶⁶⁾ was proposed. This method is useful because there is not always a tunable laser in the desired wavelength region, such as mid-infrared.

Frequency locking of a microcomb, such as f - $2f$ self-reference interference, is still desired. Despite much research on dispersion engineering, the spectrum of a mode-locked microcomb itself does not reach an octave. As the spectrum emitted by a Ti:Sapphire laser broadens, an octave microcomb is achieved with a highly nonlinear fiber. Recently, f - $2f$ and $2f$ - $3f$ self-reference methods have been demonstrated^{67,68)}. Thus, a microcomb can obtain the same capacity as a frequency comb source. However, some additional components are required, which eliminates the advantage of a microcomb that requires a simple setup. Thus, generation of an octave-spanning microcomb is still one of the most attractive topics in microcomb research.

Not only telecom-range, but also visible- and mid-infrared-range microcombs

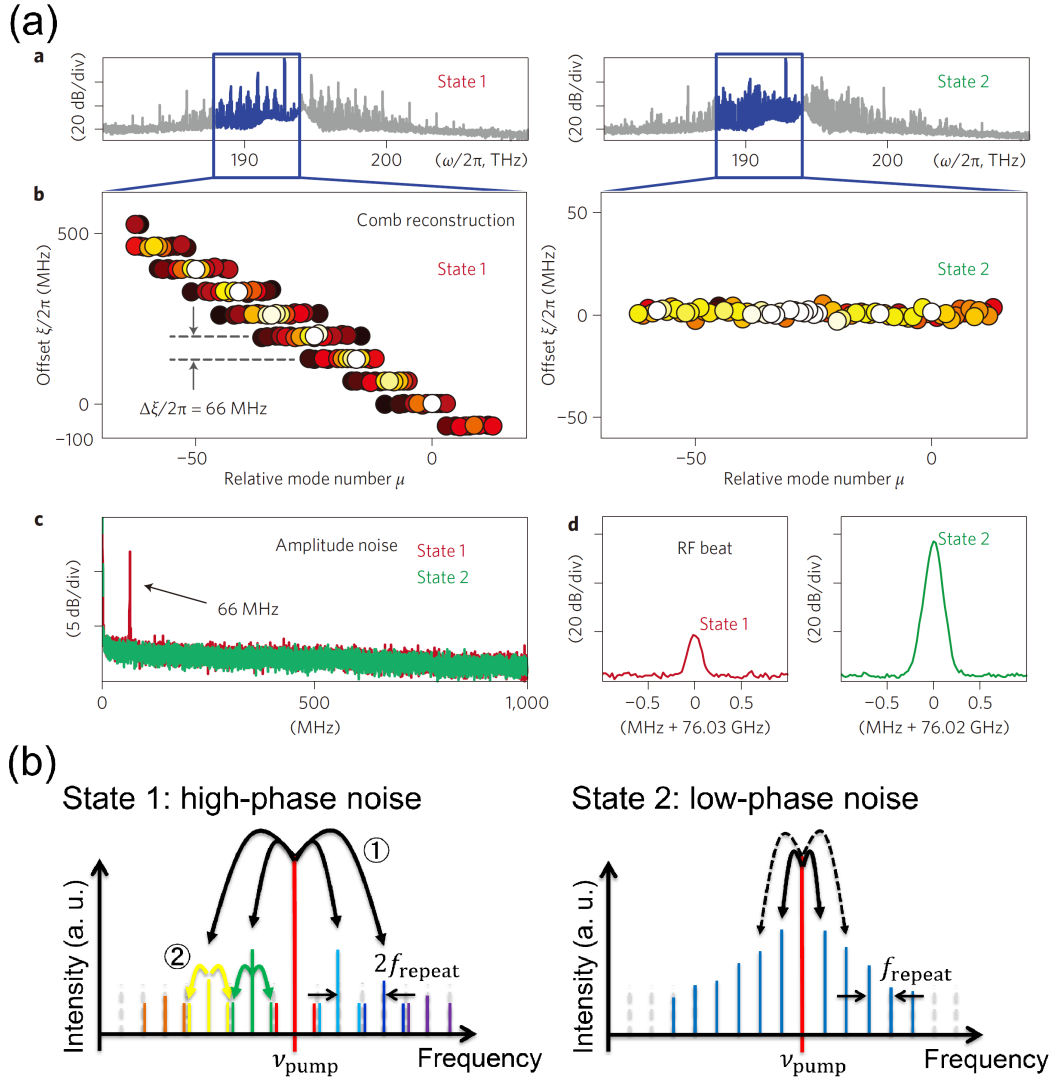


Fig. 1.5: (a) Transition to a low-phase-noise Kerr comb. a, Optical spectra of microresonator comb states 1 and 2 (pump power = 6 W) in a Si_3N_4 resonator. State 2 evolves from State 1 when reducing the detuning of the pump laser. b, A transition is observed from multiple subcombs to a single (sub)comb over the bandwidth of the Kerr comb reconstruction. In State 1, all subcombs have the same mode spacing, but have different offsets ξ , which differ by a constant relative amount of $\Delta\xi/2\pi = 66 \text{ MHz}$. c, In the transition from State 1 to State 2, the amplitude noise peak resulting from the beating between overlapping offset subcombs disappears (resolution bandwidth RBW = 300 kHz) d, The RF beat note shifts by $\sim 10 \text{ MHz}$ and the signal-to-noise ratio increases (RBW = 100 kHz). (b) Evolution of optical spectra, state 1 and 2. State 1 exhibits high-phase noise derived from a difference of offsets of secondary combs which generate from each primary comb line (2-FSR combs in this case). The optical spectrum of State 2 exhibits low-phase noise because all comb lines are directly generated from a pump. [(a) T. Herr, K. Hartinger, J. Riemensberger, C. Y. Wang, E. Gavartin, R. Holzwarth, M. L. Gorodetsky, and T. J. Kippenberg, *Nature Photonics* **6**, 480-487 (2012). The figure is used with permission from Nature Publishing Group.]

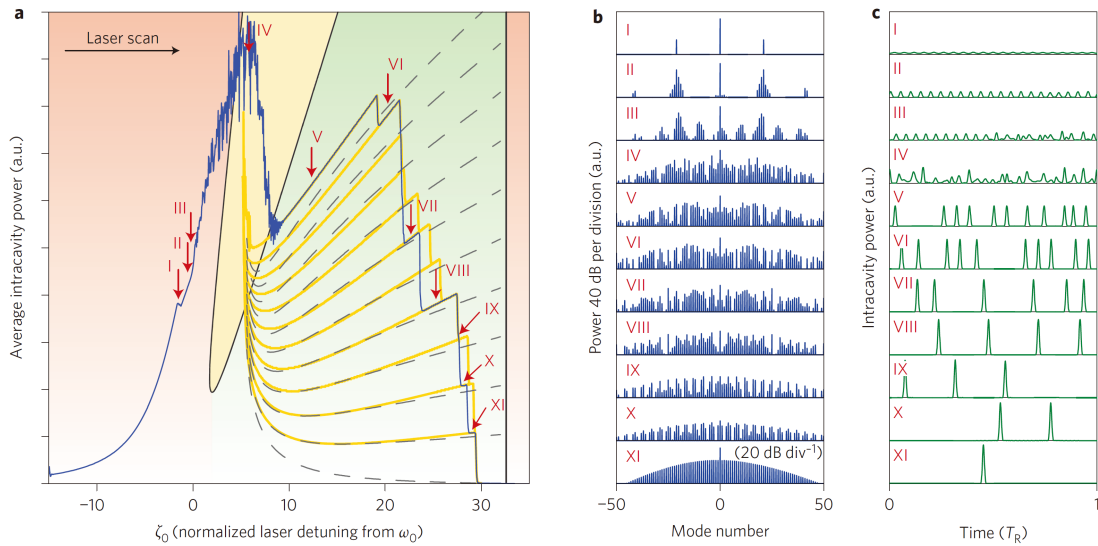


Fig. 1.6: Numerical simulations of soliton formation in a microresonator.

a, Average intracavity power (blue line corresponds to the transmission signal for a microcavity with side coupling system.) during a simulated laser scan (101 simulated modes) over a resonance in a MgF_2 resonator. The step features are well reproduced. The orange lines trace out all possible evolutions of the system during the scan. The dashed lines show an analytical description of the steps. The green area corresponds to the area in which solitons can exist, the yellow area allows for breather solitons with a time-variable envelope; solitons cannot exist in the red area. b,c, Optical spectra and intracavity powers for the different positions I–XI in the laser scan.. [T. Herr, V. Brasch, J. D. Jost, C. Y. Wang, N. M. Kondratiev, M. L. Gorodetsky, and T. J. Kippenberg, *Nature Photonics* **8**, 145-152 (2014). The figure is used with permission from Nature Publishing Group.]

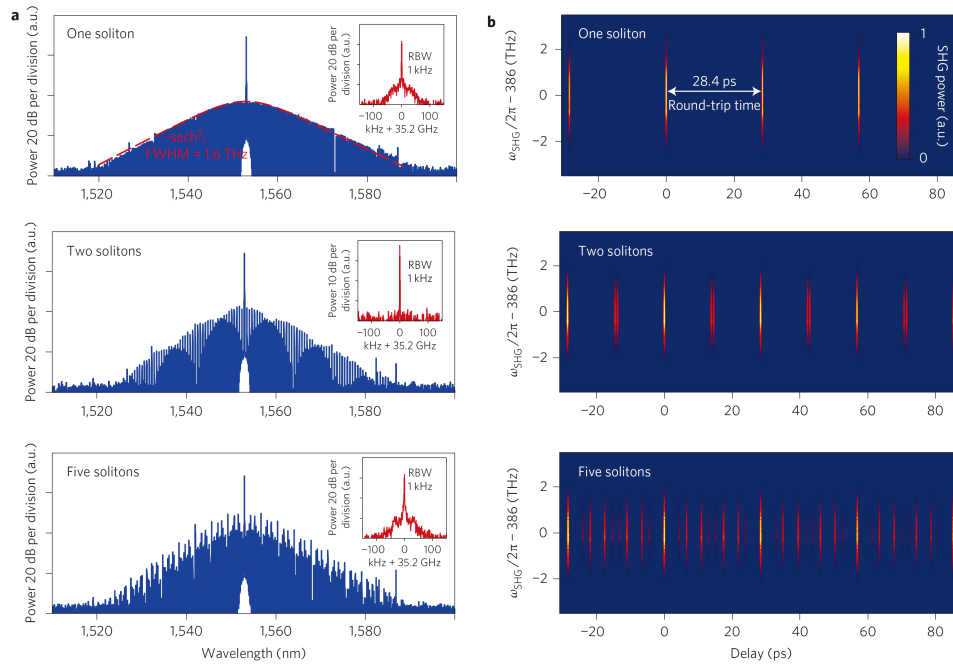


Fig. 1.7: a, Optical spectra of three selected states with one, two and five solitons, respectively. The insets show the RF beatnote, which is resolution-bandwidth limited to a 1 kHz width in all cases. The dashed red line in the optical spectrum of the one-pulse state shows the spectral sech² envelope expected for solitons with a 3 dB bandwidth of 1.6 THz. b, FROG traces of the states in a that display the signal of the single and multiple pulses. [T. Herr, V. Brasch, J. D. Jost, C. Y. Wang, N. M. Kondratiev, M. L. Gorodetsky, and T. J. Kippenberg, *Nature Photonics* **8**, 145-152 (2014). The figure is used with permission from Nature Publishing Group.]

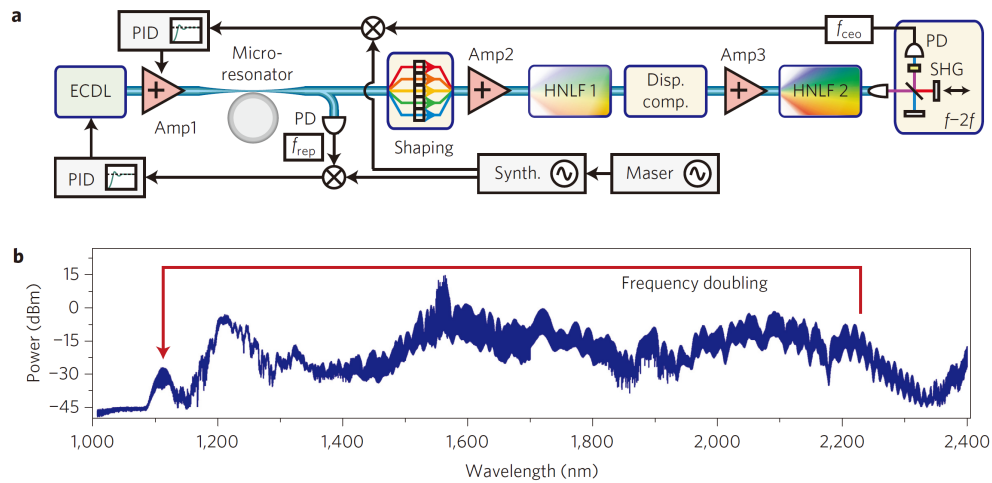


Fig. 1.8: Experimental setup for $f - 2f$ self-referencing of a microcomb.

a, The microcomb is generated by an amplified external cavity diode laser (ECDL) and phase-optimized for the generation of Fourier-limited pulses shorter than 200 fs. Subsequent amplification and broadening in highly nonlinear fiber (HNLF) generates an octave-spanning comb spectrum and enables the measurement of the carrier-envelope-offset frequency using an $f - 2f$ interferometer. Repetition rate and carrier-envelope-offset of the microcomb can be stabilized to an atomic clock (hydrogen maser). Amp, erbium-doped fiber amplifier; PD, photodiode; PID, proportional-integral-derivative controller; Shaping, liquid-crystal-based spatial light modulator; SHG, second harmonic generation. b, Octave-spanning microcomb spectrum after nonlinear broadening. [P. Del'Haye, A. Coillet, T. Fortier, K. Beha, D. C. Cole, K. Y. Yang, H. Lee, K. J. Vahala, S. B. Papp, and S. A. Diddams Nature Photonics **10**, 516-520 (2016). The figure is used with permission from Nature Publishing Group.]

are gaining attention, because there are some interesting applications in the visible⁶⁹⁾ and mid-infrared regions^{70,71)}.

In the visible region, there are some biological applications, such as tissue imaging and sensing in water. In the mid-infrared region, there are many absorption lines of gases for which sensing is desired. Microcombs can be applied to these regions as long as a continuous-wave laser exists and the material absorption is small. In 2011, a mid-infrared microcomb was demonstrated with a magnesium fluoride cavity, using dispersion engineering to achieve an anomalous dispersion in the mid-infrared region²⁴⁾. Recently, a microcomb with a silicon ring cavity reached a mode-locked state and was used for measurements of acetylene gas²³⁾. There are some studies utilizing a quantum cascade laser as an input. Thus, there is a possibility of developing microcomb research in the wavelength region of 4.5–10 μm ⁷²⁾. There are few materials to use for a microcomb in the visible, because it is almost impossible to design an anomalous dispersion, due to a strong material dispersion^{73,74)}. However, a diamond ring cavity should have the potential to achieve microcomb generation in the visible. A group at Harvard University achieved the design of an anomalous dispersion in the visible range and fabricated a high- Q diamond ring⁷⁵⁾.

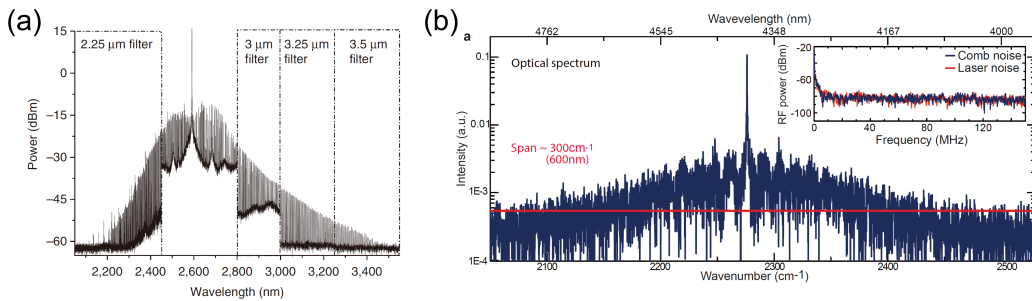


Fig. 1.9: Mid-infrared microcomb generation.

(a) Optical spectrum of microcomb generation with a silicon microring. The input laser is an optical parametric oscillator emitting a wavelength of 2.6 μm ²³⁾. (b) Optical spectrum of microcomb generation with a magnesium fluoride cavity. The input laser is a quantum cascade laser emitting a wavelength of 4.4 μm ⁷⁶⁾. [(a) A. G. Griffith, R. K.W. Lau, J. Cardenas, Y. Okawachi, A. Mohanty, R. Fain, Y. H. D. Lee, M. Yu, C. T. Phare, C. B. Poitras, A. L. Gaeta, and M. Lipson, *Nature Communications* **6**, 6299 (2015). The figure is used with permission from Nature Publishing Group. (b) C. Lecaplain, C. Javerzac-Galy, E. Lucas, J. D. Jost, T. J. Kippenberg, arXiv:1506.00626. (2016). The figure is used with permission from T. J. Kippenberg.]

Cavity solitons require an anomalous dispersion because it compensates for the phase shift derived from a Kerr effect. However, a microcomb with a normal dispersion has been intensively researched^{77–81)} because most materials exhibit strong normal dispersion in the visible and ultraviolet ranges, which are attractive ranges because of some of the practical applications mentioned above. Essentially, there is no four-wave mixing gain in the normal dispersion. Yet, a kind of mode crossing causes a local anomalous dispersion by which wavelength conversion is triggered. Since there is a dark soliton state in the normal dispersion, coherent phase-locked states can be achieved. With coupled microcavities that can control mode crossing, a microcomb in the normal dispersion should be reasonable. Nowadays, a number of studies have reported deep understanding of the mechanism of dark soliton generation from a local anomalous dispersion.

Recently, some research on applications with a microcomb has been reported. In 2014, Pfeifle *et al.* demonstrated coherent terabit communications with a microcomb²⁵⁾. They utilized 20 comb lines with QPSK and achieved 1.44 Tbit/s. In 2016, Suh *et al.* demonstrated dual-comb spectroscopy based on two microcombs, and they measured HCN gas⁸²⁾. Thus, microcombs have already been used as a source of frequency combs, although there is still much to be understood, such as dark soliton generation^{80,83)}, dispersive wave emission^{84,85)}, and the relationship between four-wave mixing and other nonlinear optical effects, such as stimulated Raman scattering⁸⁶⁾.

1.4 Stimulated Raman scattering and Raman comb

In 2002, Spillane *et al.* reported an ultra-low threshold Raman laser with a silica microsphere with a Q of over 100 million⁷⁾. Since Raman scattering is a process that converts optical energy into molecular vibration, the wavelength is converted to a length longer than the original line. Thus, stimulated Raman scattering is a way to access long wavelengths efficiently. Raman lasing has been demonstrated by using high- Q cavities made of not only silica, calcium fluoride^{6,87,88)}, polymer^{89,90)}, diamond⁷⁵⁾, and other materials^{91,92)}. Since the amount of Stokes shift of the Raman gain is inherent to materials, the material of a cavity should be limited in order to obtain a very long-wavelength Raman laser. Diamond that

has 40 THz of Stokes shift is a powerful material, and 2 – μm Raman lasing with 1550-nm pumping has been demonstrated⁷⁵⁾.

Cascaded Raman lasing has been also reported by using silicon and silica high- Q cavities^{5,93)}. Even if the Stokes shift is comparatively small, cascaded conversion reaches a large amount of the shift. The silicon Raman lasing conducted by Rong *et al.*⁹³⁾ demonstrated measurements of gases with first-order Raman output (~ 1680 nm) and second-order Raman output (~ 1850 nm). Thus, mid-infrared Raman lasers should be also accessed by using cascaded Raman lasing with high- Q cavities.

In contrast to crystalline materials such as silicon and calcium fluoride, silica exhibits broad Raman gain because of its amorphous structure. Research with a silica microsphere showed a number of Raman oscillation lines around 1670 nm from a continuous-wave input. The multimode Raman outputs are spaced equidistantly due to the cavity resonance, creating what seems to be a comb derived from stimulated Raman scattering.

In 2010, Liang *et al.* demonstrated a mode-locked Raman comb with a calcium fluoride cavity⁹⁴⁾. Although calcium fluoride is crystalline with a narrow Raman gain, they observed Raman oscillations over 40 lines spaced with a 35 GHz interval. Interestingly, the phase noise measurement revealed that Raman lines are mutually coherent, which indicates mode-locking. Thus, this research opens the way to frequency comb generation with stimulated Raman scattering. An advantage of stimulated Raman scattering is that it occurs in the normal dispersion, in contrast to four-wave mixing. So, if a mode-locked Raman comb can be readily accessed, a Raman comb with a microcavity is useful even in the normal dispersion.

Recently, Lin and Chembo⁹⁵⁾ reported an observation of a phase-locking transition of a Raman comb with a barium fluoride cavity. Thus, mode-locked Raman comb generation is still attractive with respect to nonlinear physics and comb generation in the long wavelength region.

1.5 Third-harmonic generation and visible comb

Microcomb generation with a visible continuous-wave pump has been researched, as mentioned above. On the other hand, a visible comb produced via second- and third-harmonic generation has been also reported. In 2007, Carmon and Vahala⁹⁾ demonstrated visible light generation with a silica toroid microcavity. Due to a high Q , efficiency of third-harmonic generation is much higher in spite of poor mode overlapping. The phase matching is automatically satisfied with the selection of a third-harmonic mode of which the effective refractive index is the same as that of a pump mode. Since a third-harmonic mode is usually a much higher-order mode than a pump mode, the Q should be low. However, it contributes to easy achievement of frequency matching, because the low Q means a broad Lorentzian spectrum. Most materials exhibit a normal dispersion in the visible region. Thus, common microcomb generation does not occur because it requires an anomalous dispersion. Therefore, harmonic generation should be a reasonable way to obtain a visible comb with a microcavity. Upconversion lasers emitting visible light have been also demonstrated by using doped silica cavities. Silica glass can be doped with many kinds of rare earth trivalent ions: not only erbium, but also ytterbium, neodymium, and thulium. Lu *et al.*⁹⁶⁾ reported that an erbium-doped silica toroid cavity with a near-infrared pump emits visible light in the range between 520 and 560 nm. A blue upconversion laser with a 1064 nm pump has been demonstrated by using a thulium-doped silica microcavity⁹⁷⁾. Thus, upconversion with doped silica cavities is a promising way to obtain visible light with near-infrared pumping. In 2011, Miller *et al.*⁹⁸⁾ demonstrated visible comb generation via second-harmonic generation with a silicon nitride ring. The visible comb occurred from a continuous-wave input in the near-infrared region. This phenomenon explains that a microcomb occurs first in the near-infrared region, and each comb line causes second-harmonic generation, which forms lines even in the visible region. Similar research with third-harmonic generation and with both second- and third-harmonic generation has been reported⁹⁹⁾.

The combination of four-wave mixing, stimulated Raman scattering, and third-harmonic generation causes multi-colored emissions with a silica microsphere¹⁰⁰⁾ and a lithium niobate cavity¹⁰¹⁾. Although the mechanism is still too complex to

understand, a broad visible spectrum is obtained.

1.6 Motivation and objective of this study

I described the background of high- Q microcavities and optical frequency combs. Then, I introduced recent progress on optical frequency comb generation with a microcavity, via nonlinear optical effects including four-wave mixing, stimulated Raman scattering, and third-harmonic generation. The motivations for this study are explained in this section.

· For Microcombs

Microcombs derived from four-wave mixing have been intensively researched to achieve mode-locking. The first demonstration of mode-locked microcombs was performed with wavelength scanning to compensate for resonant shifts caused by Kerr and thermo-optic effects. Theoretical research has also revealed much important information—for example, that Turing patterns and cavity solitons occur in the effectively blue and red detunings, respectively. Such understanding cannot be obtained without theoretical and numerical analyses.

One problem with the wavelength scanning method is that there is not always a good tunable laser in every frequency region. It is true that almost all wavelengths can be accessed with optical parametric oscillators and quantum cascade lasers. Yet, they are expensive and complex, which takes away the advantage of microcombs in terms of cost and simplicity. The motivation of this study is to develop a simple method that complements the wavelength scanning method for mode-locked microcomb generation in every frequency region.

To develop a novel method, numerical simulation with a Lugiato-Lefever model was used. Considering the hysteresis behavior of a nonlinear cavity, wavelength scanning and input power scanning should have the same meaning for nonlinear dynamics. I focus on input power control, which is readily achieved with a kind of optical attenuator and is a versatile method in every frequency region. I will first illustrate a mode-locked microcomb with an input power control by using numerical simulation. Second, I will prove the concept experimentally with a silica toroid microcavity, resulting in the first demonstration of mode-locking operation in a silica toroid microcavity.

· For Ramancombs

Raman lasing has been used with many kinds of microcavities. Long-wavelength Raman lasers (around 2 μm) have been achieved and are useful for measurements of gases. While single-mode lasing has been developed, multi-mode Raman lasing derived from a broad bandwidth of the Raman gain is an attractive goal. A few studies on mode-locked multi-mode Raman lasing have been done, and further research seems promising for mode-locked Raman comb generation and Raman soliton generation.

Silica has a broader bandwidth of the Raman gain than crystalline materials, due to its amorphous structure. Thus, silica cavities have the ability to produce a broad-bandwidth Raman comb. Although stimulated Raman scattering in silica cavities has been widely investigated, experimental demonstration of multi-mode Raman lasing is still lacking. The motivation of this study is to make the physics of this topic clear for broad Raman comb generation.

I will study two kinds of comb spectra resulting from stimulated Raman scattering in a silica toroid microcavity. The difference between them is caused by mode interaction between transverse modes via the stimulated Raman scattering process. To explain the physics, both theoretical analyses and experiments were conducted. I also perform numerical analyses with simultaneous Lugiato-Lefever equations.

· For Visible combs

Frequency combs in the visible range are useful for practical applications, including biological imaging. Simple comb sources are desired, although conventional comb sources already exist in the visible range. Microcavity-based visible combs are promising because of their simplicity. Upconversion via third-harmonic generation is one way to obtain a visible comb with a telecom-wavelength laser.

Some researchers have pointed out that combinations of third-harmonic generation, four-wave mixing, and stimulated Raman scattering contribute to generation of broad visible light spectra in a high- Q cavity with a telecom pump. Yet, the relationship between spectra in the visible and near-infrared regions is still unclear. In particular, silica cavities exhibit strong Raman oscillations in addition to four-wave mixing, which complicates the visible spectrum.

I study broad bandwidth visible light emission via third-harmonic generation

with a silica toroid microcavity. I measure both spectra at the same time to understand the relation between the spectra in the visible and near-infrared regions. From the results, I find how broad visible lights generate via combinations of third-harmonic generation, four-wave mixing, and stimulated Raman scattering.

A silica toroid microcavity has the potential to produce a microcomb in the near-infrared range, an octave-spanning Raman comb, and a visible comb via third-harmonic generation. This dissertation paves the way for the development of applications with silica toroid microcavity-based frequency combs.

1.7 Thesis statement and overview

This thesis explores nonlinear optical processes with silica toroid microcavities. High- Q microcavities, including silica toroid microcavities, are efficient and convenient devices that induce nonlinear parametric frequency conversion via third-order nonlinearity. Optical frequency comb generation from a continuous-wave laser was attempted via the devices. Compact sources of optical frequency combs allow their application possibilities to expand to practical uses, such as sensing and spectroscopy products. This thesis demonstrates multi-frequency generation via three nonlinear optical processes (four-wave mixing, stimulated Raman scattering, and third-harmonic generation) with a silica toroid microcavity, which paves the way to generate an optical frequency comb with high- Q microcavities.

This thesis consists of seven chapters, including this introduction, and is organized as follows:

Chapter 1 summarizes the development of microcavity-based optical frequency comb generation via third-order nonlinear optical processes. Recent progress in microcomb-, Raman comb-, and visible comb-technologies are introduced. The objective of the thesis is stated.

Chapter 2 describes the basic theory and fabrication of both a silica toroid microcavity and a tapered fiber. The experimental setups to measure the nonlinear processes (four-wave mixing, stimulated Raman scattering, and third-harmonic generation) with a fabricated silica toroid microcavity are described.

Chapter 3 presents a demonstration of a newly proposed method for achieving mode-locking in a microcomb system. A model based on the Lugiato-Lefever equation is developed to analyze microcomb generation, and it reveals that the hysteresis behavior of a nonlinear cavity is key to achieving mode-locking. In contrast to previous methods, where the frequency of the input laser was scanned, it is noted (both numerically and experimentally) that mode-locking could also be achieved by adequately sweeping the input laser power.

Chapter 4 describes a study of the gain competition between four-wave mixing and SRS that occurs in a silica microcavity. By considering the free-spectral-range (FSR) in addition to an analysis of maximum gains of four-wave mixing and stimulated Raman scattering, it is found that we can either suppress or enhance the modulation instability gain by changing the input power and the coupling Q in a large-FSR silica cavity. This will allow us to control the transition from a four-wave mixing dominant state to an stimulated Raman scattering dominant state.

Chapter 5 discusses the transverse mode interaction that occurs as a result of stimulated Raman scattering in a silica cavity, which has broad Raman gain. It is found that, in such a system, the transverse mode interaction occurs from a low- Q to a high- Q transverse mode family via an stimulated Raman scattering process when a low- Q mode is pumped. As a result, a dual-comb-like spectrum appears. The transverse mode interaction dependence on the Q value and the spatial overlap between different transverse mode families are described both numerically and experimentally.

Chapter 6 describes a demonstration of visible light emission via third-harmonic generation. Experimentally, it is shown that both four-wave mixing and stimulated Raman scattering in the near-infrared region influence the spectrum shape of the generated visible light.

Chapter 7 summarizes this dissertation, its contributions, and potential future research on nonlinear optical processes with a silica toroid microcavity.

In Appendix A, a polygonal silica toroid microcavity for stable coupling is described. An octagonal cavity shape is proposed and analyzed via a finite-domain time-difference method. A fabrication process that includes a combination of wet and dry etchings is developed. The experimental results are shown.

In Appendix B, theories of both the optical cavity and whispering gallery mode are described. A relationship between the linewidth of the resonance and Q -factor is derived. From the Helmholtz equation, general expression of whispering gallery modes in a microsphere cavity is derived.

In Appendix C, the Lugiato-Lefever equation is derived. However, prior to that derivation, a nonlinear Schrödinger equation is derived from a wave equation. By considering the combination of the nonlinear Schrödinger equation and the coupled mode theory, the Lugiato-Lefever equation is then described.

Chapter 2

Silica toroid microcavity

In this chapter, I describe mathematical expressions of a silica toroid microcavity and evaluate a fabricated silica toroid microcavity experimentally. Since the main purpose of this thesis is the study of nonlinear frequency conversion with a silica toroid microcavity, comprehension of theories related to high- Q cavities, tapered fibers, and nonlinear optical processes is necessary. Experimental protocols related to the fabrication of silica toroid microcavities and tapered fibers are also discussed. Finally, methods of measurement of nonlinearity are explained.

Section 2.1 describes quality-factor in an optical cavity. Section 2.2 describes the theory of coupling between optical components. Section 2.3 describes the spatial mode profiles of the optical modes in a silica toroid cavity. Section 2.4 describes the theory of optical modes in a tapered fiber. Section 2.5 describes theories of four-wave mixing, stimulated Raman scattering, and third-harmonic generation in a high- Q cavity. Section 2.6 explains fabrication methods for a silica toroid microcavity and a tapered fiber. Section 2.7 shows methods to measure Q -factor and nonlinearity.

2.1 Theory of quality-factor

As described in Chapter 1, high- Q is essence for the objectives of this dissertation. This section explains the theory of Q -factor of an optical cavity.

Q -factor expresses the extent to which dissipation is present in a resonant system. The description is defined as follows:

$$Q = \omega_r \frac{\text{Stored energy[J]}}{\text{Power loss[W]}}, \quad (2.1)$$

where ω_r is the angular frequency at a resonance. The factors for the dissipations are related to the photon lifetime and the linewidth of the resonance. Given that a photon lifetime and a full-width half-maximum (FWHM) of the linewidth are expressed as τ_p and $\Delta\nu_r$, relationships yield

$$Q = \omega_r \tau_p \approx \frac{\nu_r}{\Delta\nu_r}. \quad (2.2)$$

The typical values of Q , $\Delta\nu_r$, and τ_p at the telecom are shown in Table 1.1.

When Q is discussed, the causes of propagation loss should be divided into material-based loss, scattering-based loss, coupling loss, and so on. Since they are parallel, the total Q is

$$Q_{\text{total}}^{-1} = Q_{\text{material}}^{-1} + Q_{\text{scattering}}^{-1} + Q_{\text{couple}}^{-1} + \dots. \quad (2.3)$$

Note that the total Q limits the lowest Q that causes the largest loss. Figure 2.1 shows a category of causes of loss. Causes are divided into two types: intrinsic loss and external loss. Intrinsic loss indicates the loss caused by the factors the cavity has independently. Surface scattering loss and material absorption loss are categorized as intrinsic loss. On the other hand, external loss means the loss caused by perturbation from external components such as a waveguide. In this dissertation, Q_{int} and Q_{e} will refer to the Q depending on intrinsic loss and external loss, respectively. A Q measured experimentally indicates a Q_{total} .

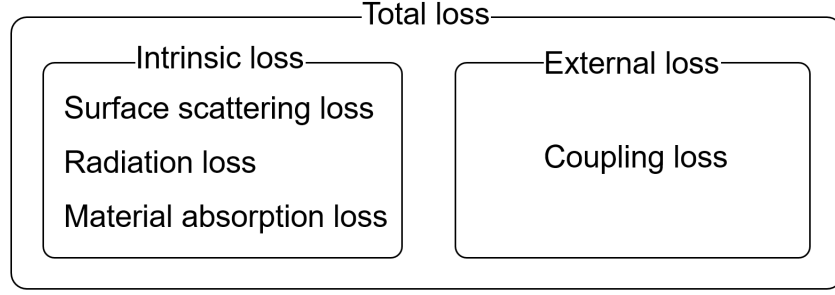


Fig. 2.1: Different causes of propagation loss. Intrinsic loss includes kinds of loss depending the cavity itself such as surface scattering and material absorption. External loss indicates loss caused by perturbation from external components such as a waveguide.

Table. 2.1: Relation between Q factor, $\Delta\nu$, $\Delta\lambda$ and τ_p at $\lambda = 1550$ nm

Q factor	$\Delta\nu$	$\Delta\lambda$	τ_p
1×10^6	193.4 MHz	1.55 pm	0.823 ns
2×10^6	96.71 MHz	0.775 pm	1.646 ns
1×10^7	19.34 MHz	0.155 pm	8.23 ns
2×10^7	9.671 MHz	0.0775 pm	16.46 ns
1×10^8	1.934 MHz	15.5 fm	82.3 ns
2×10^8	967.1 kHz	7.75 fm	164.6 ns
1×10^9	193.4 kHz	1.55 fm	0.823 μ s
2×10^9	96.71 kHz	0.775 fm	1.646 μ s

2.2 Theory of coupling between optical components

A coupled mode theory describes how light behaves between multiple optical components^{102,103}). In this section, it expresses the coupling of a light between a cavity and a waveguide. Among the several types of cavity-waveguide systems, a side coupling as shown in Figure 2.2 is regarded the best explanatory model for the experimental system described later.

On a side coupling system, U_{cav} is set as the amplitude in a cavity, where $|U_{\text{cav}}|^2$ corresponds to the stored energy within the cavity. Considering an intrinsic loss and a coupling loss, U_{cav} yields

$$U_{\text{cav}}(t) = U_0 \exp(j\omega t) \exp(-\alpha_{\text{int}} t) \exp(-\alpha_e t), \quad (2.4)$$

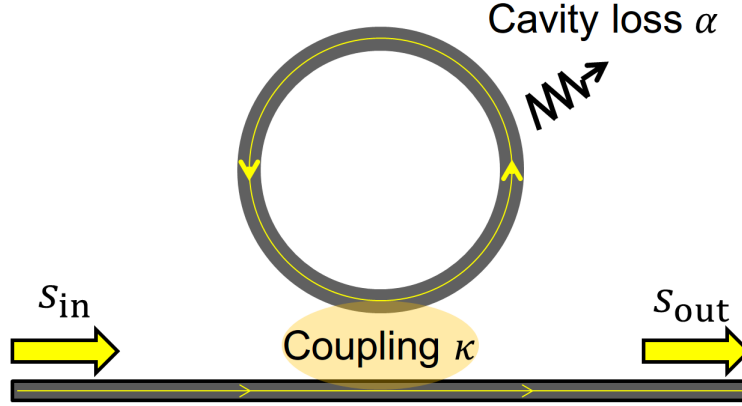


Fig. 2.2: Side coupling system. A cavity and a waveguide connect with a coupling coefficient κ .

where α_{int} and α_e are the loss related to $Q_{intrinsic}$ and $Q_{external}$, respectively. The time variation of U_{cav} is described as

$$\frac{dU_{cav}(t)}{dt} = (j\omega - \alpha_{int} - \alpha_e)U_{cav}(t) = \left(j\omega - \frac{1}{2\tau_{int}} - \frac{1}{2\tau_e}\right)U_{cav}(t). \quad (2.5)$$

Then, input s_{in} and output s_{out} in a waveguide must be considered, where $|s_{in}|^2$ and $|s_{out}|^2$ correspond to the input power and the output power, respectively. With a perturbation from the waveguide, Equation 2.5 is modified as follows:

$$\frac{dU_{cav}(t)}{dt} = \left(j\omega - \frac{1}{2\tau_{int}} - \frac{1}{2\tau_e}\right)U_{cav}(t) + \kappa s_{in}, \quad (2.6)$$

where κ is a coupling coefficient of s_{in} to the cavity. Given steady state $\frac{dU_{cav}(t)}{dt} = 0$, the amplitude yields

$$U_{cav}(t) = \frac{\kappa s_{in}}{j(\omega_{in} - \omega) + \left(\frac{1}{2\tau_{int}} + \frac{1}{2\tau_e}\right)}, \quad (2.7)$$

where ω_{in} is the angular frequency of an input. To understand κ clearly, the flow of energy from a cavity to a waveguide must be discussed. Given that an intrinsic loss α_{int} and an input s_{in} can be neglected, the energy in a cavity and the time variation are derived as

$$|U_{cav}(t)|^2 = |U_0|^2 \exp(-2\alpha_e t), \quad (2.8)$$

$$\frac{d|U_{\text{cav}}(t)|^2}{dt} = -2\alpha_e|U_{\text{cav}}(t)|^2 = -\frac{1}{\tau_e}|U_{\text{cav}}(t)|^2. \quad (2.9)$$

To satisfy the condition of energy conservation, $|s_{\text{out}}|^2$ is given by

$$|s_{\text{out}}|^2 = \frac{1}{\tau_e}|U_{\text{cav}}(t)|^2, \quad (2.10)$$

$$s_{\text{out}} = \sqrt{\frac{1}{\tau_e}}U_{\text{cav}}(t). \quad (2.11)$$

Here, the coupling rate from a cavity to a waveguide and from a waveguide to a cavity must be the same with respect to energy. Therefore, the relationship

$$\kappa = \sqrt{\frac{1}{\tau_e}}, \quad (2.12)$$

is satisfied, and it is a clear description of κ . Next, considering an input s_{in} and an intrinsic loss α_{int} , the output s_{out} yields

$$s_{\text{out}} = As_{\text{in}} + \sqrt{\frac{1}{\tau_e}}U_{\text{cav}}(t). \quad (2.13)$$

Now, from the point of view of energy conservation, the relationship is derived as

$$|s_{\text{in}}|^2 - |s_{\text{out}}|^2 = \frac{d}{dt}|U_{\text{cav}}(t)|^2 + \frac{1}{\tau_{\text{int}}}|U_{\text{cav}}(t)|^2. \quad (2.14)$$

Note that the difference between input and output is expressed as a summation of the variance in stored energy in the cavity and an intrinsic loss. In the same manner as Equations 2.6–2.9, the time variation of stored energy is given by

$$\frac{d}{dt}|U_{\text{cav}}(t)|^2 = -\left(\frac{1}{\tau_{\text{int}}} + \frac{1}{\tau_e}\right)|U_{\text{cav}}(t)|^2 + \sqrt{\frac{1}{\tau_e}}(U_{\text{cav}}^*s_{\text{in}} + U_{\text{cav}}s_{\text{in}}^*), \quad (2.15)$$

where the third and fourth terms on the right side are descriptions with related phases. With Equations 2.13 and 2.15, Equation 2.14 is developed as follows:

$$|s_{\text{in}}|^2 - |As_{\text{in}} + \sqrt{\frac{1}{\tau_e}} U_{\text{cav}}(t)|^2 = -\left(\frac{1}{\tau_{\text{int}}} + \frac{1}{\tau_e}\right) |U_{\text{cav}}(t)|^2 + \sqrt{\frac{1}{\tau_e}} (U_{\text{cav}}^* s_{\text{in}} + U_{\text{cav}} s_{\text{in}}^*) + \frac{1}{\tau_{\text{int}}} |U_{\text{cav}}(t)|^2. \quad (2.16)$$

Hence, two relationships are derived as

$$A = -1, \quad (2.17)$$

$$s_{\text{out}} = -s_{\text{in}} + \sqrt{\frac{1}{\tau_e}} U_{\text{cav}}(t). \quad (2.18)$$

With the relationships developed so far, the transmittance of an amplitude t between a cavity and a waveguide yields

$$t = \frac{s_{\text{out}}}{s_{\text{in}}} = -1 + \sqrt{\frac{1}{\tau_e}} \frac{\kappa}{j(\omega_{\text{in}} - \omega) + \left(\frac{1}{2\tau_{\text{int}}} + \frac{1}{2\tau_e}\right)} = \frac{-j(\omega_{\text{in}} - \omega) - \frac{1}{2\tau_{\text{int}}} + \frac{1}{2\tau_e}}{j(\omega_{\text{in}} - \omega) + \frac{1}{2\tau_{\text{int}}} + \frac{1}{2\tau_e}}. \quad (2.19)$$

When the frequency of input light and the resonant frequency of a cavity are matched (the detuning is zero), a simplification is possible:

$$t = \frac{-\frac{1}{2\tau_{\text{int}}} + \frac{1}{2\tau_e}}{\frac{1}{2\tau_{\text{int}}} + \frac{1}{2\tau_e}} = \frac{-\frac{1}{\tau_{\text{int}}} + \frac{1}{\tau_e}}{\frac{1}{\tau_{\text{int}}} + \frac{1}{\tau_e}} = \frac{Q_{\text{int}} - Q_e}{Q_{\text{int}} + Q_e}. \quad (2.20)$$

Note that t becomes zero when Q_{int} is equal to Q_e . This condition exhibits maximum coupling efficiency and is called "critical coupling". Based on strength of the coupling, conditions are distinguished as follows:

$$\begin{cases} Q_{\text{int}} < Q_e & \text{for under coupling} \\ Q_{\text{int}} = Q_e & \text{for critical coupling} \\ Q_{\text{int}} > Q_e & \text{for over coupling} \end{cases} \quad (2.21)$$

Experimentally, a Q_{total} and a transmittance intensity T can be observed. T is given by

$$T = |t|^2 = \left| \frac{s_{\text{out}}}{s_{\text{in}}} \right|^2 = \left| 1 - 2 \frac{Q_{\text{total}}}{Q_{\text{int}}} \right|^2, \quad (2.22)$$

$$Q_{\text{int}} = \frac{2}{1 \mp \sqrt{T}} Q_{\text{total}}. \quad (2.23)$$

From these relationships, the intrinsic performance Q_{int} is calculated. Minus and plus signs mean overcoupling and undercoupling, respectively.

From coupled mode theory, the amplification factor of the electric amplitude of a cavity can be estimated. Electric amplitude in the cavity at a steady state is described by Equation 2.7. The net power in a cavity at a steady state yields

$$|U_{\text{cav}}(t)|^2 = \frac{1}{(\omega_{\text{in}} - \omega)^2 + \left(\frac{1}{2\tau_{\text{total}}}\right)^2} \frac{P_{\text{in}}}{\tau_e}. \quad (2.24)$$

Since the $|U_{\text{cav}}(t)|^2$ is the net energy [J] in the cavity, the intracavity power P_{cav} is derived as

$$P_{\text{cav}} = \frac{|U_{\text{cav}}(t)|^2}{t_{\text{round trip}}} = |U_{\text{cav}}(t)|^2 \cdot \nu_{\text{FSR}}. \quad (2.25)$$

A general expression of the intracavity power yields

$$P_{\text{cav}} = \frac{1}{(\omega_{\text{in}} - \omega)^2 + \left(\frac{1}{2\tau_{\text{total}}}\right)^2} \frac{P_{\text{in}}}{\tau_e} \cdot \nu_{\text{FSR}}, \quad (2.26)$$

$$P_{\text{cav}} = \frac{4\tau_{\text{total}}^2}{4\tau_{\text{total}}^2(\omega_{\text{in}} - \omega)^2 + 1} \frac{P_{\text{in}}}{\tau_e} \cdot \nu_{\text{FSR}}, \quad (2.27)$$

$$P_{\text{cav}} = \frac{4\tau_{\text{total}}^2 \cdot \nu_{\text{FSR}}}{\tau_e} \frac{1}{4 \cdot \left(\frac{\nu_{\text{in}} - \nu}{\Delta\nu}\right)^2 + 1} \cdot P_{\text{in}}, \quad (2.28)$$

$$P_{\text{cav}} = \frac{4Q_{\text{total}} \cdot \nu_{\text{FSR}}}{\omega} \cdot \frac{Q_{\text{int}}}{Q_{\text{int}} + Q_e} \cdot \frac{1}{4 \cdot \left(\frac{\nu_{\text{in}} - \nu}{\Delta\nu}\right)^2 + 1} \cdot P_{\text{in}}. \quad (2.29)$$

With Equation 2.29, given that the detuning is zero, P_{cav} is simplified as follows:

$$P_{\text{cav}} = \frac{4Q_{\text{total}} \cdot \nu_{\text{FSR}}}{\omega} \cdot \frac{Q_{\text{int}}}{Q_{\text{int}} + Q_e} \cdot P_{\text{in}}. \quad (2.30)$$

When a critical coupling is achieved, P_{cav} can be written by

$$P_{\text{cav}} = \frac{2Q_{\text{total}} \cdot \nu_{\text{FSR}}}{\omega} \cdot P_{\text{in}} = \frac{Q_{\text{total}} \cdot \nu_{\text{FSR}}}{\pi \cdot \nu} \cdot P_{\text{in}}. \quad (2.31)$$

Now, "finesse F " is defined and the relationship between P_{cav} and F is described as

$$P_{\text{cav}} = \frac{F}{\pi} \cdot P_{\text{in}}, \quad (2.32)$$

$$F = \frac{\nu_{\text{FSR}}}{\Delta\nu} = \frac{\nu_{\text{FSR}}}{\nu} \cdot Q_{\text{total}}. \quad (2.33)$$

This is the amplification factor of a cavity. Given a Q_{total} of 1 million, a ν_{FSR} of 800 GHz, a ν of 193 THz, and an input power of 1 mW, the calculated intracavity power is at most 4.15 W, which is 4150 times higher than the input power.

2.3 Theory of optical modes in silica toroid microcavity

This section explains whispering gallery modes excited in a silica toroid microcavity. Theory of whispering gallery modes in microsphere cavities is detailed in Appendix B.2.

A mathematical description of whispering gallery modes in microspheres derives from a wave equation in spherical coordinates (r, θ, ϕ) : radial distance r , polar angle θ , and azimuthal angle ϕ . Given a ψ as a function of light, two separated equations that whispering gallery modes satisfy are derived as^{104,105)}

$$Y_l^m(\theta, \phi) = p(l, m) \cdot P_l^m(\cos\theta) \cdot e^{im\phi}, \quad (2.34)$$

$$\frac{d^2}{dr^2} \psi_r(r) + \frac{2}{r} \frac{d}{dr} \psi_r(r) + [k_0^2 n^2 - \frac{l(l+1)}{r^2}] \psi_r(r) = 0. \quad (2.35)$$

where l , m , p , k_0 , and n correspond to a polar quantum number, an azimuthal quantum number, a constant depending on l and m , the wavenumber, and the refractive index of the material, respectively. Y and P are spherical harmonics

and the Legendre polynomial, respectively. Figure 2.3 shows mode profiles in the radial direction for whispering gallery modes in a silica microsphere. The first three radial modes ($r = 1, 2, 3$) are shown because low-order modes have high- Q due to their weak light leakage.

Whispering gallery modes in a silica toroid microcavity follow the same path as those in a microsphere. However, because derivation of the general mathematical expression^{106,107}) is complex, numerical calculation with a finite-element method (FEM) is usually used to analyze the spatial mode profiles in a silica toroid microcavity¹⁰⁸). There are two parameters (major and minor radii) that can model a silica toroid microcavity as shown in Figure 2.4. Figure 2.5 shows the cross-sectional spatial mode profiles of three transverse-electric (TE) mode families (TE₀₀, TE₀₁, and TE₁₀) in a silica toroid microcavity with a major radius of 50 μm . Although transverse-magnetic (TM) modes are also considered, TE modes are the focus of this thesis because TE modes exhibit a higher- Q than TM modes due to their weaker light leakage. The effective mode volume V for nonlinear processes can be evaluated as

$$V = \frac{\int |\mathbf{E}|^2 dV \int |\mathbf{E}|^2 dV}{\int |\mathbf{E}|^4 dV}. \quad (2.36)$$

Since the optical density of a cavity is proportional to $1/V$, a small mode volume is required for high efficiency for nonlinear processes. Effective mode area A_{eff} is also used, where $V \approx L_{\text{cavity}} A_{\text{eff}}$. The calculated values of the effective mode area of three modes as shown in Figure 2.5 are 9.75, 12.78, and 17.75 μm^2 , respectively. Thus, the fundamental mode TE₀₀ has the minimum mode volume. Notably, the single mode operation in a silica toroid microcavity can be achieved by making the minor radius small. However, it is not needed for stable operation because the excited mode can be selected by phase matching between the mode in the cavity and the optical mode in the tapered fiber, which is described in the next section.

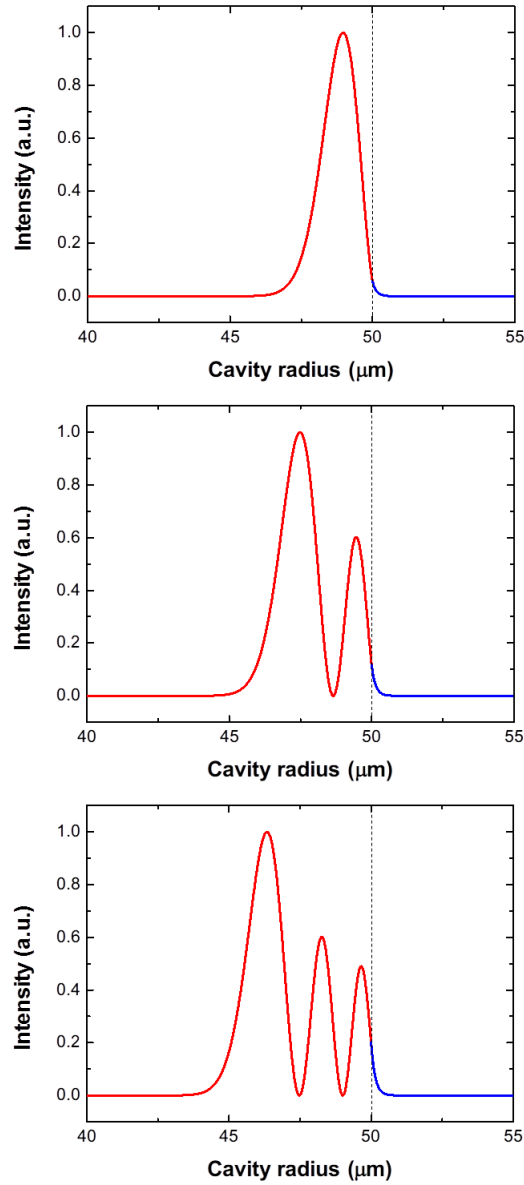


Fig. 2.3: Intensity mode profile $|E_r|^2$ in the radial direction for a microsphere with a principal radius of $50 \mu\text{m}$ and an azimuthal mode number $m = 280$ for the first three radial mode numbers ($r = 1, 2, 3$). The wavelength corresponds to 1552.95 nm , 1505.95 nm , and 1469.52 nm , respectively. The ratios of the evanescent field in the total mode profile are 0.498% , 0.839% , and 1.307% , respectively.

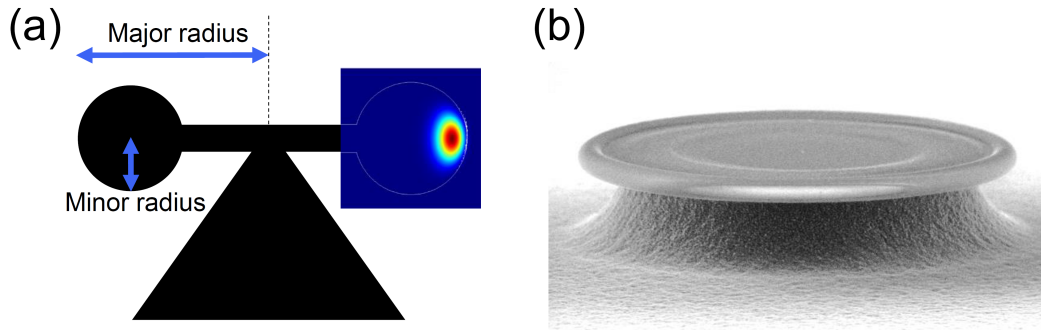


Fig. 2.4: (a) Schematic image of a silica toroid microcavity. Both the major and minor radii are defined, as shown. A mode profile is a typical fundamental mode in the cavity. (b) A scanning electron microscope image of a silica toroid microcavity.

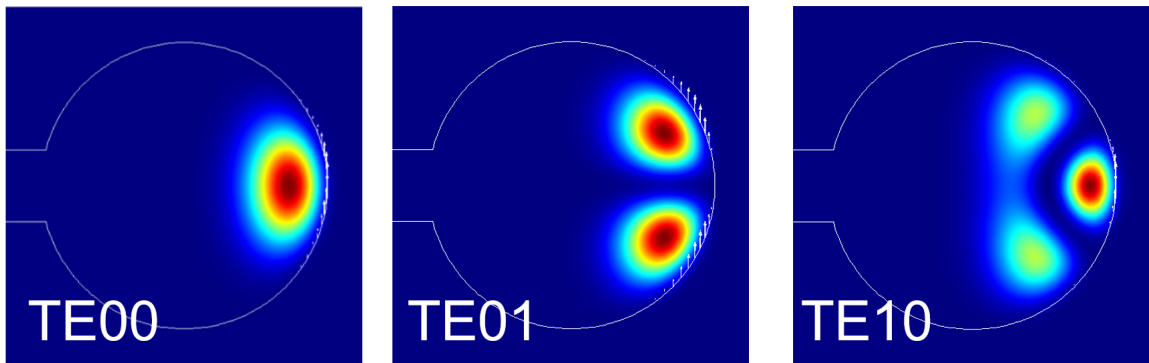


Fig. 2.5: Three TE modes in a silica toroid microcavity. The major and minor radii are $50\ \mu\text{m}$ and $4\ \mu\text{m}$.

2.4 Theory of optical modes in tapered fiber

This section explains how a tapered fiber is required to measure a silica toroid microcavity. Since the cavity excites whispering gallery modes, a coupling with an evanescent wave is needed. To achieve this coupling, a prism, an angled fiber, and a tapered fiber are commonly used. Recently, a free space coupling was also achieved¹⁰⁹). A tapered fiber is a fiber with a thin part in which an evanescent field becomes large. Couplings between a prism and an angled fiber are easy to achieve compared to those with a tapered fiber, because a tapered fiber is easily broken. However, since a tapered fiber enables a propagation loss of nearly zero, it is suitable for demonstrating nonlinear optical effects requiring high power^{110–112}). In this thesis, because nonlinear optical effects with a silica toroid microcavity are the objective, a tapered fiber was selected. From the theory of optical fibers, a general expression of a tapered fiber is described here.

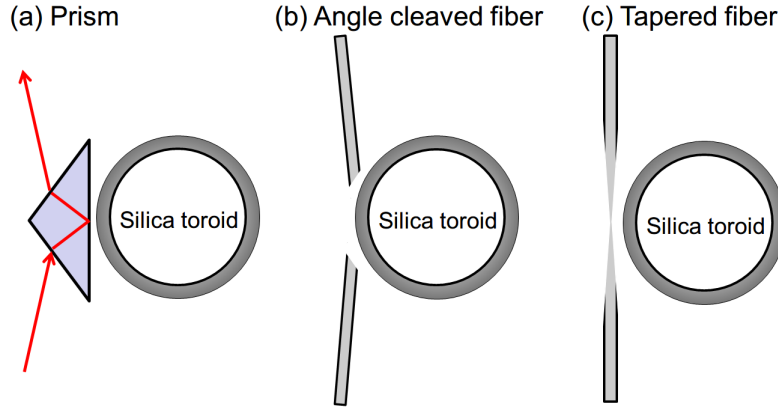


Fig. 2.6: Schematic images of some evanescent coupling devices. (a) Prism coupling. (b) Angle-cleaved fiber coupling. (c) Tapered fiber coupling.

The profile of an electromagnetic wave in an optical fiber follows a wave equation, which is transformed into the cylindrical coordinate system as follows:

$$\frac{\partial^2 E_z}{\partial r^2} + \frac{1}{r} \frac{\partial E_z}{\partial r} + \frac{1}{r^2} \frac{\partial^2 E_z}{\partial \theta^2} + \frac{\partial^2 E_z}{\partial z^2} + n^2 k_0^2 E_z = 0, \quad (2.37)$$

where E_z can be regarded as H_z . In an optical fiber, propagation with a direction of z depends on a propagation constant β , which is expressed as $e^{-i\beta z}$. On the

other hand, propagation with a direction of θ requires periodicity to satisfy circular symmetry. Since there are various candidates to choose among, I have set it as $e^{-il\theta}$ with an integer l . Considering these, the electric amplitude E_z is given by

$$E_z(r, \theta, z) = E_z(r) e^{-i\beta z} e^{-il\theta}. \quad (2.38)$$

Thus, the wave equation 2.37 is solved with respect to E_z with only r dependence as follows:

$$\frac{d^2 E_z(r)}{dr^2} + \frac{1}{r} \frac{dE_z(r)}{dr} + (n^2 k_0^2 - \beta^2 - \frac{l^2}{r^2}) E_z(r) = 0. \quad (2.39)$$

Here, refractive indices of the core and the clad are n_1 and n_2 , respectively. Given that the propagation constant is smaller than the wave number in the core ($\beta < n_1 k_0$) and is larger than that in the clad ($\beta > n_2 k_0$), light can propagate with total internal reflection in the fiber. To satisfy this condition, two parameters (κ , γ) are defined as

$$\kappa^2 = n_1^2 k_0^2 - \beta^2, \quad (2.40)$$

$$\gamma^2 = \beta^2 - n_2^2 k_0^2, \quad (2.41)$$

where both κ and γ are real. Now the electric amplitude in the core and clad is given by

$$\begin{cases} \frac{d^2 E_z(r)}{dr^2} + \frac{1}{r} \frac{dE_z(r)}{dr} + (\kappa^2 - \frac{l^2}{r^2}) E_z(r) = 0 & r < a, \text{ (for core),} \\ \frac{d^2 E_z(r)}{dr^2} + \frac{1}{r} \frac{dE_z(r)}{dr} - (\gamma^2 + \frac{l^2}{r^2}) E_z(r) = 0 & r > a, \text{ (for clad),} \end{cases} \quad (2.42)$$

where a means a boundary of the core and the clad. Solutions of these differential equations are Bessel functions of the first kind and modified Bessel functions of

the second kind, as follows:

$$\begin{cases} E_z \propto J_l(\kappa r) & r < a, \text{ (for core).} \\ E_z \propto K_l(\gamma r) & r > a, \text{ (for clad).} \end{cases} \quad (2.43)$$

Several propagation modes can exist in an optical fiber if the thickness of the core is large for the light. To explain this clearly, a parameter V_{fiber} is defined as

$$(\kappa a)^2 + (\gamma a)^2 = V_{\text{fiber}}^2, \quad (2.44)$$

$$V_{\text{fiber}} = k_0 n_1 a \sqrt{2 \frac{n_1^2 - n_2^2}{2n_1^2}}. \quad (2.45)$$

To have a propagation mode, each electromagnetic component must satisfy the theory of continuity at the boundary between the core and the clad. With a weakly-guiding approximation ($n_1 \approx n_2$), the condition is given by

$$(\kappa a) \frac{J_{l\mp 1}(\kappa a)}{J_l(\kappa a)} = \mp(\gamma a) \frac{K_{l\mp 1}(\gamma a)}{K_l(\gamma a)}, \quad (2.46)$$

where signs \mp correspond to HE modes and EH modes, respectively. Figure 2.7 shows relationships indicated by HE and EH modes with $l = 0, 1$. Analytically, the HE mode with $l = 0, m = 1$ always exists in a fiber. The next one is the HE mode with $l = 1, m = 1$. Therefore, a single-mode operation can be achieved with a $V_{\text{fiber}} < 2.405$.

In the thin part of a tapered fiber, the core and the clad are merged. For an evanescent coupling to a specific whispering gallery mode, a single-mode operation is desired. Thus, propagation in the structure with the fiber (core) and the air (clad) is focused on. The condition of a single-mode operation is described as

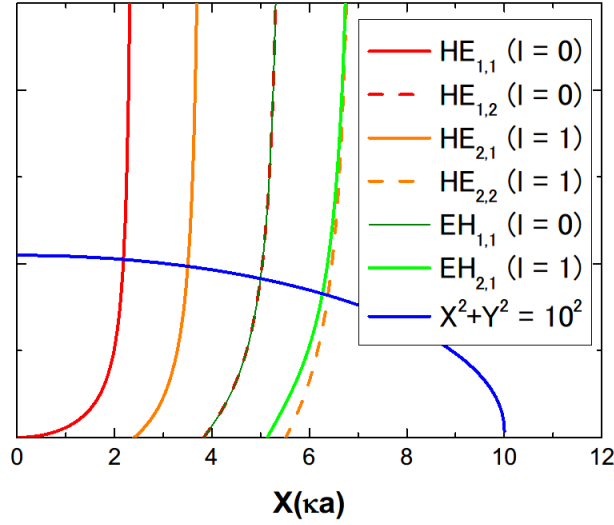


Fig. 2.7: The graph of the characteristics equation for propagating optical modes. This graph shows that the condition $V_{\text{fiber}} < 2.405$ allows single mode propagation..

$$V_{\text{fiber}} = k_0 n_1 a \sqrt{2 \frac{n_1^2 - n_2^2}{2n_1^2}} < 2.405, \quad (2.47)$$

$$a < 0.57, \quad (2.48)$$

with $\lambda = 1.55 \mu\text{m}$, $n_1 = 1.44$, $n_2 = 1$. This is the description of tapered fiber required for measurements of a silica toroid microcavity.

2.5 Theory of nonlinearity

This section describes the nonlinearity studied in this thesis. Three third-order nonlinearity-based phenomena (four-wave mixing, stimulated Raman scattering, and third-harmonic generation) in high- Q microcavities are explained.

2.5.1 Four-wave mixing

The main frequency conversion process of third-order nonlinearity-based non-linear optical effects is four-wave mixing. Optical parametric oscillation with a silica toroid microcavity has been studied³⁾, and the threshold power is basically

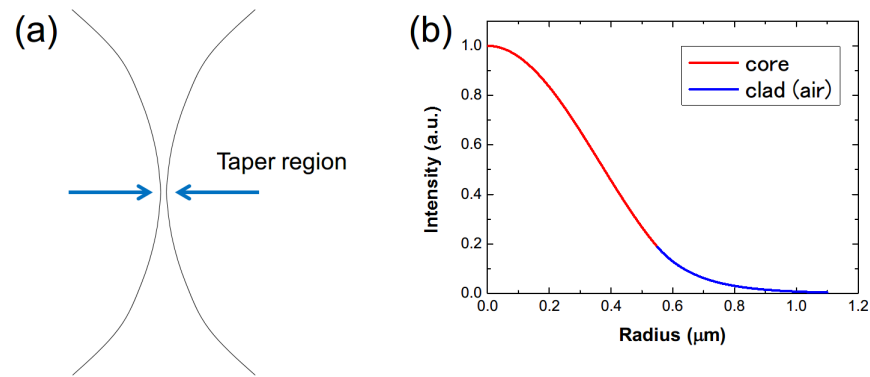


Fig. 2.8: (a) The schematic image of a tapered fiber. (b) The graph of the characteristics equation for the propagating optical mode ($l = 0$) in a tapered fiber with the radius of $0.55 \mu\text{m}$. The wavelength is $1.55 \mu\text{m}$. The inner refractive index n_1 and outer refractive index n_2 are 1.44 and 1.00, respectively. The ratio of the evanescent field in the total mode profile is 14%.

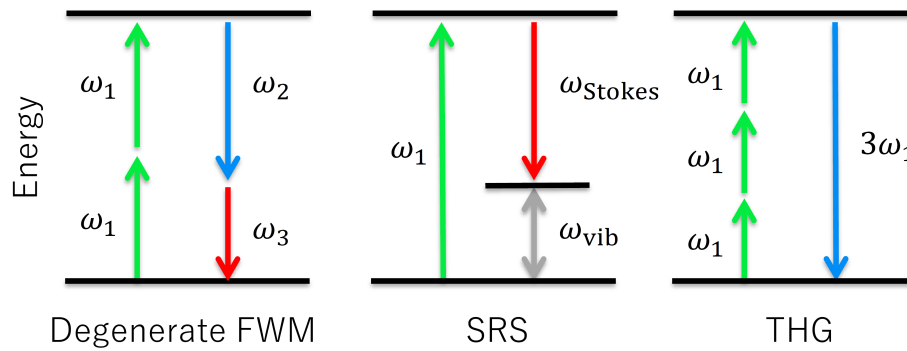


Fig. 2.9: Energy diagrams of third-order nonlinearity effects. Upward and downward arrows mean annihilation and creation of photons. FWM, four-wave mixing; SRS, stimulated Raman scattering; THG, third-harmonic generation.

described as

$$P_{\text{th}} = \frac{2\pi n^2}{\lambda n_2} \cdot \frac{V}{Q^2}. \quad (2.49)$$

Given a Q of 1 million, a V of $1000 \mu\text{m}^3$, an n of 1.44, and an n_2 of $2.0 \times 10^{-20} \text{ W/m}^2$, the calculated threshold power is 420 mW. If Q reaches 10 million, the threshold power rapidly decreases to 4.2 mW. Thus, a high Q is required for best results.

Simply, the point where the first comb line occurs¹⁹⁾ is given by

$$m_{\text{th}} = \sqrt{\frac{2\pi c}{Q\lambda|D_2|} \left(\sqrt{\frac{P_{\text{in}}}{P_{\text{th}}}} - 1 + 1 \right)}, \quad (2.50)$$

where m indicates a mode number counted from a pump mode and the first comb line occurs at the m_{th} mode, and D_2 means a kind of cavity dispersion defined as

$$\omega_m = \omega_0 + D_1 m + \frac{1}{2} D_2 m^2 + \frac{1}{6} D_3 m^3 \dots, \quad (2.51)$$

where ω_0 is a pump mode, ω_m is the m th mode from the pump mode, D_1 is an FSR, D_2 is a cavity dispersion, and D_3 is a third-order dispersion. Thus, the cavity dispersion D_2 is one of the parameters that should be designed.

2.5.2 Stimulated Raman scattering

Since Raman scattering derives from the molecular vibration that is a near-universal phenomenon of materials, there are a number of researchers who study it. The threshold power of stimulated Raman scattering in a silica toroid microcavity^{5,7)} is given by

$$P_{\text{th}} = \frac{\pi^2 n^2 V}{\lambda_p \lambda_R g_R} \frac{1}{Q_{\text{int}}^2} \cdot \frac{27}{4}. \quad (2.52)$$

where λ_p and λ_R are the respective wavelengths of the pump and a Raman mode, g_R is the nonlinear bulk Raman gain coefficient, and Q_{int} is the intrinsic Q factor. V is the effective mode volume.

Given a Q_T of 1 million, a V of $1000 \mu\text{m}^3$, an n of 1.44, a λ_p and a λ_R of 1550 and 1650 nm, and a g_R of $0.6 \times 10^{-11} \text{ cm/W}$, the calculated threshold power is 900 mW,

which is nearly twice as high as the threshold power of four-wave mixing. Ideally, four-wave mixing should be dominant in a microcavity.

2.5.3 Third-harmonic generation

Third-harmonic generation is a simple frequency conversion based on third-order nonlinearity. Since high- Q cavities without second-order nonlinearity dramatically enhance the circulating power inside, third-harmonic light is usually observed^{9,113}. Third-order nonlinearity-based polarization is described as

$$P_{\text{NL}} = \epsilon_0 \chi^{(3)} : \mathbf{EEE}. \quad (2.53)$$

The power generated from a third-harmonic generation with a silica toroid microcavity has been studied⁹, and it is given by

$$P_{\text{TH}} = \left(\frac{\chi^{(3)} \eta_0}{2\epsilon_0 n^2} \right)^2 \left(\frac{P_{\text{in}} Q_p \lambda_p}{2\pi n r A_p} \right)^3 \left(\frac{2\pi r n Q_{\text{TH}}}{A_{\text{TH}} \lambda_{\text{TH}}} \right) \frac{4 \left| \int_{r,z} E_p^3 E_{\text{TH}}^* dA \right|^2}{4(\Delta\omega \tau_{\text{TH}})^2 + 1}, \quad (2.54)$$

where λ_p and λ_{TH} are the respective wavelengths of the pump and a third-harmonic mode, A_p and A_{TH} are the effective mode areas of the pump and a third-harmonic mode, and $\Delta\omega$ is frequency mismatching between the pump mode and the third harmonic mode. The second factor on the right side shows that a third-harmonic power is cubically proportional to the circulating power of a pump mode. The third factor refers to the build-up factor of the third-harmonic light. Also, the last factor indicates a mode overlap between a pump mode and a third-harmonic mode, which means that frequency mismatching strongly influences the third-harmonic power.

2.6 Fabrication

2.6.1 Fabrication of a silica toroid microcavity

For this thesis, a silica toroid microcavity was selected from a number of possible microcavities. There are four main characteristics of this type of cavity^{47,48}:

1. ultrahigh Q ($Q > 10^8$)

2. small mode volume ($V \sim 100 \mu\text{m}^3$)
3. integration on-chip
4. silicon-based advantage

In particular, ultrahigh- Q and small mode volume are extremely important. As noted in the discussion above, a silica toroid microcavity confines as high as 10^6 times the power as the input power P_{in} within the small space, which then reaches the number of gigawatts per square centimeter required for nonlinear optics. Thus, silica toroid microcavities have been researched to demonstrate Raman lasing, optical parametric oscillation, and third-harmonic generation. Since the cavity is fabricated on a common silicon chip, it is possible to integrate it with other optical devices on a single chip. This fabrication method is compatible with conventional semiconductor processes.

The process of fabrication of a silica toroid microcavity is as follows:

1. Silica thermal film growth on a silicon substrate
The quality of the silica influences the absorption loss of a cavity. Thus, thermal growth is required instead of chemical vapor deposition. In thermal growth, there are wet and dry methods. The wet method provides fast growth with a reasonable quality and the dry method makes a high-quality silica film with slow growth. A silica toroid microcavity requires 1- or 2- μm silica films, for which wet thermal growth is commonly selected.
2. Patterning silica on a silicon chip with photolithography
Photomask patterning is utilized to make a circle of a silica film. With semiconductor processes, precise fabrication is possible. Within reason, shapes other than circular ones (e.g. octagonal or slightly deformed) can be used for a silica toroid microcavity.
3. Silicon sacrificial layer etching
To make an SiO_2 disk structure on an Si post, part of the silicon is etched as a sacrificial layer. XeF_2 gas etching with a high selection rate is appropriate. Another approach is wet etching with an HNA (hydrofluoric acid, nitric acid, and acetic acid) system, which can be utilized with the same purpose.

4. CO₂ laser reflow to melt silica

A CO₂ laser irradiates the silica film from the top. The silica absorbs heat from the CO₂ laser and eventually reaches the melting point. The melted part shrinks and forms a toroidal structure, due to a surface tension. The silicon post works as a heat sink that stops the melting. When heating and cooling are balanced, further melting will not occur unless the irradiating power is increased.

Figure 2.11 shows experimental results of the fabrication of a silica toroid microcavity. In this study, mask patterns were used to make circular shapes with diameters of 100 or 150 μm.

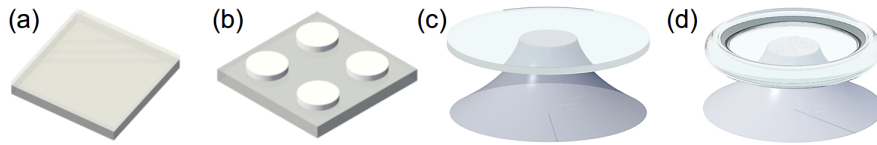


Fig. 2.10: The process of fabrication of a silica toroid microcavity. (1) Thermal oxidizing silicon substrate. (2) Photolithography for patterning circular silica forms. (3) Sacrificial layer etching for making a silica disk cavity. (4) Laser reflow process to form a silica toroid structure.

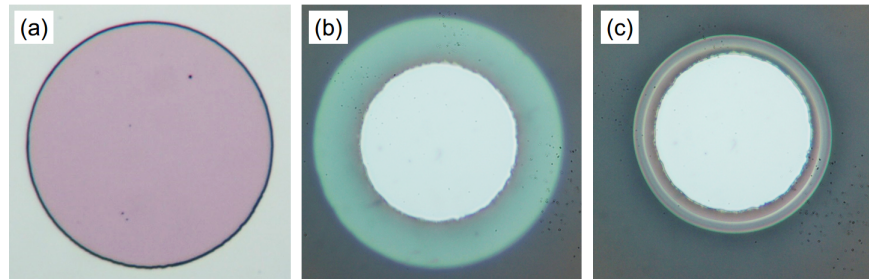


Fig. 2.11: Optical microscope images of (a) a mask pattern with diameters of 100 μm (b) a disk cavity (c) a silica toroid cavity. The white circle in (b) and (c) is the silicon post supporting the silica disk.

2.6.2 Fabrication of a tapered fiber

In this thesis, a tapered fiber was used as an evanescent coupler between a light and a silica toroid microcavity. As mentioned above, a tapered fiber is easily broken because its diameter at the thinnest part is nearly 1 μm, so it is sufficient for a single-mode operation.

A fabrication method is as follows:

1. The coating of a commercial single-mode fiber is removed.
2. The fiber is heated until it reaches the softening point of silica glass.
3. The fiber is pulled slowly to prevent thermal cracking.

A special device is used to fabricate a tapered fiber by this process. It uses a burner, from which a mixture of gases (oxygen and propane) flows. Figure 2.12 shows transmittance fluctuation during the pulling. At first, the transmittance is stable because a single-mode propagation occurs in the core and the clad. However, a large fluctuation occurs in the middle of the pulling, because the core and the clad are merged by compression and reach multi-mode operation. Finally, the transmittance becomes stable again. It is thought that a single-mode operation is achieved with a core of fiber and a clad of air. In the experiment, the parameters that control heating and pulling are strict and are selected to prevent thermal cracking that would severely decrease the transmittance.

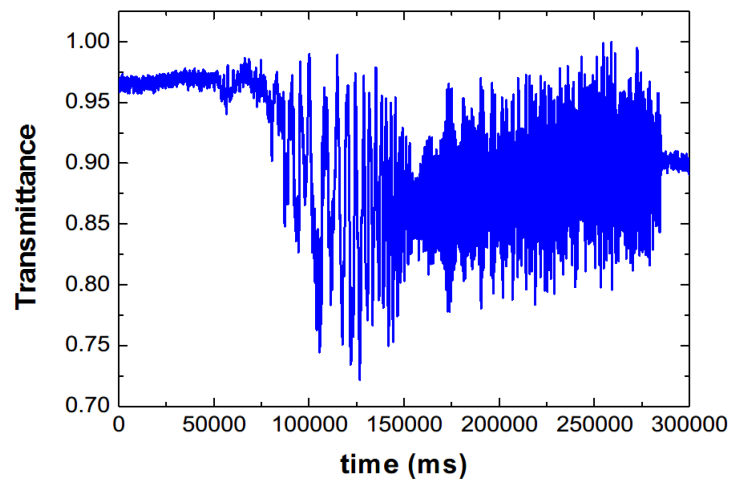


Fig. 2.12: A graph showing transmittance power in a tapered fiber while the fiber is being pulled by a machine. The first region shows this fiber as a single-mode fiber. The second region shows the fiber allowing the multi-mode to propagate, due to the change in width of the core and the clad. The final region shows the fiber becoming a single-mode fiber, where the core is glass and the clad is air.

2.7 Optical measurement methods

In this section, optical measurement methods are showed. First, Q -factor measurement is explained. Q -factor is the most important factor of experiments of third-order nonlinearity because it strongly determines the threshold powers. Next, measurements of nonlinearity are explained.

2.7.1 Measurement of Q -factor

To measure Q s experimentally, there are two main methods:

1. Measurement of the FWHM of a resonant spectrum $\Delta\nu$ with a tunable laser diode.
2. Measurement of the photon lifetime τ_p with a repeatable pulse train (ring-down method).

The former is a simple method requiring a tunable laser with a scanning function. Although the latter requires multiple devices (a continuous-wave laser, an electro-optic modulator, and an oscilloscope), its precision is higher than that of the former, which is determined by the accuracy of the wave meter in the tunable laser.

First, FWHM measurement is explained. Figure 2.13(a) is the experimental setup to obtain the data as shown in Figure 2.14 (a). Note that careful control of the coupling point is required for efficient coupling. To achieve phase-matching between the cavity mode and the mode in the tapered fiber, changes of the coupling point of the fiber is effective because the diameter of the fiber determines a propagation constant of the mode in the fiber. The spectrum was obtained using the wavelength scan of a tunable laser diode with 200 kHz linewidth (Santec TSL-710) and a power meter (Agilent 8163B) to measure the transmittance. The dips spaced equidistantly indicate a whispering gallery mode, and a Q of 4.0×10^5 was calculated from the FWHM. Next, the ringdown method is described. The Q is calculated from the photon lifetime (the decay rate) directly. The advantage of this method is the robustness against the heat in a cavity, in addition to the high precision. A thermo-optic effect is the main cause of deformation of the spectrum, because it changes resonant frequencies dynamically during a

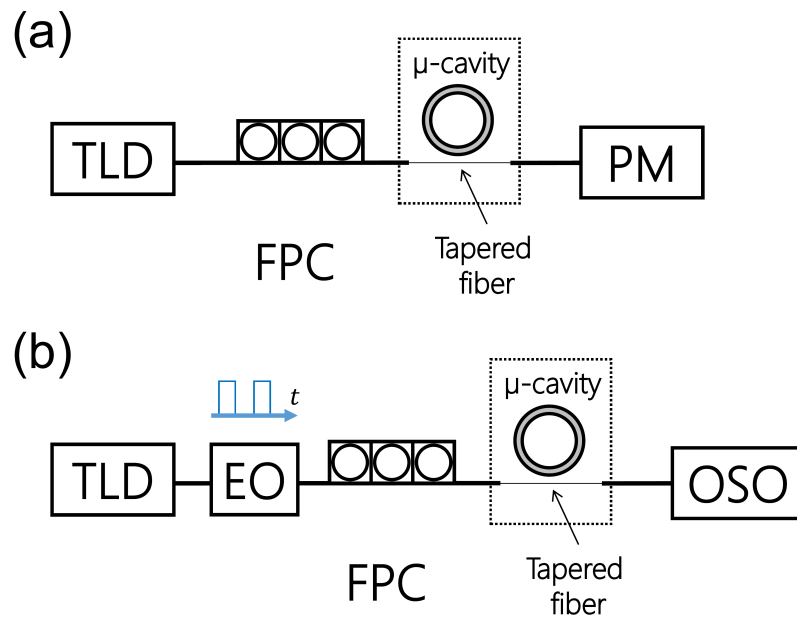


Fig. 2.13: Experimental setup of measurement of Q -factor

(a) Experimental setup for measurement of the FWHM. TLD, tunable laser diode (Santec TSL-710); FPC, fiber polarization controller (Thorlabs FPC560); PM, power meter (Agilent 8163B). A tapered fiber is aligned closely at the surface of the toroid microcavity to couple light evanescently. (b) Experimental setup for measurement of the photon lifetime. EO, electro-optic modulator; OSO, optical sampling oscilloscope.

measurement. Since the ringdown method is not influenced by heat, the Q of a cold cavity can be measured with high reliability. Figure 2.13(b) shows an experimental setup that contains an electro-optic modulator generating a repeatable rectangular wave. The output signal is shown in Figure 2.14(c). After trailing edge of the pulse, the cavity releases the confined light with a certain decay rate. By measuring the decay rate, the Q is calculated as shown in Figure 2.14(d).

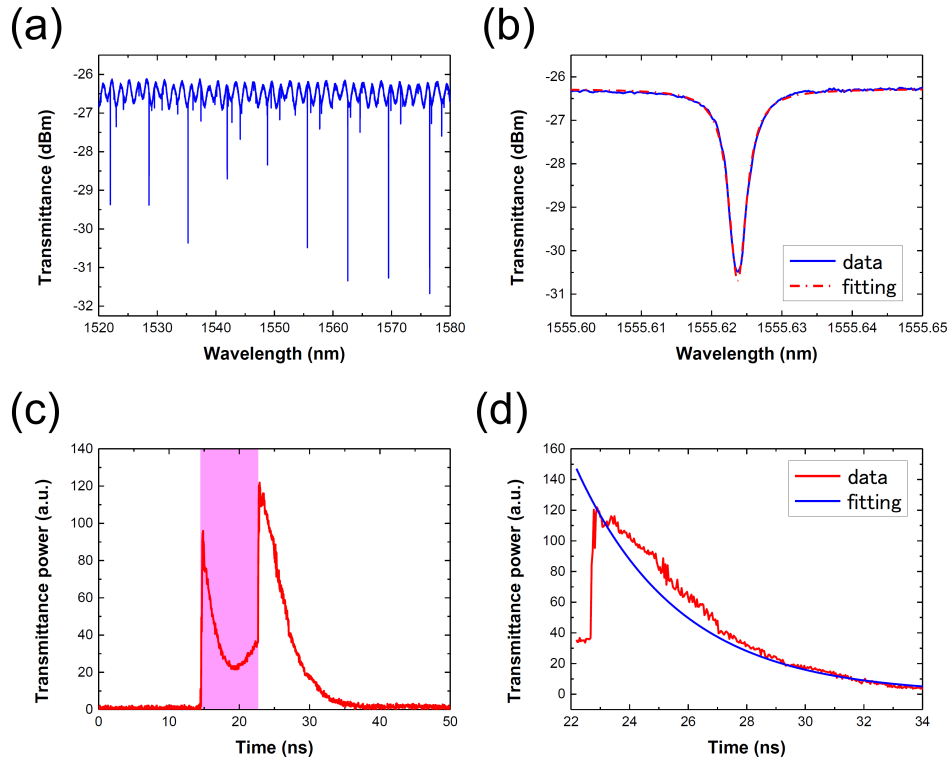


Fig. 2.14: Calculation method from the experimental data

(a) Typical transmission spectrum of side coupling systems. Equidistant dips mean resonant wavelength of a measured cavity. (b) Magnification of (a). Lorentz fitting shows the FWHM and the Q . (c) Typical transmission signal when a square pulse is inputted. A shadow means the inputted pulse width. (d) Magnification of (c). The decay rate shows the photon lifetime of the cavity.

2.7.2 Measurement of nonlinearity

To measure nonlinearity, some specific components are required in addition to the setup for Q -factor measurement.

Third-order nonlinearity requires high optical power even though high- Q cav-

ities build up the optical power inside. To compensate it, erbium-doped fiber amplifier (EDFA) is used. A common EDFA amplifies an input power up to 1 W, which is sufficient to induce nonlinearity in cavities. The precise control of the input power is required for control of nonlinearity. Thus, a variable optical attenuator which controls the attenuation with the unit of 0.01 dB is used. Output signal is evaluated with an optical spectrum analyzer and a power meter. SHG auto-correlator is used for pulse-width measurement. Figure 2.16(a) is a measured spectrum. The pump at 1553 nm is inputted to the cavity and five lines are generated via four-wave mixing. They are coupled to the tapered fiber and evaluated with the optical spectrum analyzer. Since four-wave mixing is the coherent process, the linewidth of generated lines should be around 200 kHz which is the linewidth of the input laser. Figures 2.16(b) and (c) are optical images of visible light emission resulting from third-harmonic generation. Visible light is not coupled to the tapered fiber due to phase-mismatching. Thus, telescopes collect light in space and couple it to a multimode fiber connecting with a spectrometer.

To measure the efficiency of third-harmonic generation, there are two methods. One is that the third-harmonic light is withdrawn with a tapered fiber which is for visible light¹¹⁴⁾. This way makes, however, the experimental setup more complex because a thinner or a bended tapered fiber is required for collecting visible light. Another is that the efficiency is estimated by the scattered light collected with telescopes¹¹⁵⁾. The scattered light power depends on intracavity third-harmonic power and surface roughness of the cavity, and the surface roughness can be estimated by the surface tension of the material or measured with atomic force microscopy. With the scattered light power and the surface roughness, the intracavity power can be estimated.

When the high power (≈ 1 W) is used, the intracavity power exceeds 4000 W for the cavity with the Q of 1 million. Moreover, the optical density P_{cav}/V reaches the order of GW/cm^2 . Although the absorption loss of the cavity is considerably small, the influence of appearing heat should be noted. The heating can be estimated by resonance shifts by a thermo-optic effect^{64, 116)}. The amount of the thermal shift $\Delta\lambda$ is given by

$$\Delta\lambda = C\lambda_0\Delta T, \quad (2.55)$$

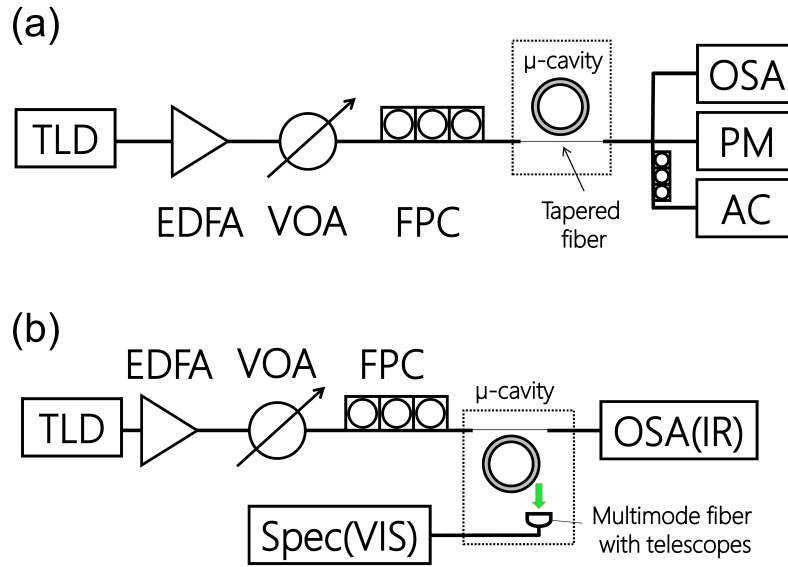


Fig. 2.15: Experimental setup for measurement of nonlinearity
 (a) Experimental setup of measurement of four-wave mixing and stimulated Raman scattering. TLD, tunable laser diode (Santec TSL-710); EDFA, erbium-doped fiber amplifier (Pritel PMFA-30); VOA, variable optical attenuator (OZ Optics DA-100); FPC, fiber polarization controller (Thorlabs FPC560); OSA, optical spectrum analyzer (Yokogawa AQ6375); PM, power meter (Agilent 8163B); AC, SHG autocorrelator (APE Berlin pulseCheck). A tapered fiber is aligned closely at the surface of the toroid microcavity to couple light evanescently. (b) Experimental setup for measurement of third-harmonic generation. Spectrometer is used to evaluate visible light emitted from the cavity. Visible light is collected with telescopes. Spec, spectrometer (Ocean Optics USB2000+).

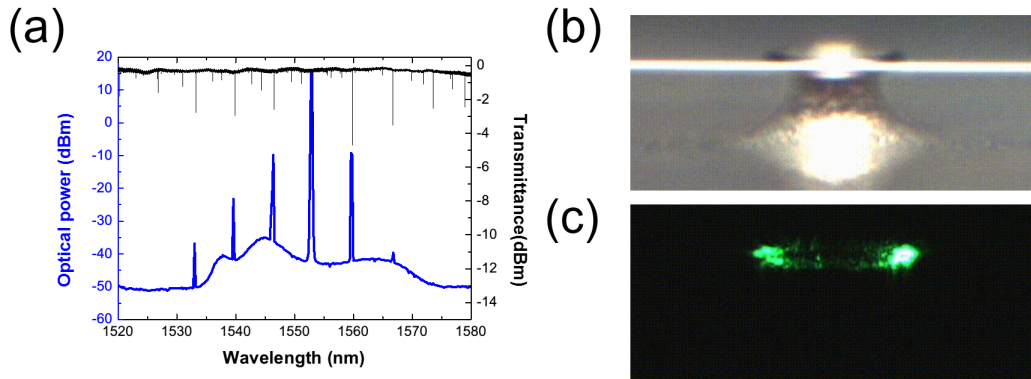


Fig. 2.16: (a) Optical spectrum resulting from four-wave mixing. Blue line shows outputs measured with OSA. Black line shows transmittance spectrum of the cold cavity measured with PM. (b) Optical image of the side view of the cavity connecting a tapered fiber. The object is observed with telescopes. (c) Green light emission from the cavity. The visual point is same as (b). The emission is evaluated with a spectrometer.

where C , λ_0 and ΔT are the thermo-optic coefficient, the resonant wavelength of the cold cavity, and the amount of internal temperature change, respectively. Figure 2.17 shows the typical thermal shifts when the input wavelength is scanned from short to long wavelength. The measured shift is 0.55 nm. Since the $C = 5.2 \times 10^{-6} \text{ K}^{-1}$ for silica, the internal temperature rises by about 70 K. Considering the room air temperature is 20°C , the internal temperature should be 90°C . Most heat dissipates through the silicon post of the cavity because of the high thermal conductivity of silicon. Although the dissipation through the air can be considered, it is negligible because the thermal conductivity of air is 5 orders of magnitude smaller than that of silicon.

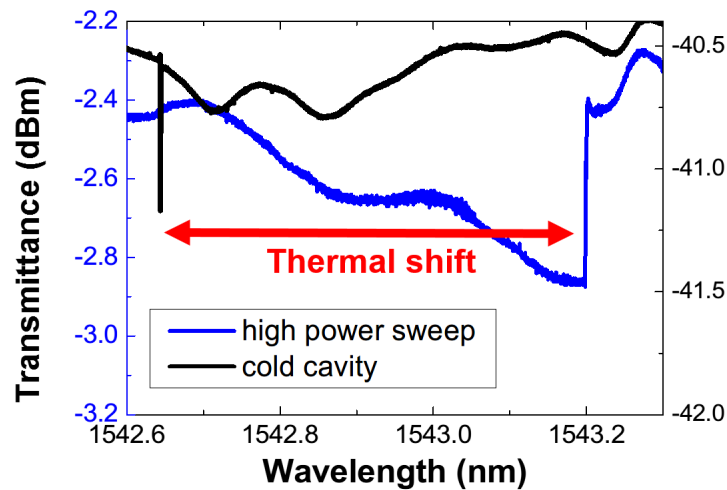


Fig. 2.17: Thermal shift of the resonance when the input wavelength is scanned from short to long wavelength. Black and blue lines show transmittance spectrum with low-power scanning and high-power scanning, respectively. At high-power scanning, the shift caused by thermo-optic effect is about 0.55 nm, which indicates that the internal temperature change of the cavity is about 70 K.

2.8 Summary

In this chapter, mathematical descriptions related to high- Q cavity, build-up factor, optical modes in silica toroid microcavity and tapered fiber were explained. Third-order nonlinearity-based optical processes (four-wave mixing, stimulated Raman scattering, and third-harmonic generation) in a cavity were described. Moreover, fabrication methods of a silica toroid microcavity and a tapered fiber

were described. Finally, measurements of Q -factor and nonlinearity with a silica toroid microcavity were explained.

Chapter 3

Hysteresis behavior of microcomb generation

This chapter describes hysteresis behavior of microcomb generation using a silica toroid microcavity. This mechanism of microcomb generation has been researched for the last decade, and many studies have demonstrated how to control the generation, especially mode-locked microcomb generation. This chapter focuses on hysteresis behavior of nonlinear cavities and explores the dependence of a microcomb on the history of the cavity. In this context, a novel method for producing a mode-locked microcomb was proposed and experimentally demonstrated.

Section 3.1 shows a Lugiato-Lefever equation developed from a nonlinear Schrödinger equation, which is a reasonable model for analyzing microcomb generation. Section 3.2 explains dispersion engineering of a silica toroid microcavity, which is needed for obtaining a microcomb. Section 3.3 describes hysteresis behavior of a nonlinear cavity with a Lugiato-Lefever model. Section 3.4 shows experimental results indicating that a mode-locked microcomb can be generated by a novel method.

3.1 Lugiato-Lefever equation

This section describes a Lugiato-Lefever equation, which is a reasonable model for analyzing microcomb generation^{117,118}). For a ring cavity with a continuous-wave input, the combination of a nonlinear Schrödinger equation and a coupled mode theory is required for understanding the nonlinear dynamics in the cavity. A Lugiato-Lefever equation is a simplified form that combines two equations with a generalized mean-field approximation¹¹⁹). A Lugiato-Lefever equation can be calculated with a split-step Fourier algorithm⁵¹), and it clearly describes the behavior of a nonlinear cavity.

With the slowly varying envelope approximation, a Luagito-Lefever model is described as⁶⁰)

$$t_R \frac{\partial E(n, \tau)}{\partial n} = \left(-\frac{\alpha L}{2} - \frac{T}{2} - i\delta + iL \sum_{k \geq 2} \frac{\beta_k}{k} (-i \frac{\partial}{\partial \tau})^k + i\gamma L |E|^2\right) E + \sqrt{T} E_{\text{in}}, \quad (3.1)$$

where $E(n, \tau)$ is the electric field in a cavity. n and τ are the round trip number, a short time, respectively. t_R , α , T , L , δ , β_k , γ , and E_{in} correspond to a round trip time, intrinsic loss per unit length, a coupling coefficient, a cavity length, a wavelength detuning, k -th order dispersion, a nonlinear coefficient, and the driving field, respectively. With a split-step Fourier algorithm, Equation 3.1 can be solved and nonlinear dynamics in the cavity is analyzed.

It is worth pointing out a relationship between Q and some parameters in a Lugiato-Lefever equation, because it is simpler to measure a Q than to measure propagation loss. First, a Q is described as

$$Q = \omega \tau_p = \omega \frac{1}{c \alpha_r}, \quad (3.2)$$

where α_r is the loss coefficient per unit length. From this, the relationship between Q and propagation loss is derived as

$$\alpha L = \frac{\omega}{c Q_{\text{int}}} L. \quad (3.3)$$

Here, the Q in Equation 3.2 corresponds a Q_{int} . The coupling T has a relationship written as

$$T = \frac{\omega}{cQ_c}L. \quad (3.4)$$

With Equations 3.3 and 3.4, a measured Q can be used in the analysis of a Lugiato-Lefever equation.

3.2 Dispersion parameters of a silica toroid microcavity

In a Lugiato-Lefever equation, cavity dispersion is a key factor for determining the behavior of a nonlinear ring cavity. For example, there is hardly any gain of four-wave mixing in the normal dispersion region. Thus, anomalous dispersion is essentially required for microcomb generation, so that the dispersion engineering of a cavity is needed^{120–126}). In this section, the cavity design of a silica toroid microcavity is explained.

A cavity dispersion consists of a material-based and a geometry-based dispersion. The former depends on the material of a cavity, and the parameters of each material must already be known through use of the Sellmeier equation. The Sellmeier equation shows the frequency dependence of the refractive index of a material. It is described as

$$n^2(\omega) = 1 + \sum_{j=0}^m \frac{A_j \omega_j^2}{\omega_j^2 - \omega^2} \quad (3.5)$$

where A_j and ω_j are peculiar constants of a material. For fused silica, these are as follows¹²⁷):

$$\begin{aligned} A_1 &= 0.6961663 \quad , \quad \lambda_1 = 0.0684043 \text{ } \mu\text{m}, \\ A_2 &= 0.4079426 \quad , \quad \lambda_2 = 0.1162414 \text{ } \mu\text{m}, \\ A_3 &= 0.8974794 \quad , \quad \lambda_3 = 9.896161 \text{ } \mu\text{m}. \end{aligned} \quad (3.6)$$

Next, a geometric dispersion is discussed. It physically derives from the frequency dependence of the spatial profile of a mode. For a typical ring cavity, the longer a wavelength, the smaller the effective refractive index of the mode. This is because the mode area becomes large and is felt strongly outside the cavity. For a silica toroid microcavity, not only the extent of the mode profile but also the effective radius of the mode is frequency-dependent. Generally, it is hard to estimate the geometric dispersion analytically. Thus, a finite-element method (FEM) is commonly used.

There are two main parameters of a silica toroid microcavity as shown in Figure 3.1: the major radius and the minor radius. Since the thickness of a silica film on silicon can be changed, it is possible to control the minor radius experimentally. The major radius determines the cavity length and the FSR, which is selected according to need. In contrast, the minor radius can be designed mainly for dispersion engineering.

Figure 3.2 shows the dispersion of the fundamental mode (TE_{00}) when the cavity parameters are changed. The major radius dependence of the cavity dispersion appears in Figure 3.2(a) in which three major radii (30, 50 and 80 μm) are considered. Figure 3.2(b) shows the minor radius dependence of the cavity dispersion. From these results, a large major radius and a small minor radius are required for obtaining anomalous dispersion in the telecom region.

Mode dependence of the cavity is shown in Figure 3.3. Three modes (TE_{00} , TE_{01} , and TE_{10}) are considered. The dispersions are clearly different. Although the selection of modes seems to be important, the TE_{00} is used because the TE_{00} usually exhibits the highest- Q among all the modes.

3.3 Hysteresis behavior of microcomb generation

In this section, hysteresis behavior of nonlinear cavities and microcomb generation are discussed. First, the steady state of a Lugiato-Lefever equation is explained. A nonlinear cavity exhibits a bistability caused by the Kerr effect. Since intracavity power influences a microcomb, analysis of the behavior of the intracavity power makes the mechanism of a microcomb clear. This section uses a numerical simulation to analyze microcomb generation. Then, a novel way to

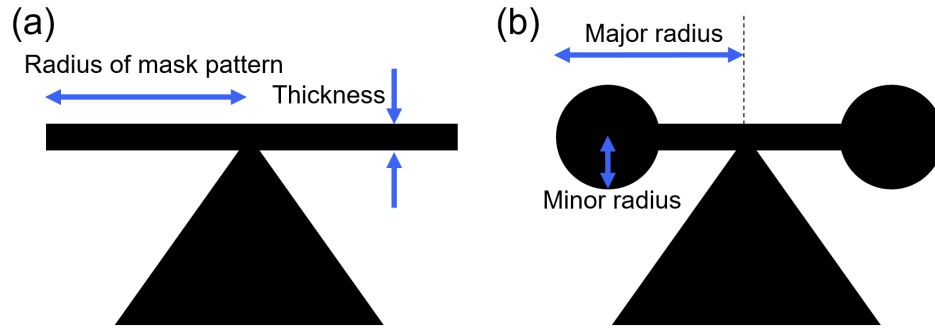


Fig. 3.1: Schematic images of a silica toroid microcavity (a) before CO₂ laser reflow and (b) after CO₂ laser reflow.

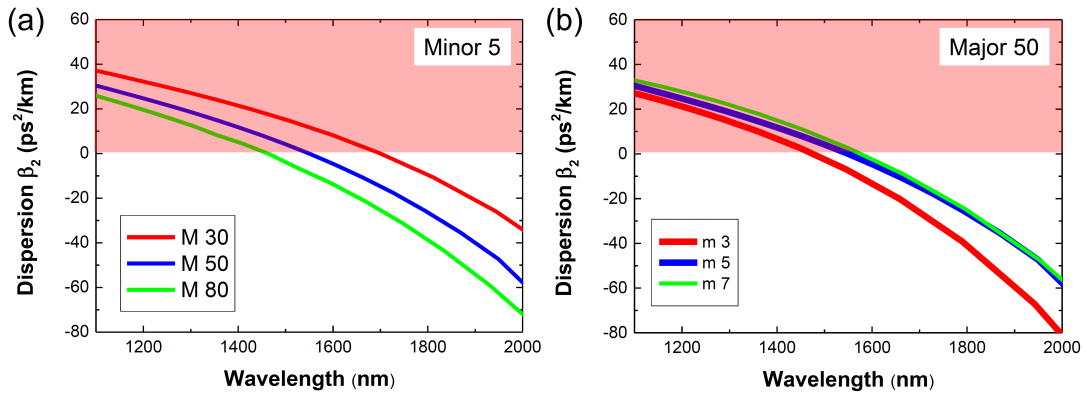


Fig. 3.2: Calculated dispersion of the fundamental mode in a silica toroid microcavity. Anomalous dispersion is required for optical parametric conversion. (a) Different major radii with a minor radius of 5 μm . (b) Different minor radii with a major radius of 50 μm .

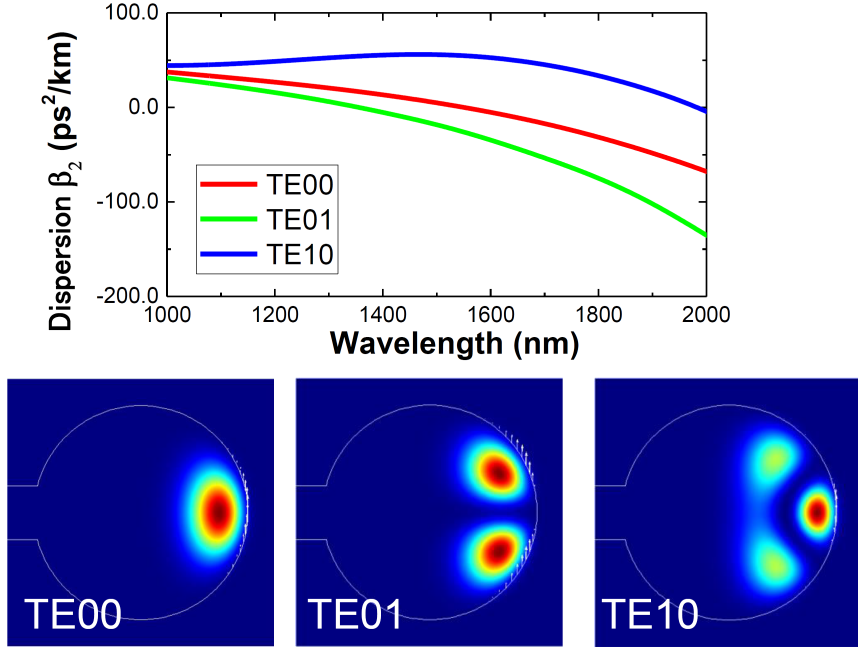


Fig. 3.3: Calculated dispersion of different modes in a silica toroid microcavity with a major radius of 50 μm and a minor radius of 4 μm .

achieve a mode-locked microcomb is proposed.

Before numerical analysis, a bistability caused by the Kerr effect is explained. A bistability means that a system provides two independent stable outputs from the same input. Output selection depends on the history of the system. Thus, how an input is controlled is interesting in the context of bistability. A bistability caused by the Kerr effect is expressed with the equation developed by Gibbs *et al.*¹²⁸⁾. Given a steady-state of a Lugiato-Lefever equation, the equation is derived as

$$E_{\text{in}}^2 = |E_{\text{cavity}}|^2 \{1 + (|E_{\text{cavity}}|^2 - \Delta)^2\}, \quad (3.7)$$

where Δ is the normalized detuning, which is a decisive parameter. Following variable transformation, a steady-state of Equation 3.1 transforms Equation 3.7:

$$\frac{\alpha L + T}{2} \rightarrow \alpha_{\text{norm}}, \quad n \rightarrow \frac{\alpha_{\text{norm}}}{t_{\text{R}}} t, \quad \tau \rightarrow \sqrt{\frac{2\alpha_{\text{norm}}}{|\beta_2|L}} \tau$$

$$E \sqrt{\frac{\gamma L}{\alpha_{\text{norm}}}} \rightarrow E, \quad E_{\text{in}} \sqrt{\frac{\gamma L T}{\alpha_{\text{norm}}^3}} \rightarrow S, \quad \Delta = \frac{\delta}{\alpha_{\text{norm}}}$$

Note that the normalized Lugiato-Lefever equation^{129,130}) is described as

$$\frac{\partial E(t, \tau)}{\partial t} = \{-1 + i(|E|^2 - \Delta) - i\eta \frac{\partial^2}{\partial \tau^2}\} E + S, \quad (3.8)$$

where η is a sign of β_2 . Given that $|E_{\text{in}}|^2 = X$ and $|E_{\text{cavity}}|^2 = Y$, the relationship is derived as

$$X = Y^3 - 2\Delta Y^2 + (\Delta^2 + 1)Y. \quad (3.9)$$

With Equation 3.8, the behavior of a steady-state of a cavity is analyzed. Figure 3.5(a) shows a set of solutions when $Q_{\text{int}} = 2 \times 10^7$ and $Q_{\text{couple}} = 2 \times 10^7$. It is clear that the detuning, δ , strongly influences the intracavity power. Figure 3.5(b) mentions that coupling of Q depends on the intracavity power. The weaker the coupling, the smaller the fluctuation of the intracavity power. This analysis of a steady-state shows that the hysteresis of the cavity should be considered in controlling nonlinear dynamics.

Next, a mode-locked microcomb is calculated with a simple case. The calculated parameters are: $Q_{\text{int}} = 1 \times 10^7$, $Q_{\text{couple}} = 1 \times 10^7$, $\beta_2 = -3 \text{ ps}^2/\text{km}$, $\beta_3 = -0.01 \text{ ps}^3/\text{km}$, $\gamma = 5 \times 10^{-9} \text{ W}^{-1} \mu \text{ m}^{-1}$, $f_{\text{FSR}} = 200 \text{ GHz}$, $L = 1.041 \text{ mm}$, and calculated mode number $N = 128$.

Table. 3.1: The parameters for the calculation for Figure 3.8.

Q_{int}	1×10^7	γ	$5 \times 10^{-9} \text{ W}^{-1} \mu \text{ m}^{-1}$
Q_{couple}	1×10^7	f_{FSR}	200 GHz
β_2	$-3 \text{ ps}^2/\text{km}$	L	1.041 mm
β_3	$-0.01 \text{ ps}^3/\text{km}$	N	128

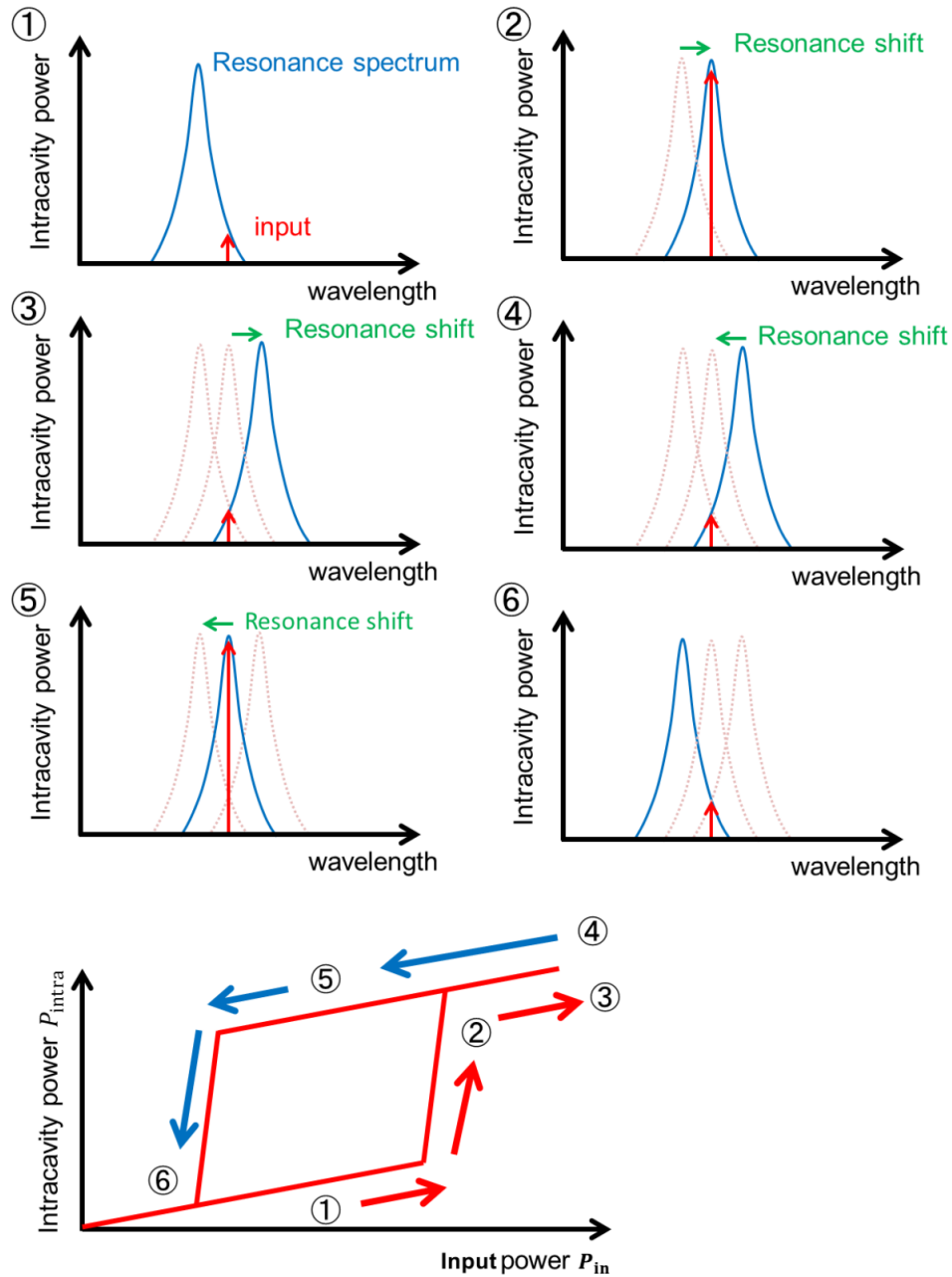


Fig. 3.4: Bistability system caused by the Kerr effect.

1. A red-detuned driving field is inputted. 2. The Kerr effect causes a red frequency shift of the resonant frequency, which makes the intracavity power drastically high. 3. Too high input power causes a large frequency shift. 4. Input power decreases. 5. A high intracavity power is maintained in spite of the decreased input power. This is the upper state of the bistability. 6. The system exhibits one output.

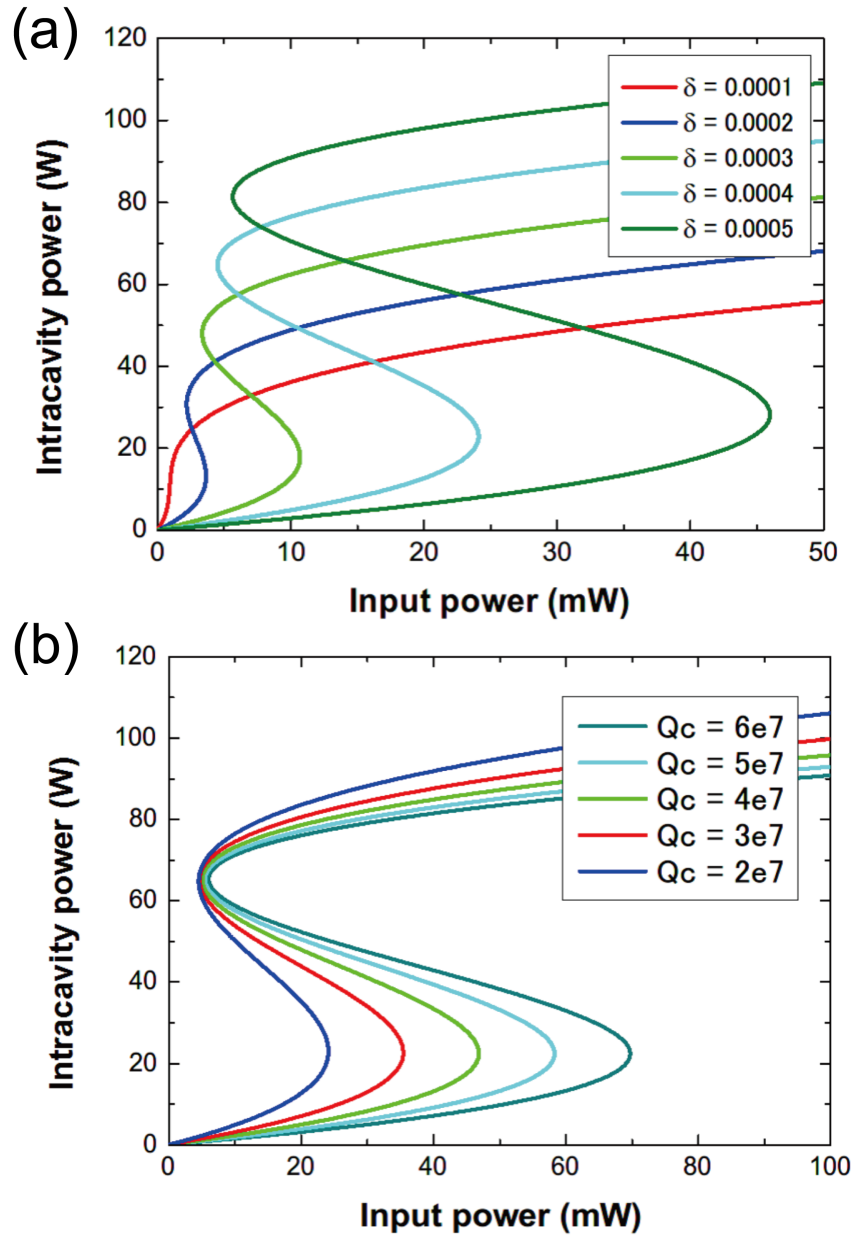


Fig. 3.5: (a) The behavior of the intracavity power when the launched power is changed. Each condition is different in terms of detuning. (b) The behavior of the intracavity power when the launched power is changed. Each condition is different in terms of coupling Q .

Figure 3.6(a) shows an intracavity power transition during a wavelength scan with an input power of 20 mW. On the x-axis, zero means the original frequency of the pump mode. Due to the Kerr effect, which causes an increase in the refractive index, the resonant frequency is shifted towards red. The scan follows the redshift, and the intracavity power gradually becomes high. When the intracavity power is over a threshold of four-wave mixing, frequency conversion starts to occur. The first stage of frequency conversion in microcomb generation is called the Turing pattern, which occurs with effectively blue detuning. Turing patterns have a modulation-like temporal waveform. With further increase of the intracavity power, a chaotic oscillation occurs. Following the chaotic state, there are step-like transitions. In this region, the detuning is effectively red, and cavity solitons occur, which also leads to mode-locking. The step-like transition means that the number of cavity solitons decreases one by one (though multiple decreases can also occur). Thus, the final state has a single soliton in the cavity. This is called the "soliton step," and it proves that cavity solitons occur. The reason the transitions occur is that each pulse behaves to satisfy a soliton condition requiring a balance between a dispersion and the Kerr effect, in addition to a balance between gain and loss. When a certain soliton cannot satisfy the condition, the soliton collapses, and the rest of the energy from the collapsed soliton moves to other existing solitons, which makes the others stable again. From the point of view of hysteresis, this region is the upper state of an "S-character" curve, because the intracavity power has already experienced a much higher state with a chaotic oscillation. Thus, a wavelength scan is not always required. Figure 3.6(c) shows an intracavity power transition with an input power control at a fixed detuning. The power is controlled from low to high and from high to low. At the downward slope, cavity solitons occur. It is clear that microcomb generation depends on hysteresis of the cavity. This is the complementary way for the wavelength scanning method to obtain a microcomb¹⁷⁾. It is worth noting that the input power control should be more effective than the input wavelength control, because a severe control is required at the soliton steps, and a precise scanning laser is more expensive than a precise attenuation tool for controlling the input power. In addition, there is no reasonable scanning laser for the ultraviolet, visible, and mid-infrared regions. Therefore, I propose the input power control as a

novel way to obtain a mode-locked microcomb.

Next, a silica toroid microcavity is set as a model. The parameters are: major radius = 30 μm , minor radius = 2 μm , $Q_{\text{int}} = 5 \times 10^6$, $Q_{\text{couple}} = 5 \times 10^6$, $\gamma = 3.686 \times 10^{-8} \text{ W}^{-1} \mu \text{ m}^{-1}$, $f_{\text{FSR}} = 1100 \text{ GHz}$, and calculated mode number $N = 128$. The dispersion is calculated to fit the model.

Table. 3.2: The parameters for the calculation for Figure 3.9.

Q_{int}	5×10^6	γ	$3.686 \times 10^{-8} \text{ W}^{-1} \mu \text{ m}^{-1}$
Q_{couple}	5×10^6	f_{FSR}	1100 GHz
Major radius	30 μm	N	128
Minor radius	2 μm		

When the normalized detuning, Δ , is set higher than $\sqrt{3}/2$ times the FWHM, hysteresis of the system is obtained. Since the theoretical Equation 3.8 shows the behavior of the intracavity power with no frequency conversion, the point at which a deviation from the theoretical curve occurs indicates the threshold power of frequency conversion. The black lines in Figures 3.7(b) and (c) show a theoretical curve for Equation 3.8. Figure 3.7(b) shows an intracavity power transition as a function of the input power when $\Delta = \sqrt{3}/2$. The power in the cavity is recorded at 0.55 mW/ μm while input power changes. Note that the point where input power is 12 mW is the threshold of frequency conversion. Figure 3.7(b) shows that only 2-FSR mode-locking is obtained. When the input is increased, the cavity enters an unstable regime. Figure 3.7(b) also shows that 1-FSR mode-locking cannot be obtained even when the input power is carefully controlled. The result shown in Figure 3.7(c) is the case where the normalized detuning is $\Delta = 1.25$. A single soliton state can be obtained when the input power is decreased after strong pumping. Thus, these numerical results show the possibility of obtaining a mode-locked microcomb in a silica toroid microcavity with a certain method.

3.4 Experimental results

In this section, I show experimental results with a fabricated silica toroid microcavity. First, changes in comb spacing with changes in input power and coupling

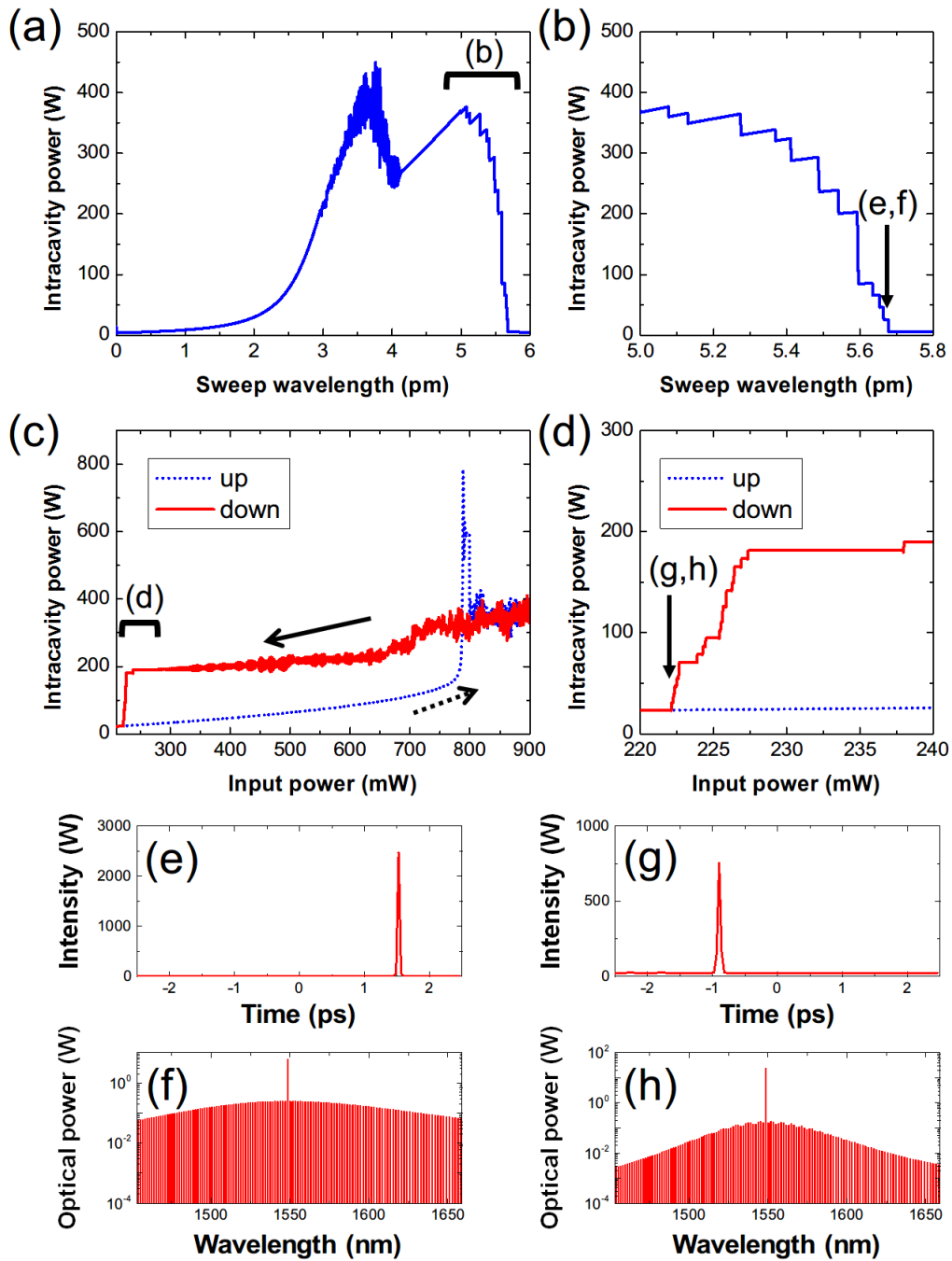


Fig. 3.6: Calculated results for a simple condition. (a) Intracavity power with wavelength sweep. (b) Magnification of a part of (a). (c) Intracavity power with input power change. (d) Magnification of a part of (c). (e-h) Spectra and temporal waveforms of each point in (b) and (d).

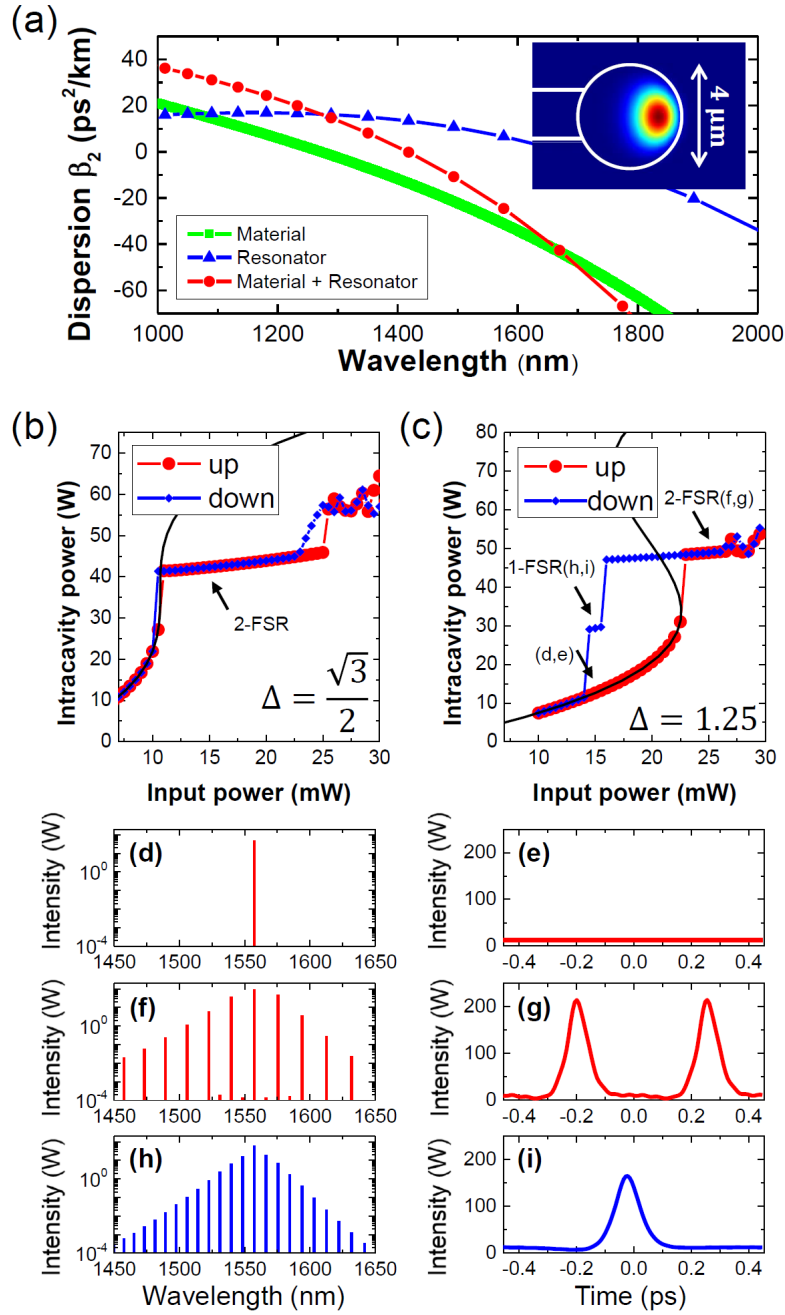


Fig. 3.7: (a) Calculated dispersion of a silica toroid microcavity with a major diameter of 60 μm . (b) Calculated intracavity power as a function of the input power when the normalized detuning of the input laser is $\Delta = \sqrt{3}/2$ from the resonance of the cavity. (c) Same as (b), but with detuning of $\Delta = 1.25$. (d-i) Spectra and temporal waveforms at different input powers. The corresponding points are shown in (c).

strength are demonstrated. Next, the measurement of soliton steps is explained, which is in agreement with a numerical simulation. Finally, some data on the temporal waveform of a microcomb are shown.

The experimental setup is shown in Figure 3.8. Although a typical Q of a silica toroid is nearly 100 million, the device in this experiment exhibited a Q of 5 million for several reasons, including OH absorption. Thus, EDFA, which amplifies up to 1 W, was used. After EDFA, there is a variable attenuator to control input power precisely. I used a wavelength scan partially although an input power control should be demonstrated. This is because very high input power was required for eliciting hysteresis behavior, due to the fact that the fabricated device had a comparatively low Q . However, an advantage of input power control is precise control in soliton step regions. Thus, a wavelength scan was used for rough control and an input power control for precise control in this experiment. Figure 3.9(a) shows the optical spectrum when the cavity was pumped at 433 mW. The spectrum shows a 2-FSR microcomb, which should be in the upper branch with respect to hysteresis. Hence, with careful decrease of the input power, the spectra as shown in Figures 3.9(b) and (c) were observed. It was demonstrated that the 2-FSR microcomb changed to a 1-FSR microcomb with only input power control. Next, since a tapered fiber was used in this experiment, its control ability was investigated. First, an optical spectrum was obtained, as shown in Figure 3.10(a). The distance between the fiber and the cavity was changed, which meant that the coupling coefficient was controlled. Figures 3.10(a-d) show optical spectra (1, 2, 3, and 4-FSR comb) with an approach distance of 50, 190, and 240 nm, respectively. This control also influences microcomb formation, although this is not usually feasible, because a tapered fiber is vulnerable to the external environment.

Next, the measurement of a soliton step with a silica toroid microcavity is described. A power meter is required to measure a transmitted power indicating an intracavity power indirectly. First, a 2-FSR microcomb was obtained with a wavelength scan. After that, the input power was decreased while measuring the transmitted power. Figure 3.11(b) shows the transition of the transmitted power during the decrease of the input power. At the beginning, the transmitted power decreased without a change in the spectrum. At an input power of around 100 mW, a sharp transition occurred, and the spectrum changed to a 1-FSR comb,

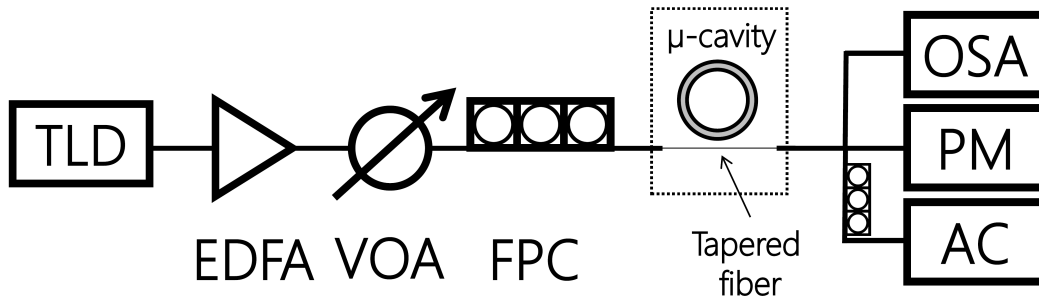


Fig. 3.8: Experimental setup for microcomb generation. TLD, tunable laser diode (Santec TSL-710); EDFA, erbium-doped fiber amplifier (Pritel PMFA-30); FPC, fiber polarization controller (Thorlabs FPC560); VOA, variable optical attenuator (OZ Optics DA-100); OSA, optical spectrum analyzer (Yokogawa AQ6375); PM, power meter (Agilent 8163B); AC, auto-correlator (APE Berlin pulseCheck).

as shown in Figure 3.11(f). This change is in accordance with calculated results. Therefore, a mode-locked microcomb generated by a silica toroid microcavity was achieved with the input power control method. The vibration of the transmitted power at an input power of around 90 mW was also observed. Although this might have been affected by optomechanics of the cavity, such an effect is beyond the scope of this study.

Finally, temporal waveform measurements of a microcomb are reported. An autocorrelation based on second-harmonic generation (SHG) was used for these measurements. Figure 3.12 shows the optical spectra and the SHG autocorrelation traces under different conditions. Since microcomb generation requires a high-power continuous-wave laser, the comb measured with an optical spectrum analyzer usually contains the high-power component caused by the input passing through the cavity. This phenomenon is often an obstacle to measurement of optical pulses, because it pushes the noise level too high. There are some proposed methods for eliminating the obstacle component. For example, it can be cut with a fiber Bragg grating or a wave shaper. With an add-drop setup, the comb measured in the drop port is not affected by the input.

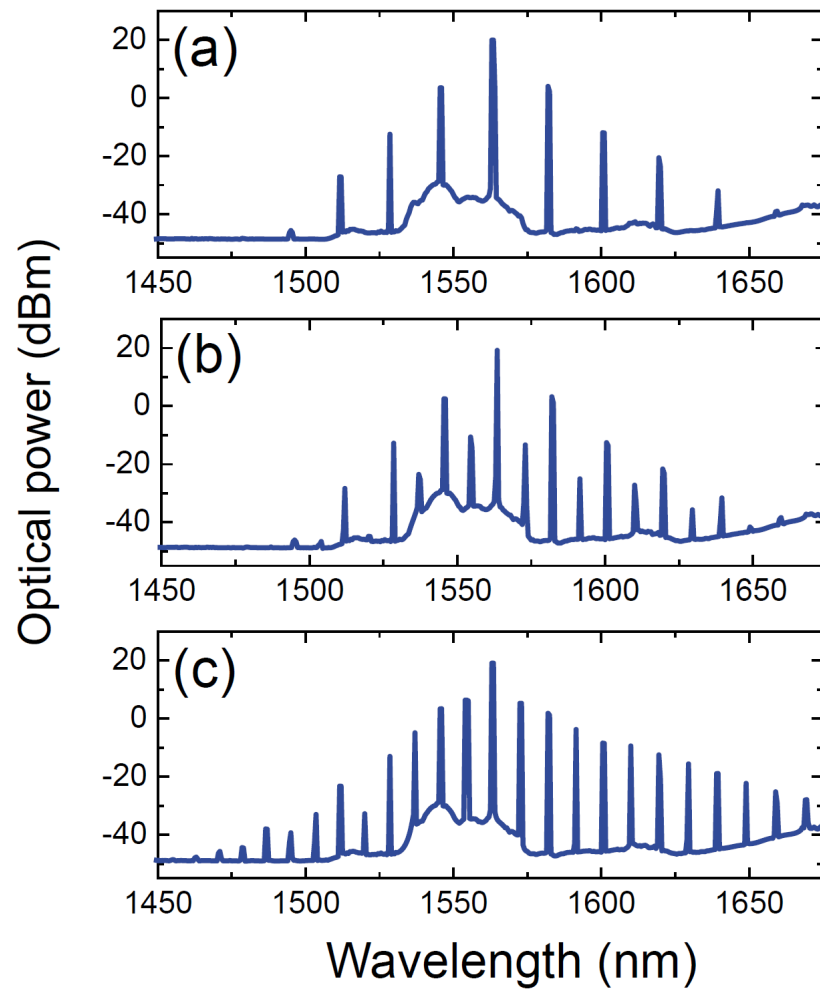


Fig. 3.9: Experimental output optical spectra when the cavity is pumped at (a) 433 mW, (b) 419 mW, and (c) 407 mW. The pumping power was gradually reduced during the experiment.

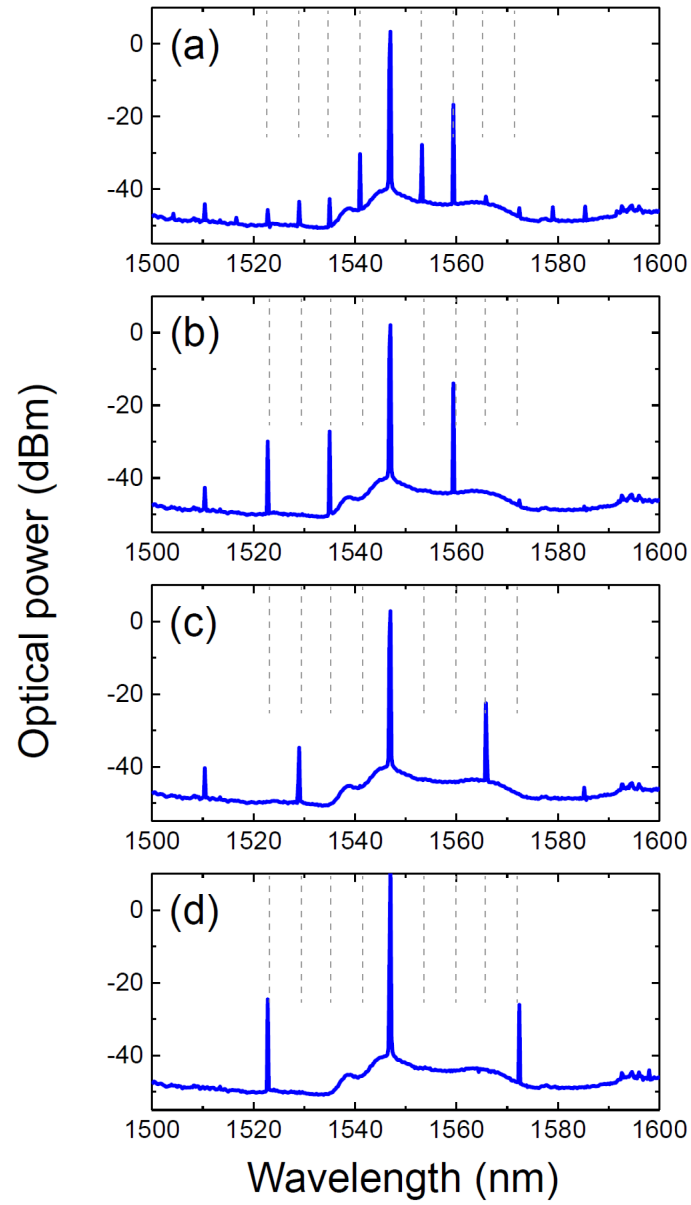


Fig. 3.10: Experimental output optical spectra when the gap is tuned at the points approaching with (a) 0 nm, (b) 50 nm, (c) 190 nm, (d) 240 nm.

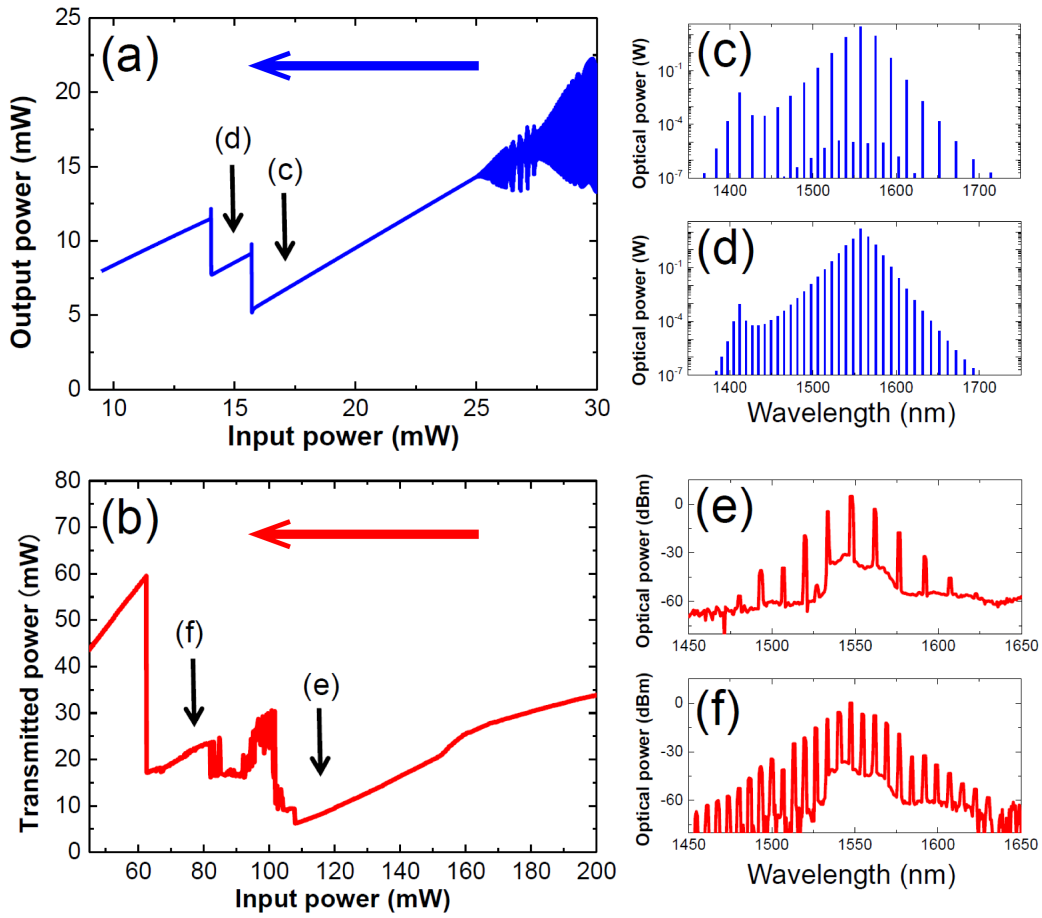


Fig. 3.11: (a) Calculated and (b) experimental transmitted powers as a function of input power. (c-f) show the output spectra at the corresponding input powers. Both show a case when the input power is decreased.

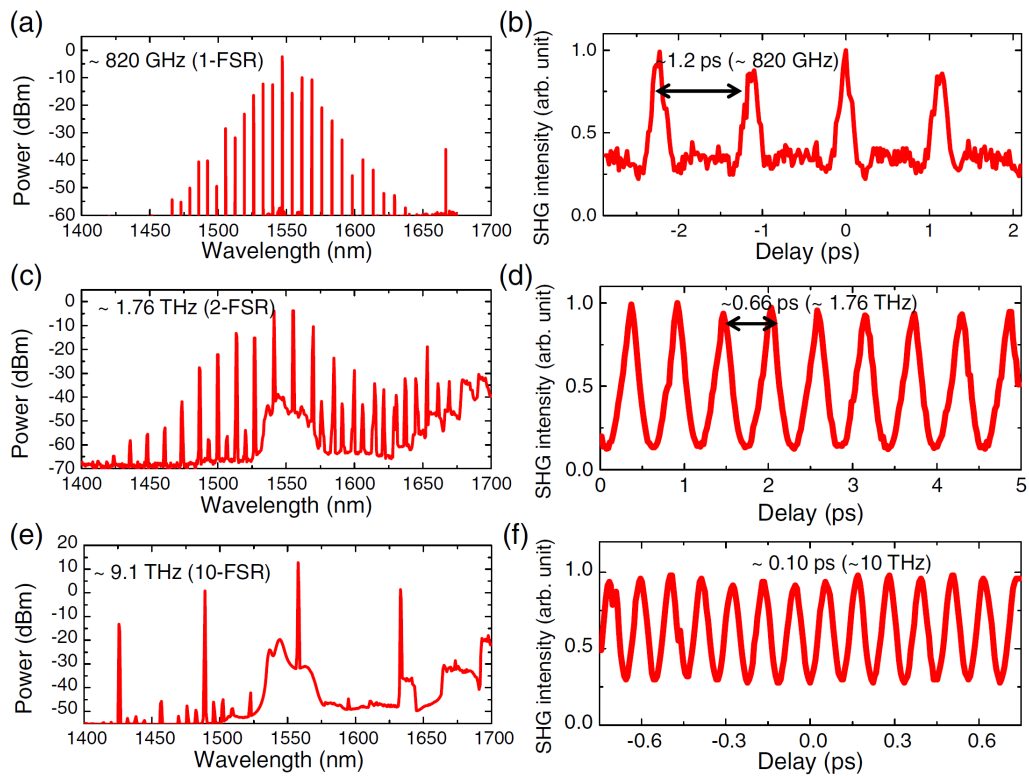


Fig. 3.12: (a) Spectrum of the Kerr comb generation at 1-FSR spacing. (b) SHG autocorrelation trace for the output shown in (a). (c, e) The same as (a) but with different input power and wavelength. (d, f) Corresponding SHG auto-correlation traces for (c) and (e).

3.5 Summary

In this chapter, descriptions of a Lugiato-Lefever equation were explained. The Lugiato-Lefever equation fits a model for analyzing microcomb generation. With a view towards use for calculations, dispersion parameters of a silica toroid microcavity were described. Based on the model, hysteresis behavior was analyzed in terms of microcomb generation. It was found that a mode-locked microcomb can be achieved with only an input power control. Numerical simulation for a silica toroid microcavity showed that a mode-locked microcomb can be obtained, and I also showed this experimentally. To my knowledge, this is the first time a soliton step indicating a mode-locked microcomb with a silica toroid microcavity has been observed.

Chapter 4

Influence of stimulated Raman scattering on microcomb generation in a silica cavity

This chapter describes the influence of stimulated Raman scattering on microcomb generation in a silica cavity. With a Lugiato-Lefever equation that includes a Raman effect, some differences from the simple model described in Chapter 3 are shown. Next, modulation instability gain is explained, which reveals that a large-FSR cavity behaves differently from a small-FSR cavity. Finally, a method to control four-wave mixing and stimulated Raman scattering is proposed.

Section 4.1 shows a mathematical description of a Raman effect and an extended model of a Lugiato-Lefever equation. Section 4.2 explains modulation instability gain in a cavity, which indicates that a large-FSR cavity behaves differently from a small-FSR cavity. Section 4.3 proves this numerically.

4.1 Raman scattering in silica

This section explains a numerical model that describes the behavior of a nonlinear cavity in which four-wave mixing and stimulated Raman scattering occur simultaneously.

The starting point is the nonlinear Schrödinger equation given by

$$\frac{\partial A}{\partial z} = -\frac{\alpha}{2}A - \frac{i}{2}\beta_2\frac{\partial^2 A}{\partial T^2} + i\gamma|A|^2A. \quad (4.1)$$

Considering a high-order nonlinear effect, the equation is described as⁵¹⁾

$$\frac{\partial A}{\partial z} = -\frac{\alpha}{2}A - \frac{i}{2}\beta_2\frac{\partial^2 A}{\partial T^2} + i\gamma\{A(z,t)\int_0^\infty R(t')|A(z,t-t')|^2 dt'\}, \quad (4.2)$$

where R is a nonlinear response function given by

$$R(t) = (1 - f_R)\delta(t) + f_R h_R, \quad (4.3)$$

where f_R represents the fractional contribution of the delayed Raman response. The Raman response function h_R in silica is shown in Figure 4.1. Thus, the first term and the second term on the right side of Equation 4.3 mean the Kerr response (immediate response) and the Raman response (delayed response), respectively.

With Equation 4.2, an expanded Lugiato-Lefever equation is derived as

$$t_R \frac{\partial E(n, \tau)}{\partial n} = \left(-\frac{\alpha L}{2} - \frac{T}{2} - i\delta - \frac{i}{2}\beta_2 L \frac{\partial^2}{\partial \tau^2} + N\right)E + \sqrt{T}E_{\text{in}}, \quad (4.4)$$

$$N = i\gamma L \left(\int_0^\infty \{(1 - f_R)\delta(t) + f_R h_R\} |E(n, t - t')|^2 dt' \right). \quad (4.5)$$

For silica, $f_R = 0.18$ is a common value. With this Lugiato-Lefever equation, calculated results are shown in Figure 4.2. Calculated parameters are: $Q_{\text{int}} =$

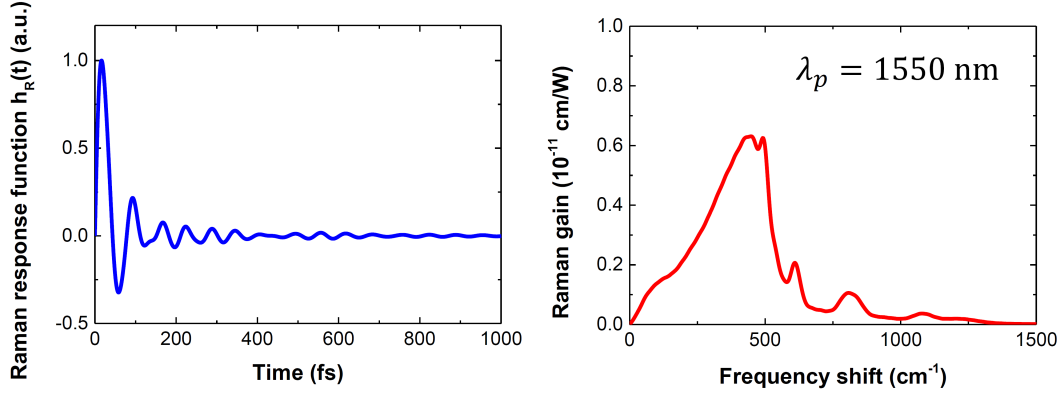


Fig. 4.1: Temporal variation of the Raman response function $h_R(t)$ in fused silica. And, Raman gain spectrum of silica fiber at a wavelength of 1550 nm.

1×10^7 , $Q_{\text{couple}} = 1 \times 10^7$, $\beta_2 = -4 \text{ ps}^2/\text{km}$, $\gamma = 5 \times 10^{-9} \text{ W}^{-1}\mu\text{m}^{-1}$, $f_{\text{FSR}} = 500 \text{ GHz}$, $L = 416 \mu\text{m}$, and calculated mode number $N = 256$.

Table. 4.1: The parameters for the calculation for Figures 4.2 (a) and (b).

Q_{int}	1×10^7	γ	$5 \times 10^{-9} \text{ W}^{-1}\mu\text{m}^{-1}$
Q_{couple}	1×10^7	f_{FSR}	500 GHz
β_2	$-4 \text{ ps}^2/\text{km}$	L	416 μm
input power	20 mW	N	256

Table. 4.2: The parameters for the calculation for Figures 4.2 (c) and (d).

Q_{int}	1×10^7	γ	$5 \times 10^{-9} \text{ W}^{-1}\mu\text{m}^{-1}$
Q_{couple}	1×10^7	f_{FSR}	500 GHz
β_2	$5 \text{ ps}^2/\text{km}$	L	416 μm
input power	20 mW	N	256

With an input power of 20 mW, a soliton state is shown in Figures 4.2(a) and (b). It is worth noting that the center of the microcomb is shifted to 1612 nm from a pump wavelength of 1550 nm. This is similar to the effect of intrapulse Raman scattering in an optical fiber. For a microcomb system, the amount of shift is described as¹³¹⁾

$$f_{\text{shift}} = -\frac{32\pi}{15} \left(\frac{\delta}{D_2} \right) f_R \left(\frac{2\pi\tau_R}{t_R} \right) D_1, \quad (4.6)$$

where δ is a cavity detuning term, and τ_R is a Raman shock term (with $\tau_R = 89$ fs for silica). Thus, the Raman shift depends on the FSR of the cavity, the cavity dispersion, and the cavity detuning. The behavior of the anomalous dispersion is clearly different from the normal dispersion. Figures 4.2(c) and (d) show a spectrum and a temporal wave with a normal dispersion of $\beta_2 = 5$ ps²/km, and others are the same as Figures 4.2(a) and (b), which that show stimulated Raman scattering is dominant. As explained later, there is hardly any four-wave mixing gain in the normal dispersion. These results show a gain competition between four-wave mixing and stimulated Raman scattering in the cavity.

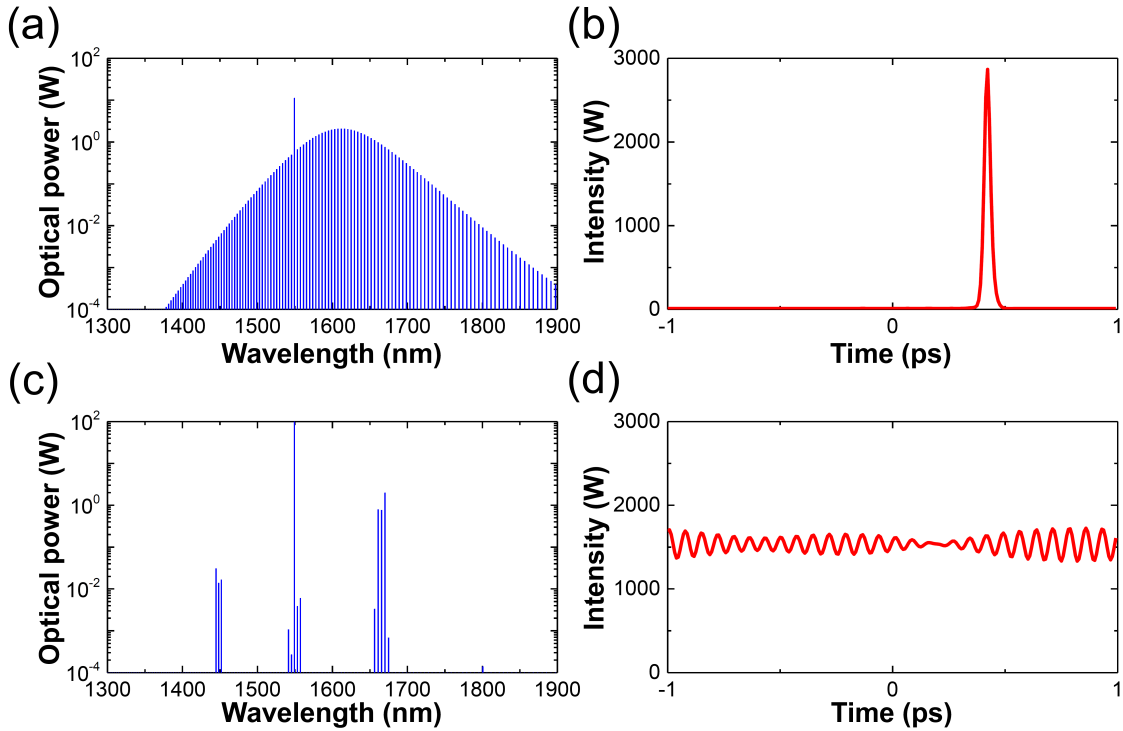


Fig. 4.2: (a) Typical cavity soliton state with the Raman effect. The center of the sech spectrum is shifted by the Raman effect. (b) Temporal waveform of (a). (c) Spectrum when stimulated Raman scattering is dominant. (d) Temporal waveform of (c).

4.2 Modulation instability gain

In this section, modulation instability gain in a cavity is explained. With some assumptions, it is found that a silica cavity with a large FSR behaves uniquely.

Modulation instability is a result of an interplay between the nonlinear and dispersive effects. It induces amplitude modulation of continuous wave input. It is also regarded as a degenerate four-wave mixing process and has been studied widely in fiber optics, a topic that applies to microcomb generation because it occurs from a continuous-wave input via degenerate four-wave mixing. A common gain equation for modulation instability is described as⁵¹⁾

$$g(\Omega) = |\beta_2 \Omega| \sqrt{\frac{4\gamma P_0}{|\beta_2|} - \Omega^2}, \quad (4.7)$$

where P_0 is the peak power of a pulse. Thus, the higher the value of P_0 , the higher the modulation instability gain, as shown in Figure 4.3(a). The process can be interpreted as four-wave mixing that requires phase matching derived from a balance between anomalous dispersion and self-phase modulation caused by P_0 . On the other hand, there is another phase term for the cavity, which is the cavity detuning δ_0 . Thus, Equation 4.7 is transformed into^{132, 133)}

$$g(\Omega) = \sqrt{(\gamma L P_0)^2 - (\delta_{\text{miss}})^2}, \quad (4.8)$$

$$\delta_{\text{miss}} = \delta_0 - \frac{\beta_2 L}{2} \Omega^2 - 2\gamma L P_0, \quad (4.9)$$

where g is the modulation instability gain per roundtrip of the cavity. As shown in Figure 4.3(b), the gain is shifted to follow the increase in input power due to a balance of three phase terms. Significantly, the gain near the pump disappears when the pump power increases because the solution of the gain in Equation 4.8 becomes imaginary. In other words, the input power influences the effective cavity detuning, which causes fluctuations in the phase-mismatching term. When the term δ_{miss} is zero, the gain is at its maximum. The frequency of the maximum gain is given by

$$\Omega_{\max}^2 = \frac{2}{L\beta_2}(\delta_0 - 2\gamma LP_0). \quad (4.10)$$

Considering resonant frequencies in the cavity, a unique behavior should occur in a silica cavity. A schematic image of this behavior is shown in Figure 4.4. First, when an input power is small, the gain covers a set of resonant frequencies at 1-FSR. Since the gain of four-wave mixing is ideally higher than that of Raman gain, four-wave mixing is dominant. The higher the input power, the farther the gain is shifted. Thus, when the gain is located between two resonant frequencies, the frequencies hardly experience the four-wave mixing gain and Raman scattering becomes dominant. Then, a further high input power causes the gain, which is dominant, to meet the next resonant frequency critically. This mechanism of gain is a novel finding, although a number of studies on competition between four-wave mixing and stimulated Raman scattering in the context of values of maximum gain have been conducted. However, previous studies focused on the comparison of maximum gains of four-wave mixing and stimulated Raman scattering, which neglects the case that resonant frequencies cannot experience the maximum gain^{3,5,134}). This transition requires a large-FSR silica cavity unless the four-wave mixing gain always covers one or multiple resonant frequencies.

4.3 Numerical simulation

To prove the theoretical considerations, a numerical simulation is used. Some of the numerical results are in close agreement with the theoretical analysis.

The calculated parameters are: $Q_{\text{int}} = 5 \times 10^7$, $\gamma = 3.686 \times 10^{-8} \text{ W}^{-1} \mu \text{ m}^{-1}$, $f_{\text{FSR}} = 1100 \text{ GHz}$. The silica toroid microcavity has a major diameter of $60 \mu \text{ m}$ and a minor diameter of $4 \mu \text{ m}$. To compare the gains of four-wave mixing and stimulated Raman scattering, the Raman gain is set as

$$g_{\text{Raman}} = g_{\text{bulk}}^R \frac{P_0}{A_{\text{eff}}} L_{\text{eff}} - \text{loss}, \quad (4.11)$$

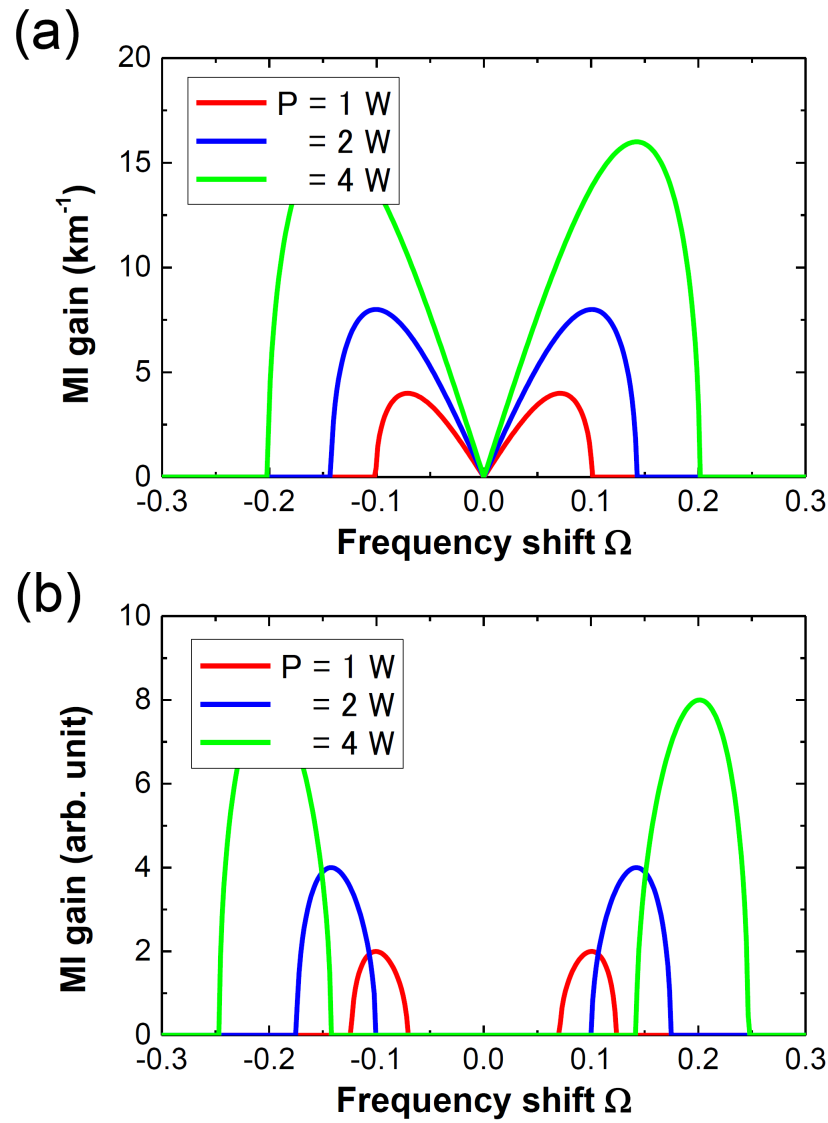


Fig. 4.3: Typical gain spectra of modulation instability at three power levels for (a) an optical fiber and (b) an optical cavity.

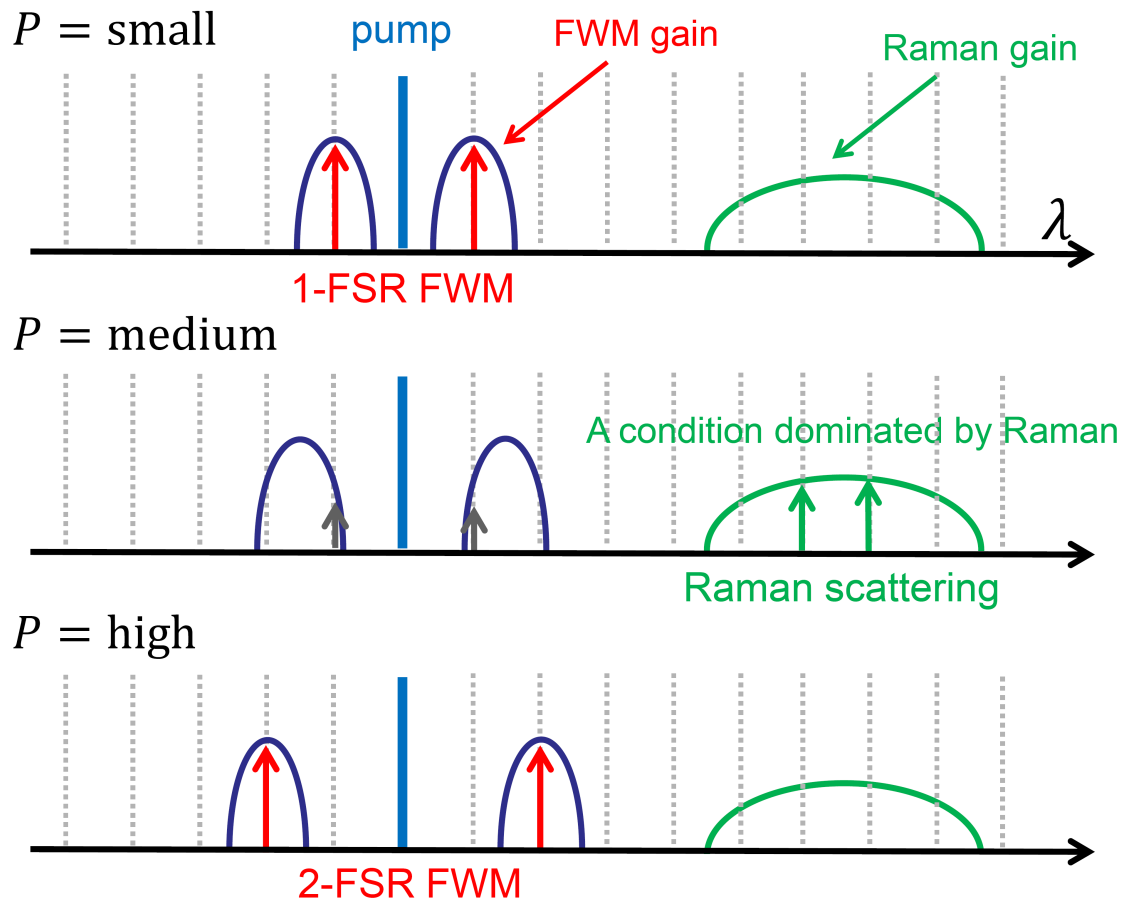


Fig. 4.4: Schematic image of the transition caused by gain competition between four-wave mixing and stimulated Raman scattering. When an input power is small, the first mode from the pump can experience a large gain of four-wave mixing. However, the increased input power shifts the four-wave mixing gain far from the pump, which causes the gain experienced by the resonant frequencies to be small. Thus, stimulated Raman scattering is dominant. When the input power is high, the four-wave mixing gain meets the resonant frequency again, which causes a 2-FSR comb.

$$L_{\text{eff}} = \frac{1}{\alpha_{\text{total}}} \{1 - \exp(-\alpha_{\text{total}}L)\}, \quad (4.12)$$

where $g_{\text{bulk}}^R = 0.631 \times 10^{-11}$, and $A_{\text{eff}} = 3 \mu\text{m}^2$. The variables α_{total} and L correspond to the Q and the FSR, respectively.

Table. 4.3: The parameters for the calculation for Figures 4.5 (a) and (b).

Q_{int}	5×10^7	γ	$3.686 \times 10^{-8} \text{ W}^{-1} \mu\text{m}^{-1}$
Q_{couple} in (a)	1×10^8	f_{FSR}	1100 GHz
Major radius	30 μm	detuning	0.01
Minor radius	2 μm	input power in (b)	10mW

The relationship between the intracavity power and the input power is required for an estimation of P_0 . It is described as

$$TP_{\text{input}} = (\gamma L)^2 P_0^3 - 2\delta_0 \gamma L P_0^2 + (\delta_0^2 + \alpha_{\text{total}}^2) P_0. \quad (4.13)$$

Using Equations 4.8, 4.11, and 4.13, the competition between four-wave mixing and stimulated Raman scattering is analyzed. Figure 4.5(a) shows each gain with a coupling Q of 100 million. The four-wave mixing gain is divided into each resonant frequency, i.e. the first mode and the second mode from the pump. The Raman gain is assumed to be homogenous and always at its maximum because the gain covers over 10 THz, which is much larger than the FSR. When the input power is between 9 and 20 mW, the four-wave mixing gain disappears, because the gain is located in a valley between the first and second modes, whereas the Raman scattering is dominant even if the maximum gain of the four-wave mixing is higher than that of the Raman scattering. Conventional analysis has been suggested in the context of maximum gain. Thus, this mechanism is novel because consideration of the FSR is a key point. Figure 4.5(b) indicates the gains with a fixed input when the coupling Q is changed. There is also a valley where the four-wave mixing gain disappears. A coupling Q works for changing the intracavity power when the input power is changed directly.

Figure 4.6 exhibits numerical simulation results with a Lugiato-Lefever model.

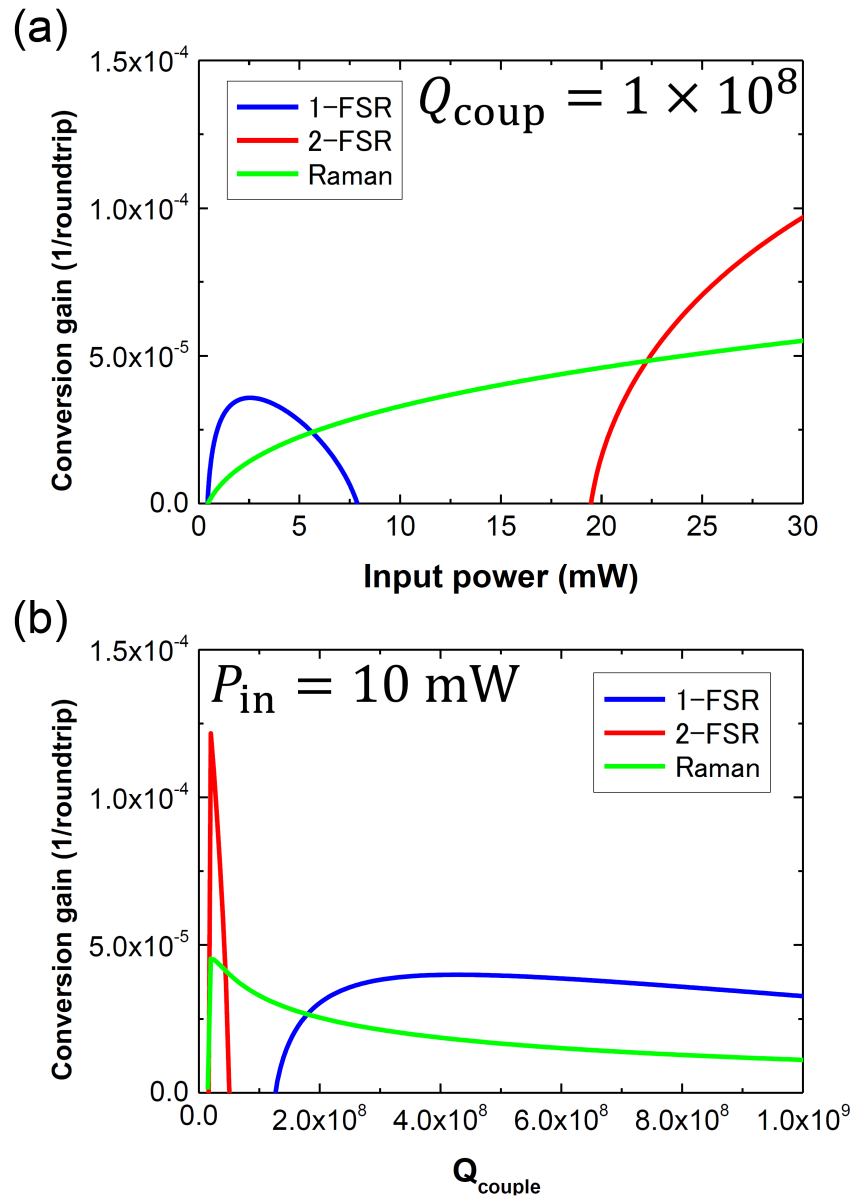


Fig. 4.5: (a) Gain of four-wave mixing for each resonant frequency and stimulated Raman scattering with respect to input power. (b) Same as (a) but with respect to coupling Q . The calculated parameters are a major diameter of $60 \mu\text{m}$, a minor diameter of $4 \mu\text{m}$, a cavity detuning of 0.01, and an FSR of 1100 GHz.

The parameters are same as those used in Figure 4.6 (b). First, a 2-FSR comb is obtained with a coupling Q of 3.0×10^7 , which is reasonable because the gain of the second mode from the pump is much higher than the Raman gain. Next, the coupling Q is set as 1×10^8 , where there is a valley in the four-wave mixing gain. Here, stimulated Raman scattering is dominant. Then, a coupling Q of 9×10^8 causes a 1-FSR comb. Thus, numerical simulation confirms the novel mechanism of gain competition between four-wave mixing and simulated Raman scattering in a large-FSR silica cavity.

Finally, an experimental result is shown in Figure 4.7. First, a 4-FSR comb and some Raman oscillations were obtained under certain conditions. After that, the input wavelength was slightly detuned to the red, causing the four-wave mixing lines to disappear and only the Raman oscillations to exist. With a little more red detuning, a 3-FSR comb was obtained. Although Raman oscillations always exist, the transition shown in the three panels indicates that the four-wave mixing gain is clearly influenced by the width of the free spectral range

4.4 Summary

The influence of stimulated Raman scattering on microcomb generation was described in this chapter. An extended model of a Lugiato-Lefever model that includes a Raman effect was developed, and typical results in the anomalous and normal dispersion regimes were discussed. Modulation instability gain in a cavity was explained theoretically. From the analysis, a novel mechanism of gain competition between four-wave mixing and simulated Raman scattering in a large-FSR silica cavity was suggested and then verified by numerical simulation and experiments. This discussion contributes to ideas on how to operate a large-FSR silica cavity such as a silica toroid microcavity.

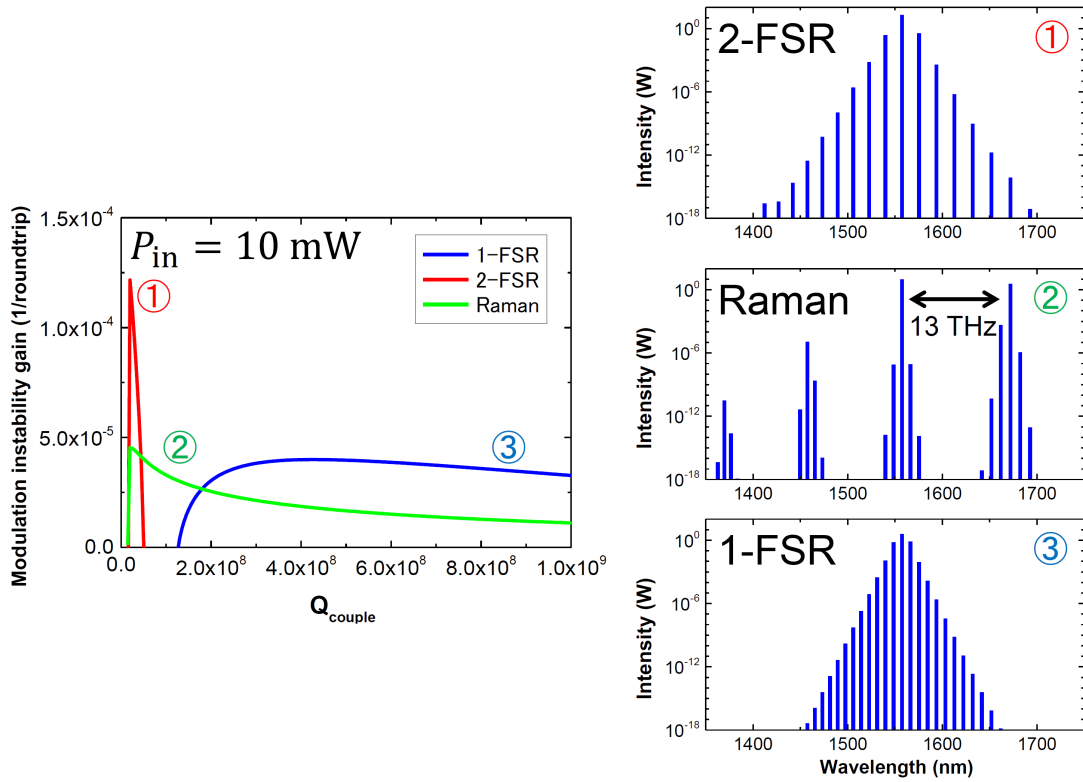


Fig. 4.6: Transition of comb spectra caused by gain competition between four-wave mixing and stimulated Raman scattering. 1.) A 2-FSR comb is obtained with a coupling Q of 3.0×10^7 . 2.) A Raman comb is dominant with a coupling Q of 1.0×10^8 . 3.) A 2-FSR comb appears with a coupling Q of 9.0×10^8 . The calculated parameters are a major diameter of $60 \mu\text{m}$, a minor diameter of $4 \mu\text{m}$, a cavity detuning of 0.01, and an FSR of 1100 GHz.

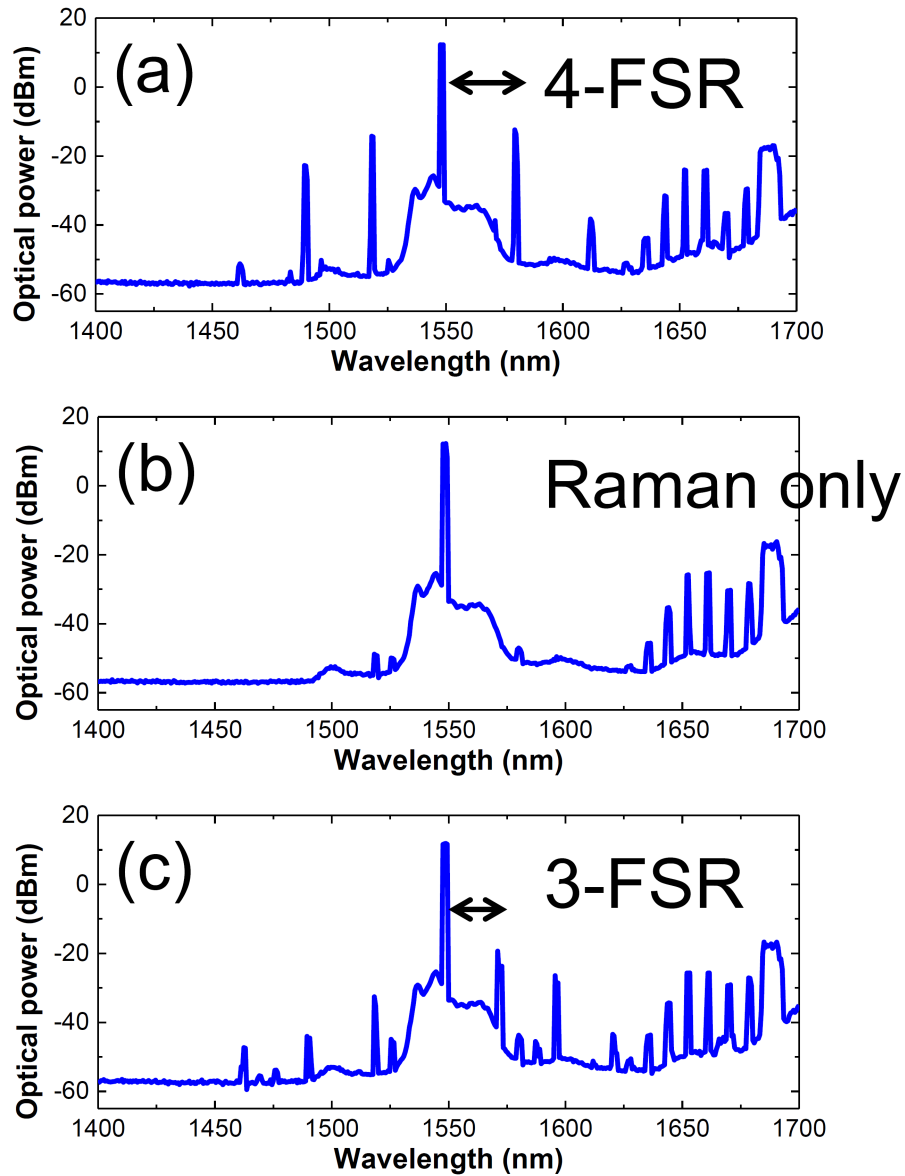


Fig. 4.7: Experimental results of transition of comb spectra caused by a valley in the four-wave mixing gain. (a) A 4-FSR comb and multiple Raman oscillations appear under certain conditions. (b) With a small amount of red detuning of the input wavelength, four-wave mixing lines disappear and Raman lines appear. (c) With a little more red detuning, a 3-FSR comb emerges.

Chapter 5

Transverse mode interaction via stimulated Raman scattering combs in a silica toroid microcavity

This chapter describes transverse mode interaction via stimulated Raman scattering in a silica toroid microcavity. Since every material has a Raman gain of a certain width, there are usually several transverse modes apart from the desired mode. In particular, silica has a broad Raman gain covering a width of 260 cm^{-1} , which corresponds to approximately 100 nm around 1550 nm. Although transverse mode interaction via stimulated Raman scattering seems to occur frequently, it can be suppressed by the selection of a pump mode. The relationship between the quality factor of a pump mode and a Raman mode determines the strength of the mode interaction.

Section 5.1 describes stimulated Raman scattering in a silica toroid microcavity. With a theoretical analysis, the possibility of the mode interaction via stimulated Raman scattering is discussed. Section 5.2 shows experimental results verifying that transverse mode interaction occurs in the cavity. It is found that the control of the mode interac-

tion can be performed with a selection of a pump modes. Section 5.3 explains numerical simulation results with coupled Lugiato-Lefever equation. Calculated results are in close agreement with the theoretical analysis and the experimental results.

5.1 Stimulated Raman scattering

Since the Raman effect is based on molecular vibration, it is a universal effect in optics. It is derived from third-order nonlinearity, so that the threshold of Raman lasings is essentially high. Here, a high- Q microcavity that enhances optical power inside is an appropriate platform for demonstrating applications with the Raman effect. In high- Q silica cavities, it is easy to utilize Raman lasing because the Raman gain covers a width of 260 cm^{-1} , which corresponds to approximately 100 nm around 1550 nm. Thus, precise control of resonant frequencies is not required to match the gain and the resonant frequency because a broad width of the gain contains one or multiple resonant frequencies by accident. In 2002, Raman lasing in a high- Q cavity was demonstrated with a silica microsphere⁷⁾. Since then, a number of studies have been conducted. The threshold power of stimulated Raman scattering is described as⁵⁾

$$P_{\text{th}} = \frac{\pi^2 n^2 V}{\lambda_p \lambda_R g_R} \left(\frac{1}{Q_{\text{int}} \right)_P \left(\frac{1}{Q_{\text{int}} \right)_R \cdot \frac{(1 + K_R)(1 + K_P)^2}{K_P}, \quad (5.1)$$

where λ_p and λ_R are the respective wavelengths of the pump and a Raman mode, g_R is the nonlinear bulk Raman gain coefficient, V is the effective mode volume, and Q_{int} is the intrinsic Q factor, in which the subscript means a pump mode (P) and a Raman mode (R). K is a coupling factor and defined as $K = Q_{\text{int}}/Q_{\text{coup}}$. Thus, if the mode is at critical coupling, K should be 1. Given that the values of Q s of two modes are the same, and both modes are at critical coupling, the equation is simplified to

$$P_{\text{th}} = \frac{\pi^2 n^2 V}{\lambda_p \lambda_R g_R} \left(\frac{1}{Q_{\text{int}}} \right)^2 \cdot 8. \quad (5.2)$$

Note that the minimum threshold is obtained when $K = 1/2$, which means an undercoupling condition.

$$P_{\text{th}}^{\text{min}} = \frac{\pi^2 n^2 V}{\lambda_p \lambda_R g_R} \left(\frac{1}{Q_{\text{int}}} \right)^2 \cdot \frac{27}{4}. \quad (5.3)$$

Here, transverse mode interaction is considered. In other words, a situation in which a pump mode excites a Raman oscillation in a different mode family is dis-

cussed. Transverse mode interaction via stimulated Raman scattering is often observed experimentally unlike via four-wave mixing. Although there is a report on transverse mode interaction via four-wave mixing⁷³⁾, it requires complex design of the dispersions of three mode families (pump, signal, and idler modes). Thus, the only path of stimulated Raman scattering is considered in this section.

Nonlinear effective mode volume, which expresses a mode overlap, is given by

$$V = \frac{\int |E_P|^2 dV \int |E_R|^2 dV}{\int |E_P|^2 |E_R|^2 dV}, \quad (5.4)$$

Three mode families (TE₀₀, TE₀₁, and TE₁₀) in a silica toroid microcavity with a major diameter of 100 μm and a minor diameter of 8 μm are considered. The spatial mode profiles of the modes are calculated with an FEM as shown in Figure 5.1. Since the relationship that $V = 2\pi r A_{\text{eff}}$, where r is a radius, is reasonable, an effective mode area A_{eff} is used from now on. Effective mode areas of each combination are evaluated as shown in Table 5.1, where the value of the combination of one mode with itself corresponds to the value of the common effective mode area.

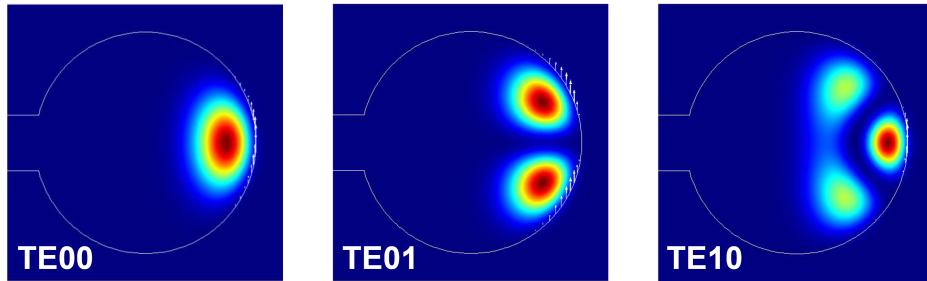


Fig. 5.1: Cross-sectional mode profiles of a silica toroid microcavity. These results were obtained using the finite-element method (COMSOL Multiphysics). The diameter of the microcavity is 100 μm and the minor diameter is 8 μm. The results are for the TE₀₀, TE₀₁, and TE₁₀ mode.

Table. 5.1: Effective mode area considering mode interaction.

$A_{\text{eff}} [\mu\text{m}^2]$	TE ₀₀	TE ₀₁	TE ₁₀
TE ₀₀	9.7549	18.1876	21.6853
TE ₀₁	18.1876	12.7816	29.4491
TE ₁₀	21.6853	29.4491	17.7464

To compare the threshold power of the excitation of a different mode family

via the SRS process, I define the power ratio C as

$$C = \frac{P_{\text{th-same}}}{P_{\text{th-diff}}} = \frac{A_{\text{same}}}{A_{\text{diff}}} \cdot \frac{Q_{\text{diff}}^t}{Q_{\text{same}}^t}, \quad (5.5)$$

where, Q_{same}^t and Q_{diff}^t are total Q s of the same mode as a pump mode and the different mode, respectively. The ratio expresses which modes have a low threshold power from a pump mode. In essence, since the mode overlap is small (A_{diff} is considerably larger), the C is less than 1, which means a mode interaction will not occur, because the threshold power for exciting the same mode via stimulated Raman scattering is lower. However, even if a mode overlap is not perfect, a relationship between Q s can compensate for it. Figure 5.2 shows the function C with different Q s. In a silica toroid microcavity, since a lower-order mode has higher Q , I assume only three transitions of $\text{TE}_{01} \rightarrow \text{TE}_{00}$, $\text{TE}_{10} \rightarrow \text{TE}_{00}$, and $\text{TE}_{01} \rightarrow \text{TE}_{10}$. Note that the value of C is always below 1 when both Q s are the same ($Q_{\text{diff}}^t/Q_{\text{same}}^t = 1$), because mode overlapping must be imperfect. When C is greater than 1, the threshold power of excitation of the different mode family is lower, which indicates the a mode interaction should occur. It is found that the ratio of $Q_{\text{diff}}^t/Q_{\text{same}}^t$ of only 1.5 causes a mode interaction that is dominant with respect to the threshold power. The analytical results reveal that high-order mode pumping easily causes a mode interaction via stimulated Raman scattering.

5.2 Experimental results

In this section, experimental results on stimulated Raman scattering in a silica toroid microcavity are shown. In particular, a mode interaction is focused on, in order to confirm the theory discussed above.

Figure 5.3(a) shows the experimental setup. A tunable laser diode scans the input laser wavelength, and an erbium-doped fiber amplifier amplifies the input power up to 1 W. A tapered fiber with a diameter of about 1 μm is used as an evanescent coupler. The output is measured with a power meter and an optical spectrum analyzer. Figure 5.3(b) shows a microscope image obtained from the top of a fabricated cavity. A typical Raman gain for silica is shown in Figure 5.3(c).

First, I pumped one of the modes and observed the spectrum, as shown in Fig-

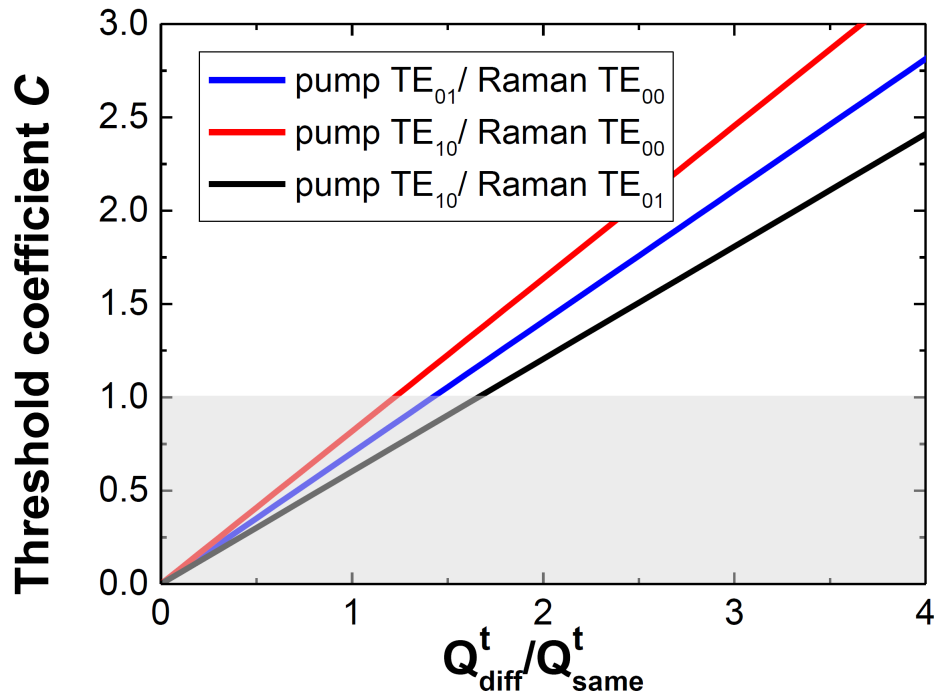


Fig. 5.2: Calculated threshold coefficient C . The blue, red, and black lines indicate combinations of TE_{01} (pump) - TE_{00} (Raman), TE_{10} (pump) - TE_{00} (Raman), and TE_{10} (pump) - TE_{01} (Raman), respectively. That the coefficient C is greater than 1 means that the threshold of excitation for a different mode family is lower than that for the same mode family, indicating that a mode interaction should occur.

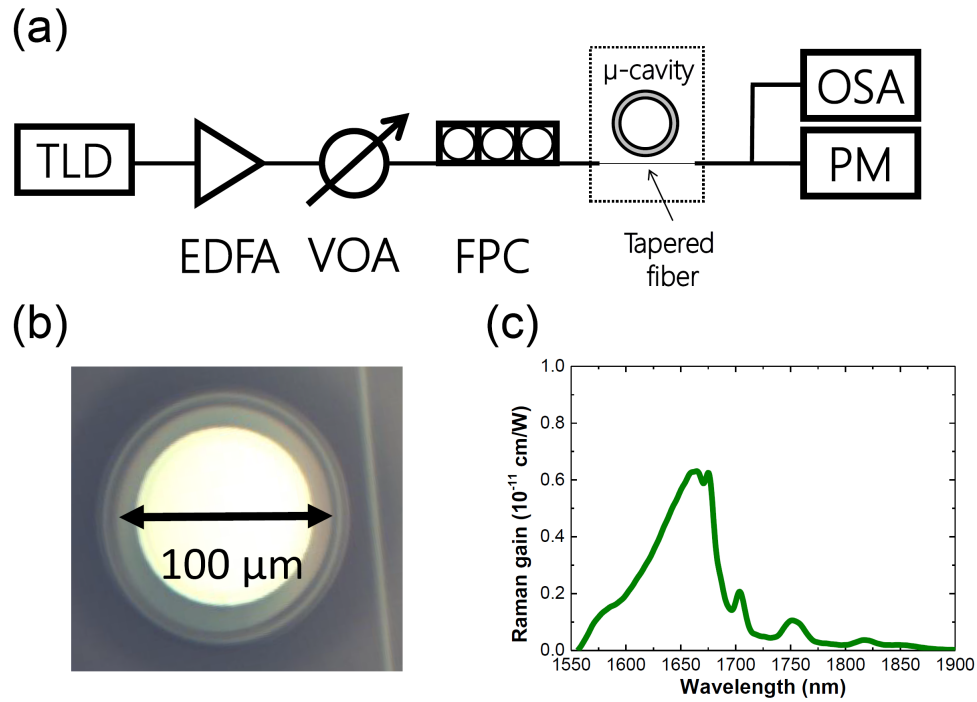


Fig. 5.3: (a) Schematic image of our experimental setup. TLD, tunable laser diode (Santec TSL-710); EDFA, erbium-doped fiber amplifier (Pritel PMFA-30); VOA, variable optical attenuator (OZ Optics DA-100); FPC, fiber polarization controller (Thorlabs FPC560); OSA, optical spectrum analyzer (Yokogawa AQ6375); PM, power meter (Agilent 81634B). A tapered fiber is used as an evanescent coupler to couple light with the microcavity. (b) An optical microscope image showing the top view of a fabricated silica toroidal microcavity. A tapered fiber is aligned close to the cavity. The diameter is about $100 \mu\text{m}$. (c) Typical Raman gain for silica at 1550 nm ^{135, 136}.

ure 5.4(a). A comb spectrum ranging from 1400–2000 nm was observed. Figure 5.4(c) is a magnified view of Figure 5.4(a), which shows that the stimulated Raman scattering occurred in the same mode family as the pump mode. Next, I pumped a different mode. The result, where I observed a dual-comb-like spectrum, is shown in Figure 5.4(b). The magnified view shown in Figure 5.4(d) clearly shows that a different mode family is excited via the stimulated Raman scattering process. Note that the transverse mode is not generated through FWM because of the energy and momentum mismatch. The frequency difference between these two mode families is about 180 GHz.

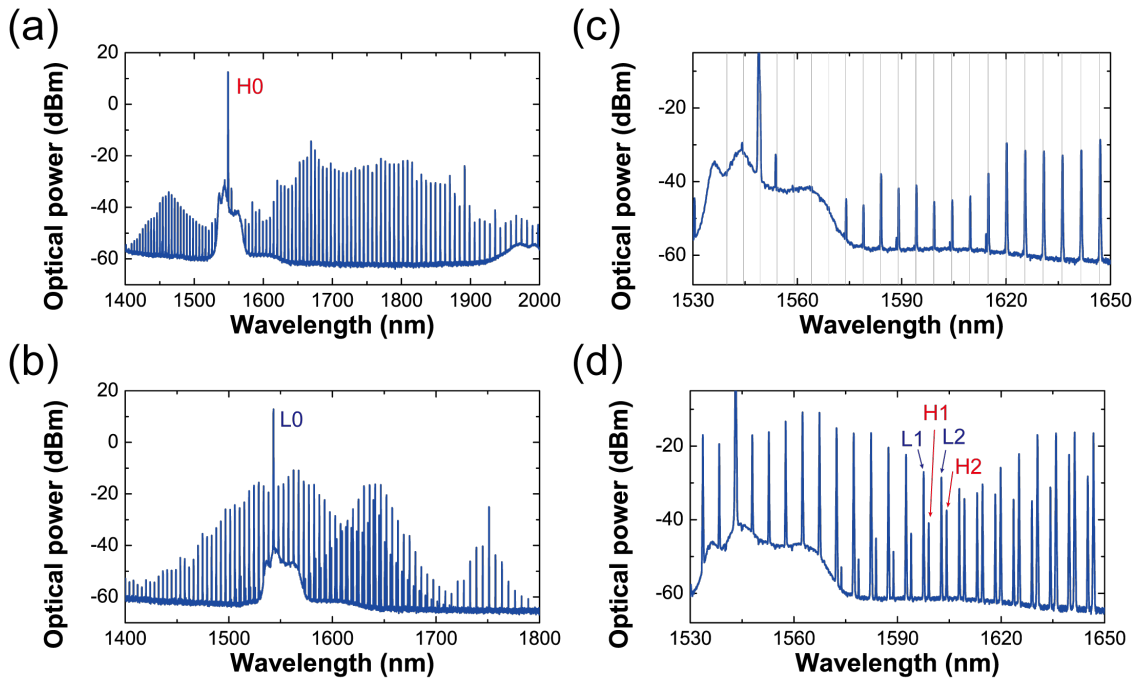


Fig. 5.4: Optical spectra pumped with different modes. Same cavity was used for all. Graphs show the spectrum when the pump wavelength was (a) 1548.96 nm and (b) 1543.08 nm. The pump power was about 1 W after the EDFA. (c) and (d) are magnified views of (a) and (b), respectively. The equidistant vertical gray lines in (c) show that the SRS comb was generated in the same mode family as the pump mode.

Next, I measured the Q s of the pump and the stimulated Raman scattering comb modes. The measured modes are indicated in Figure 5.4 as H0 and L0 for two different pump modes and L1, L2, H1, and H2 as two different sets of mode families. I performed a conventional transmittance spectrum measurement us-

ing a tunable wavelength sweep laser, and I obtained Q s of 1.1×10^7 for the 1548.96 – nm mode (H0 mode) and 3.1×10^6 for the 1543.08 – nm mode (L0 mode), as shown in Figures 5.5(a) and (b), respectively. It should be noted that the resonant wavelengths were shorter than those in Figure 5.4 due to the presence of the thermo-optic effect. Figures 5.6(a) and (b) are the transmittance spectra for the H1 and H2 modes, which exhibited Q s of 1.6×10^7 and 1.9×10^7 , respectively. On the other hand, the Q s for the L1 and L2 modes were only 5.2×10^6 and 4.7×10^6 , respectively. From this result, I confirmed that an energy transfer occurred when I pumped in a low- Q mode, but no transverse mode coupling occurred when I pumped the cavity in the highest- Q mode. Therefore, to suppress the generation of a different longitudinal mode family, one must pump the cavity at the highest- Q mode. This transverse mode coupling even allows one to find the lowest order mode, because the lowest order mode ultimately has the highest Q in the cavity. This experimental result is in close agreement with our theoretical understanding that stimulated Raman scattering converts energy from a low- Q mode to a high- Q mode.

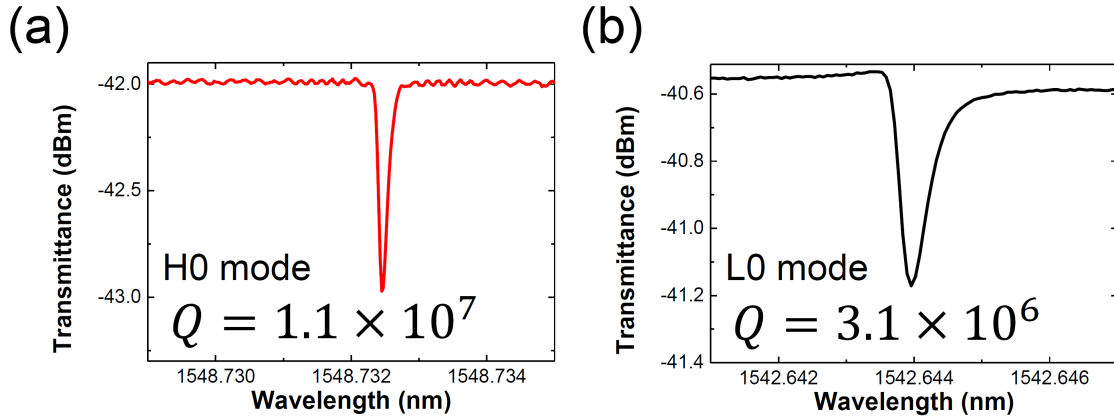


Fig. 5.5: (a) Transmittance spectrum for the 1548.96 nm mode used in Figs. 5.4(a). (b) Same as (a) but for 1543.08 nm. It should be noted that the resonant is at shorter wavelength for Figs. 5.4(a) and (b) due to the presence of the thermo-optic effect, but we are measuring the same mode.

Figure 5.7 confirms our ideas by showing pumping performed at different wavelengths. Figure 5.7(a) explains the high- and low- Q values of the pump modes. The spectra obtained when I pumped at H0 and L0 are already shown in Figures 5.4(a) and (b). When I compared Figures 5.7(c) and 5.4(a), which shows

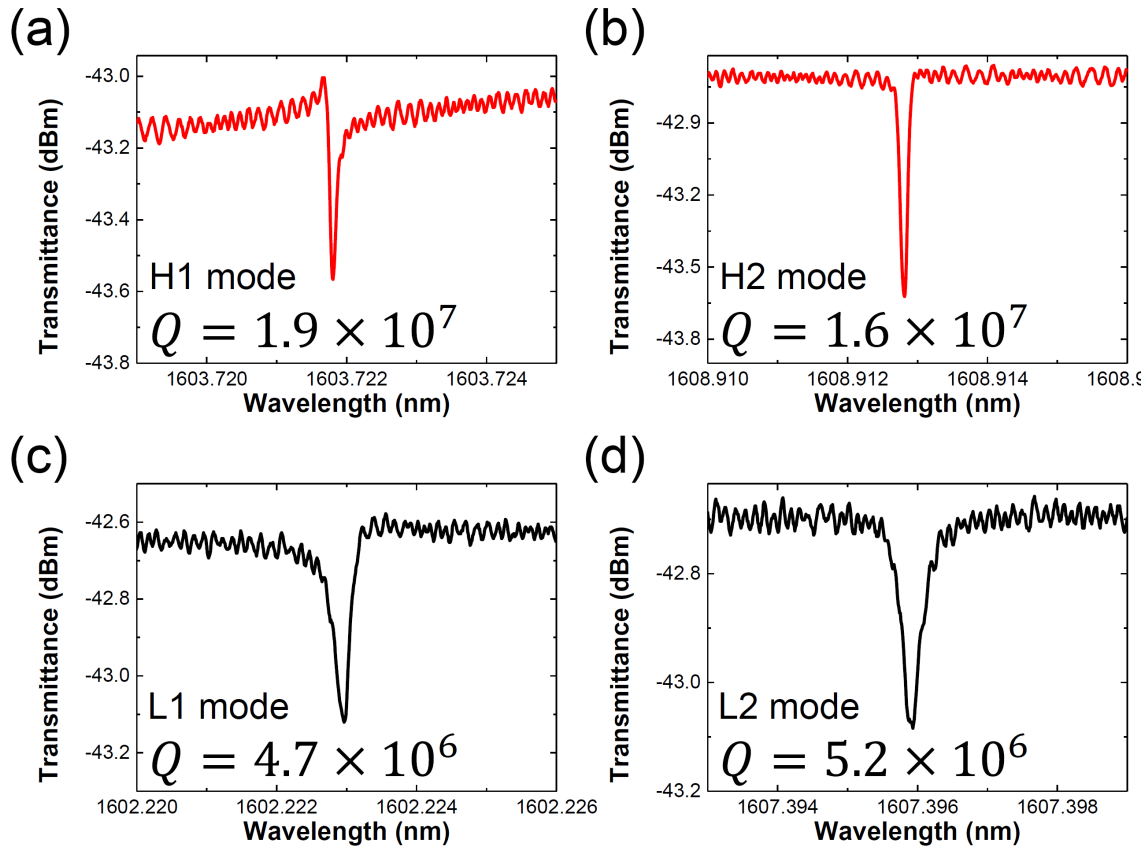


Fig. 5.6: Transmittance spectra of the modes where combs were generated: (a) H1, (b) H2, (c) L1, and (d) L2 modes. The obtained Q s are shown in the panels.

the spectrum when I pumped at mode (c), I found that they were almost identical, showing only one longitudinal mode family. This indicates that the stimulated Raman scattering process occurred in the same mode family as the pump. Indeed, I confirmed that the anti-Stokes light is also in the same mode family. On the other hand, Figure 5.7(b), when I pumped at mode (b), had the same trend as Figure 5.4(b), which shows a twin comb spectrum. Figure 5.7(b) shows that anti-Stokes stimulated Raman scattering light is excited at 1450 nm, and it is also in a different mode family from the pump but in the same mode family as the stimulated Raman scattering mode. Thus, the generation of the high- Q mode family dominates the generation of the low- Q mode in the stimulated Raman scattering process. These results indicate that mode interaction behavior depends solely on the relationship between the Q s of the modes used for the pump and the generated stimulated Raman scattering light.

5.3 Numerical simulation with a coupled Lugiato-Lefever equation

In this section, a numerical model is explained that describes the behavior of a nonlinear cavity in which four-wave mixing and stimulated Raman scattering occur simultaneously. With a developed numerical model, I confirm experimental results and theoretical analyses.

To obtain a full understanding of the behavior of a nonlinear cavity, I modified the Lugiato-Lefever equation and took the nonlinear energy transition via stimulated Raman scattering into account. The equations¹³⁷⁾ are as follows:

$$\begin{aligned}
 t_R \frac{\partial E_p}{\partial r} = & \left(-\frac{\alpha_p}{2} - \frac{\kappa_p}{2} - i\delta_p + iL \sum_{k \geq 2} \frac{\beta_p^{(k)}}{k!} \left(-i \frac{\partial}{\partial \tau} \right)^k + iL(1-f_R)(\gamma_p |E_p|^2 + 2\gamma_p |E_s|^2) E_p + f_R \left\{ \gamma_p E_p \int_{-\infty}^{\infty} h_R(t') \right. \right. \\
 & \left. \left. |E_p(t-t')|^2 dt' + \Gamma_p E_p \int_{-\infty}^{\infty} h_R(t') |E_s(t-t')|^2 dt' + \Gamma_p E_s \int_{-\infty}^{\infty} h_R(t') E_p(t-t') E_s^*(t-t') dt' \right\} + \sqrt{\kappa} E_{in}, \quad (5.6)
 \end{aligned}$$

$$\begin{aligned}
 t_R \frac{\partial E_s}{\partial r} = & \left(-\frac{\alpha_p}{2} - \frac{\kappa_p}{2} - iL(\beta_s^{(1)} - \beta_p^{(1)}) \left(-i \frac{\partial}{\partial \tau} \right) + iL \sum_{k \geq 2} \frac{\beta_s^{(k)}}{k!} \left(-i \frac{\partial}{\partial \tau} \right)^k + iL(1-f_R)(\gamma_s |E_s|^2 + 2\gamma_s |E_p|^2) E_s + f_R \right. \\
 & \left. \left\{ \gamma_s E_s \int_{-\infty}^{\infty} h_R(t') |E_s(t-t')|^2 dt' + \Gamma_s E_s \int_{-\infty}^{\infty} h_R(t') |E_p(t-t')|^2 dt' + \Gamma_s E_p \int_{-\infty}^{\infty} h_R(t') E_s(t-t') E_p^*(t-t') dt' \right\}, \quad (5.7)
 \end{aligned}$$

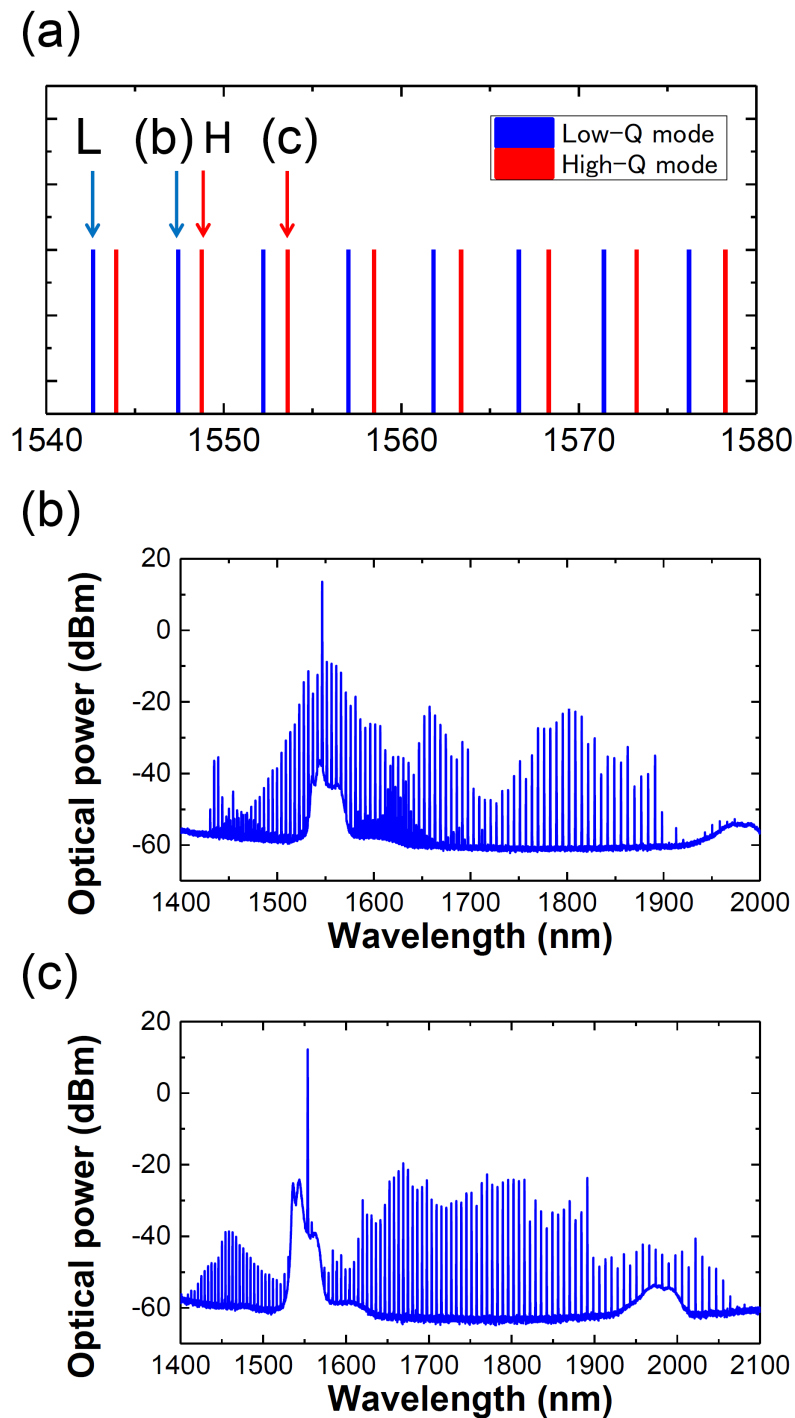


Fig. 5.7: (a) Explanation of the high and low Q modes of the pump in the experimental cavity. (b) Optical spectrum when we pump at mode b. (c) Same as (b) but when we pump the cavity at mode c.

where E_p and E_s are the electrical fields of the pump and signal (Raman) light. The variables r , t , t_R , L , and E_{in} are the propagation coordinate (step), (short) time, round-trip time, cavity length, and pump light, respectively. The variables α , κ , δ , $\beta^{(k)}$, γ , and Γ are the intrinsic cavity loss, coupling loss with the waveguide, detuning of the frequency from the resonance (detuning from the center frequency), cavity dispersion, effective nonlinear coefficients, and effective nonlinear coefficients considering mode overlapping, respectively. The subscripts denote pump and signal light. Cavity dispersion is calculated with a finite-element method as shown in Figure 5.8.

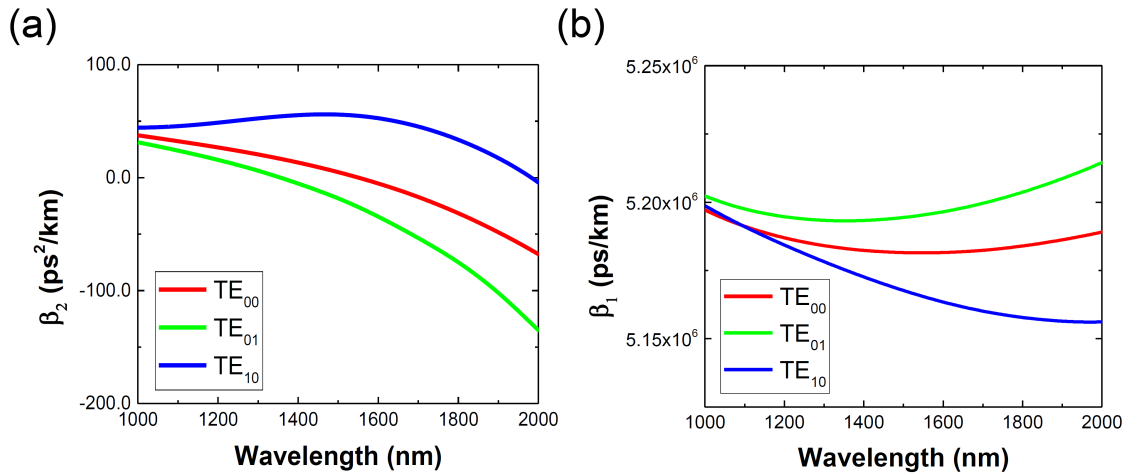


Fig. 5.8: Dispersions used for numerical calculation. The cavity is the same as that shown in Fig. 5.1. The major diameter is 100 μm and the minor diameter is 8 μm . (a) β_1 is the inverse of the group velocity. (b) β_2 is the second-order dispersion including material and geometrical dispersion.

Equation 5.6 shows the behavior of a pump mode that couples with a signal mode via cross-phase modulation and Raman scattering. The Raman scattering terms include the response from its own intensity, the coupled light intensity, and the interaction between two modes. It should be noted that only the pump mode is excited by an external source. Therefore, the signal mode receives energy only through the Raman scattering, as described in Equation 5.7. Mode overlapping is considered with effective mode area A_{ps} and described as

$$\Gamma = \frac{n_2 \omega}{c A_{\text{ps}}}, \quad (5.8)$$

$$A_{\text{ps}} = \frac{\iint |E_p(x, y)|^2 dx dy \iint |E_s(x, y)|^2 dx dy}{\iint |E_p(x, y)|^2 |E_s(x, y)|^2 dx dy}, \quad (5.9)$$

where n_2 is the nonlinear coefficient of a material. When calculating Lugiato-Lefever equations, we assume that Γ_p and Γ_s have the same value, for simplification. The Raman scattering terms, namely the Raman contribution f_R and the Raman response function h_R , are well-known values where $f_R = 0.18$ and h_R is described as

$$h_R = \frac{\tau_1^2 + \tau_2^2}{\tau_1 \tau_2^2} \exp\left(-\frac{t}{\tau_2}\right) \sin\left(-\frac{t}{\tau_1}\right), \quad (5.10)$$

Here, $\tau_1 = 12.2$ fs and $\tau_2 = 32$ fs⁵¹). Although Raman scattering has gain in the orthogonal modes, the efficiency is small, and the conversion to orthogonal modes can be neglected¹³⁸). Thus, we consider Raman modes to have the same polarization as a pump mode.

Table. 5.2: The parameters for the calculation for Figures 5.9.

Q_{TE00} in (c)	1.5×10^7	n_2	2.2×10^{-20} W/m ²
Q_{TE01}	5×10^6	f_{FSR}	660 GHz
Major radius	50 μm	detuning	0
Minor radius	4 μm	input power	1 W

To explain the experimental results, we set a pump mode with a Q of 5.0×10^6 . Based on a theoretical understanding, the Q factor ratio, $Q_{\text{Raman}}/Q_{\text{pump}}$, was used as a parameter. Figure 5.9(a) shows the calculated results when TE_{01} and TE_{00} were set as the pump and Raman modes, respectively. The vertical axis is the integrated light power of the generated stimulated Raman scattering mode. Since each calculation time is tens of thousands of round-trip times, the cavity should be in a steady state. When the Q factor ratio is 2, the Raman power suddenly increases, which means that the gain overcomes the cavity loss. The value agrees with the theoretical prediction, as discussed above and shown in Figure 5.9(b). The optical spectrum for a ratio of 3, which corresponds to our experimental val-

ues, is shown in Figure 5.9(c). The spectrum had the same shape as the experimental result shown in Figure 5.4(b). On the other hand, when we pumped at a higher mode, we obtained the spectrum shown in Figure 5.9(d). The Raman power did not increase, and this is in close agreement with Figure 5.4(a). This calculation confirmed that the origin of the dual comb-like spectrum was the result of mode interaction between the pump and Raman modes via Raman scattering. Also, the ratio of the Q values played an important role in determining the strength of the mode interaction.

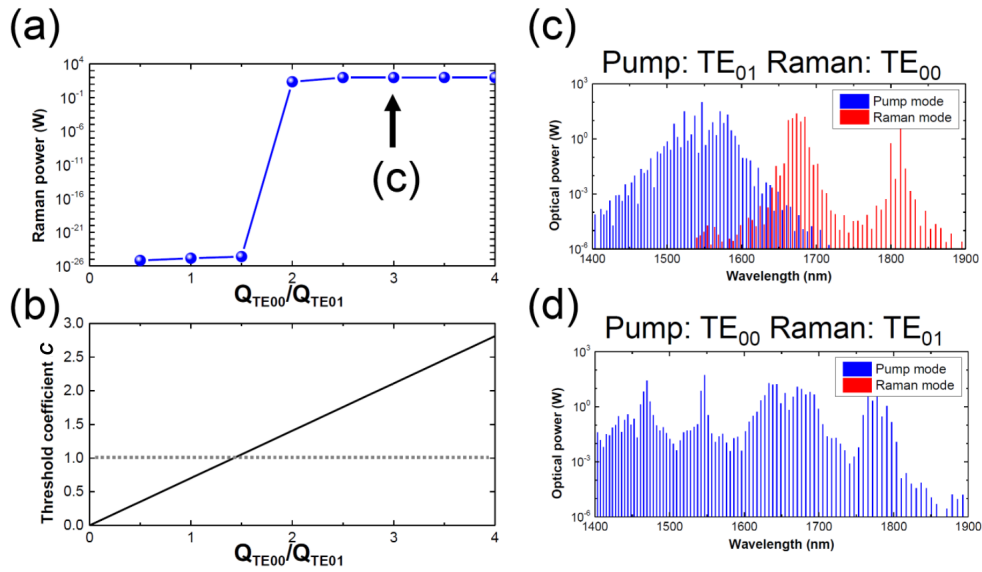


Fig. 5.9: Simulation results with the model we used in experiments. Input power is set as 1 W. (a) Integrated power of SRS modes versus Q_{TE00}/Q_{TE01} . The Q of the TE_{01} mode is defined as 5.0×10^6 . As Q_{TE00}/Q_{TE01} increases and exceeds 2, the SRS mode power increases rapidly, because the gain exceeds the threshold of SRS. (b) The theoretical threshold coefficient C mentioned in section 5.2. (c) The optical spectrum when $Q_{TE00}/Q_{TE01} = 3$. (d) High- Q mode pumping with the same Q ratio as (c). No transverse mode coupling was observed.

5.4 Summary

In this chapter, transverse mode interaction via stimulated Raman scattering in a silica toroid microcavity was discussed. Theoretical analysis suggested that a mode interaction is dominant when a low- Q mode is pumped. Experimental results confirmed the theoretical analysis. Interestingly, a mode interaction via

stimulated Raman scattering and common four-wave mixing form a dual-comb like spectrum. Finally, a numerical model was developed, and the numerical results were also in close agreement with the theoretical and experimental results.

Chapter 6

Broad bandwidth third-harmonic generation via four-wave mixing and stimulated Raman scattering

This chapter describes broad-bandwidth third-harmonic generation assisted by four-wave mixing and stimulated Raman scattering in a silica toroid microcavity. Third-harmonic generation is basically a simple triple frequency that occurs from the frequency of a pump due to third-order nonlinearity. However, a more complex process, called third-order sum-frequency generation, often occurs in a high-Q silica toroid microcavity, so that not only third-harmonic generation but also four-wave mixing and stimulated Raman scattering play key roles in determining third-harmonic light emission. Experimentally, a comb-like spectrum covering 498–611 nm is observed with a near-infrared pump.

Section 6.1 describes third-harmonic generation in a silica toroid microcavity. How phase-matching is satisfied in the cavity is discussed. Section 6.2 shows some experimental results, which verify that four-wave mixing and stimulated Raman scattering influence third-harmonic light emission. Section 6.3 explains dispersive wave emission, which provides access to a blue-color emission.

6.1 Third-harmonic generation

While a frequency comb in the visible range has many promising applications, and its development is desired, microcomb research is still too sparse to be used practically. This is because the anomalous dispersion required for microcomb generation cannot be designed, due to strong normal material dispersion. Thus, since third-harmonic generation can occur even in a normal dispersion, it should provide a way to generate visible light with a high- Q cavity.

Third-harmonic generation requires two main conditions, as follows:

$$\omega_{\text{TH}} = 3\omega_{\text{pump}}, \quad (6.1)$$

$$\beta_{\text{TH}} = 3\beta_{\text{pump}}, \quad (6.2)$$

where the former is "frequency matching" and the latter is "phase matching." For a silica toroid microcavity, the modes satisfying them are calculated with an FEM. Since the angular momentum l of a whispering gallery mode indicates the number of nodes of the travelling waves, phase matching is automatically achieved when we select the modes with the relationship $l_{\text{TH}} = 3l_{\text{pump}}$ ⁹⁾. Thus, the frequency matching is worthy of attention. The considerations are different from a ring cavity, for which the effective refractive index is focused on. The difference is derived from a whispering gallery mode affected by not only the effective refractive index but also the physical mode radius. In essence, the longer a resonant wavelength, the more deeply the whispering gallery mode propagates inside. Figure 6.1 shows the calculated frequency mismatch between the pump mode and third-harmonic modes in a silica toroid microcavity with a major diameter of 80 μm and a minor diameter of 6 μm . Typically, frequency matching is satisfied when a fundamental mode is selected as a pump mode and a high-order mode is selected as a TH mode. Here, although only four modes are considered, there are many high-order modes in the cavity. Other modes can be found where third-harmonic generation occurs. It has been shown that certain kinds of high-order modes can turn into third-harmonic modes by chance.

Next, the theoretical analysis is described. The starting point is a coupled

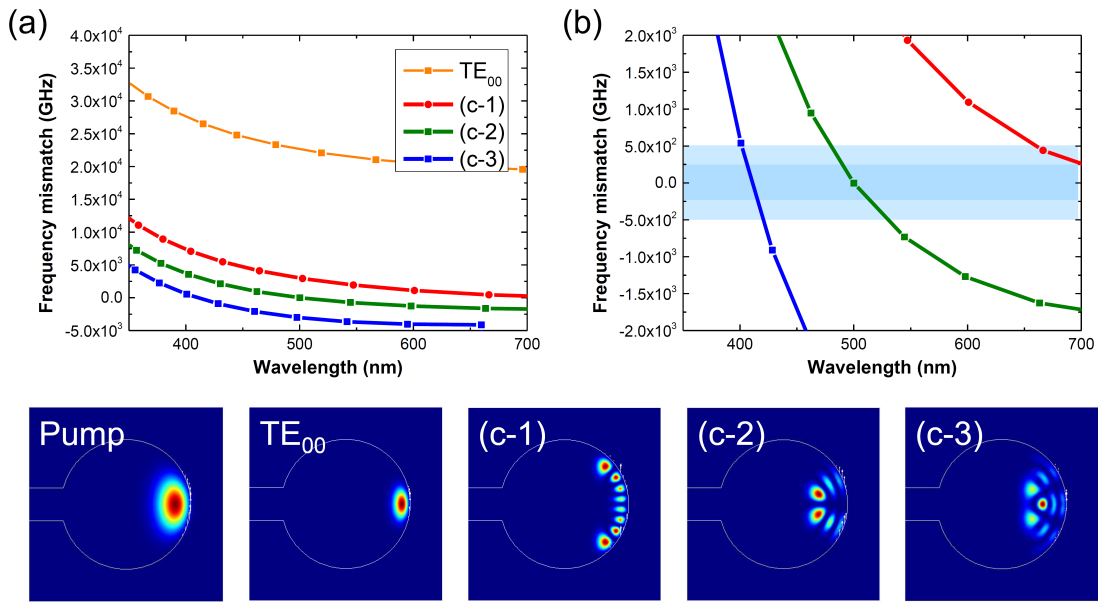


Fig. 6.1: (a) and (b) show calculated resonant frequencies of four TH modes. Since phase-matching is already satisfied by selections of the angular momentum relationship $l_{\text{TH}} = 3l_{\text{pump}}$, frequency-matching should be focused on for third-harmonic generation. The pump mode is a fundamental mode in a silica toroid microcavity. Four modes in the visible range are calculated, shown in TE₀₀ and c-1, c-2, and c-3). Light blue and dark blue areas in (b) show the bandwidths of resonant frequencies with Q s of 100 and 500.

nonlinear Schrödinger equation given by

$$\frac{\partial A}{\partial z} = -\frac{\alpha_A}{2}A - \frac{i}{2}\beta_{2A}\frac{\partial^2 A}{\partial T^2} + i\gamma_A|A|^2A + i\kappa BA^*A^*e^{-i\Delta kz}, \quad (6.3)$$

$$\frac{\partial B}{\partial z} = -\frac{\alpha_B}{2}B - \frac{i}{2}\beta_{2B}\frac{\partial^2 B}{\partial T^2} + i\gamma_B|B|^2B + i\kappa AAAe^{i\Delta kz}, \quad (6.4)$$

where A and B are electric amplitudes of a pump and a TH mode. The variables α , β_2 , γ , and κ mean propagation loss, dispersion, a nonlinear coefficient, and coupling between two modes, respectively. Δk shows the phase mismatch $k_B - 3k_A$. Equation 6.3 is transformed by the same manner¹³⁹⁾ shown in Appendix C as

$$A^n = A^{n-1} + \int_0^L \frac{\partial A}{\partial z} dz, \quad (6.5)$$

$$A^n = A^{n-1} + L \left[-\frac{\alpha_A}{2} - \frac{i}{2}\beta_{2A}\frac{\partial^2}{\partial T^2} + i\gamma_A|A|^2 \right] A + \int_0^L i\kappa BA^*A^*e^{-i\Delta kz} dz, \quad (6.6)$$

where since the last term in the right side is a function of z , the integral can be calculated as

$$\begin{aligned} \int_0^L i e^{-i\Delta kz} dz &= \frac{1}{-\Delta k} \left[e^{-i\Delta kz} \right]_0^L \\ &= \frac{1}{-\Delta k} \left(e^{-i\Delta kL} - 1 \right) \\ &= \frac{1}{-\Delta k} \left(-2 \sin \frac{\Delta kL}{2} \right) e^{-i\frac{\Delta kL}{2}} \\ &= L \frac{\sin \frac{\Delta kL}{2}}{\frac{\Delta kL}{2}} e^{-i\frac{\Delta kL}{2}} \\ &= L \cdot \text{sinc} \left(\frac{\Delta kL}{2} \right) e^{-i\frac{\Delta kL}{2}}. \end{aligned} \quad (6.7)$$

With Equation 6.7, a Lugiato-Lefever equation, including third-harmonic gener-

ation is described as

$$A^n = A^{n-1} \left(1 - \frac{1}{2}T - i\delta\right) + \int_0^L \frac{\partial A}{\partial z} dz + \sqrt{T}E_{\text{in}}, \quad (6.8)$$

$$\begin{aligned} A^n - A^{n-1} = & \left[-\frac{\alpha_A}{2}L - \frac{1}{2}T - i\delta - \frac{i}{2}\beta_{2A}L \frac{\partial^2}{\partial T^2} + i\gamma_A L |A|^2 \right] A \\ & + \kappa B A^* A^* L \cdot \text{sinc}\left(\frac{\Delta k L}{2}\right) e^{-i\frac{\Delta k L}{2}} + \sqrt{T}E_{\text{in}}. \end{aligned} \quad (6.9)$$

Note that third-harmonic generation depends on a sinc function for values of $\Delta k L/2$ denoting the phase mismatch. Here, I evaluate the phase mismatch with respect to the angular momentum l . When the angular momentum of a pump mode and that of a TH mode are l_p and l_{TH} , respectively, the phase mismatch is given by

$$\begin{aligned} \beta_{\text{TH}} - 3\beta_p &= n_{\text{TH}}k_{\text{TH}} - 3n_p k_p \\ &= n_{\text{TH}} \frac{2\pi f_{\text{TH}}}{c} - 3n_p \frac{2\pi f_p}{c} \\ &= n_{\text{TH}} \frac{2\pi}{c} l_{\text{TH}} \frac{c}{2\pi n_{\text{TH}} R} - 3n_p \frac{2\pi}{c} l_p \frac{c}{2\pi n_p R} \\ &= \frac{1}{R} (l_{\text{TH}} - 3l_p) = \Delta k, \end{aligned} \quad (6.10)$$

where R is the radius of a ring cavity. With Equation 6.10, the sinc function is described as

$$\begin{aligned} \text{sinc}\left(\frac{\Delta k L}{2}\right) &= \text{sinc}\left(\frac{2\pi R (l_{\text{TH}} - 3l_p)}{2R}\right) \\ &= \text{sinc}\{\pi(l_{\text{TH}} - 3l_p)\}. \end{aligned} \quad (6.11)$$

Thus, third-harmonic generation in a ring cavity occurs when $l_{\text{TH}} = 3l_p$ is achieved, in addition to frequency matching. If not, the sinc function exhibits zero.

6.2 Experimental results

In this section, experimental results of third-harmonic generation with a silica toroid microcavity are shown. The results reveal that not only third-harmonic generation but also other nonlinear effects can result in visible light emission.

The relationship between third-harmonic generation and four-wave mixing in the near-infrared region is explained here. Figure 6.2(a) shows the optical spectra seen when four-wave mixing occurs from a pump at 1550 nm. Seven lines are observed in the visible range. They are spaced similarly to lines with a 4.5-THz distance in the near-infrared. A "*" marks a frequency of $3f_{\text{pump}}$. This demonstrates that third-order sum-frequency generation¹⁰⁰⁾ or Bragg scattering four-wave mixing¹⁴⁰⁾ occurs. Third-order sum-frequency generation is a frequency conversion described as $\omega_{\text{TSFG}} = \omega_A + \omega_B + \omega_C$, which is the same as third-harmonic generation when A, B, and C are all the same. Bragg scattering four-wave mixing is a conversion given by $\omega_{\text{TSFG}} = \omega_{\text{TH}} + (\omega_B - \omega_A)$, which is explained as a modulation of ω_{TH} caused by $\omega_B - \omega_A$. The latter requires initial third-harmonic generation while the former doesn't. Although this result does not provide clear evidence, it does show later that third-order sum-frequency generation seems to be dominant.

Next, the relationship between third-harmonic generation and stimulated Raman scattering is shown in Figure 6.2(b). This is clear evidence that other coherent mixing processes occur besides third-harmonic generation. The numbers "1,2,3,4" show frequencies of $3\omega_p$, $2\omega_p + \omega_{\text{RS}}$, $\omega_p + 2\omega_{\text{RS}}$, and $3\omega_{\text{RS}}$, respectively. Thus, it is seen that the stimulated Raman scattering light is coherent with the pump, and it causes coherent mixing that generates visible light. Figure 6.2(c) shows the result when cascade-stimulated Raman scattering occurs. Five lines are observed in the visible range, showing that multi-wavelength generation in the near-infrared region is needed to obtain the same number of lines in the visible region. Figures 6.3(a) and (b) show broad visible light emissions covering over 100 THz. In the near-infrared region, the broad-bandwidth spectrum is obtained via the combination of four-wave mixing and stimulated Raman scattering, which causes broad-bandwidth visible light emission through third-harmonic generation. Comparison between Figures 6.3(a) and (b) shows that short wavelengths

(< 500 nm) are obtained only in (a), while long wavelengths (> 620 nm) are only in (b). This result is indirectly influenced by the spectra in the near-infrared, which suggests that the control of those spectra has the potential to achieve the desired spectrum in the visible region.

6.3 Dispersive wave emission

This section discusses blue light emission with a dispersive wave caused by third-order dispersion. A dispersive wave is a kind of four-wave mixing process that occurs in a pulse propagation¹⁴¹⁾. In the context of microcomb generation, it occurs simply because of phase matching, even from a continuous wave. In a dispersive wave emission, blue light, which is shorter than green, is generated by a pump at 1550 nm.

In a microcavity, a dispersive wave requires phase matching, and the point where it occurs is described as^{84,85)}

$$D_{\text{int}} = \frac{1}{2}D_2\mu_{\text{DW}}^2 + \frac{1}{6}D_3\mu_{\text{DW}}^3 = 0, \quad (6.12)$$

$$\mu_{\text{DW}} = -3\frac{D_2}{D_3}, \quad (6.13)$$

where μ_{DW} is the mode number from the pump mode at which a dispersive wave occurs. The other parameters have a relationship given by

$$\omega_\mu = \omega_0 + D_1\mu + \frac{1}{2}D_2\mu^2 + \frac{1}{6}D_3\mu^3, \quad (6.14)$$

where ω_0 is the pump mode, ω_μ is the μ -th mode from the pump, D_1 is a FSR, D_2 is a cavity dispersion, and D_3 is a third-order dispersion. Thus, a dispersive wave is generally observed with the D_2 of near zero. $D_{\text{int}} = 0$ means that the effective refractive index of the μ -th mode is same as that of the pump mode, which satisfies phase-matching. The underlying physics of the wavelength conversion of the dispersive wave emission is not clear yet although it is regarded as a kind of Cherenkov radiation¹⁴¹⁾.

Figure 6.4(a) shows a typical spectrum of dispersive wave emission in a sil-

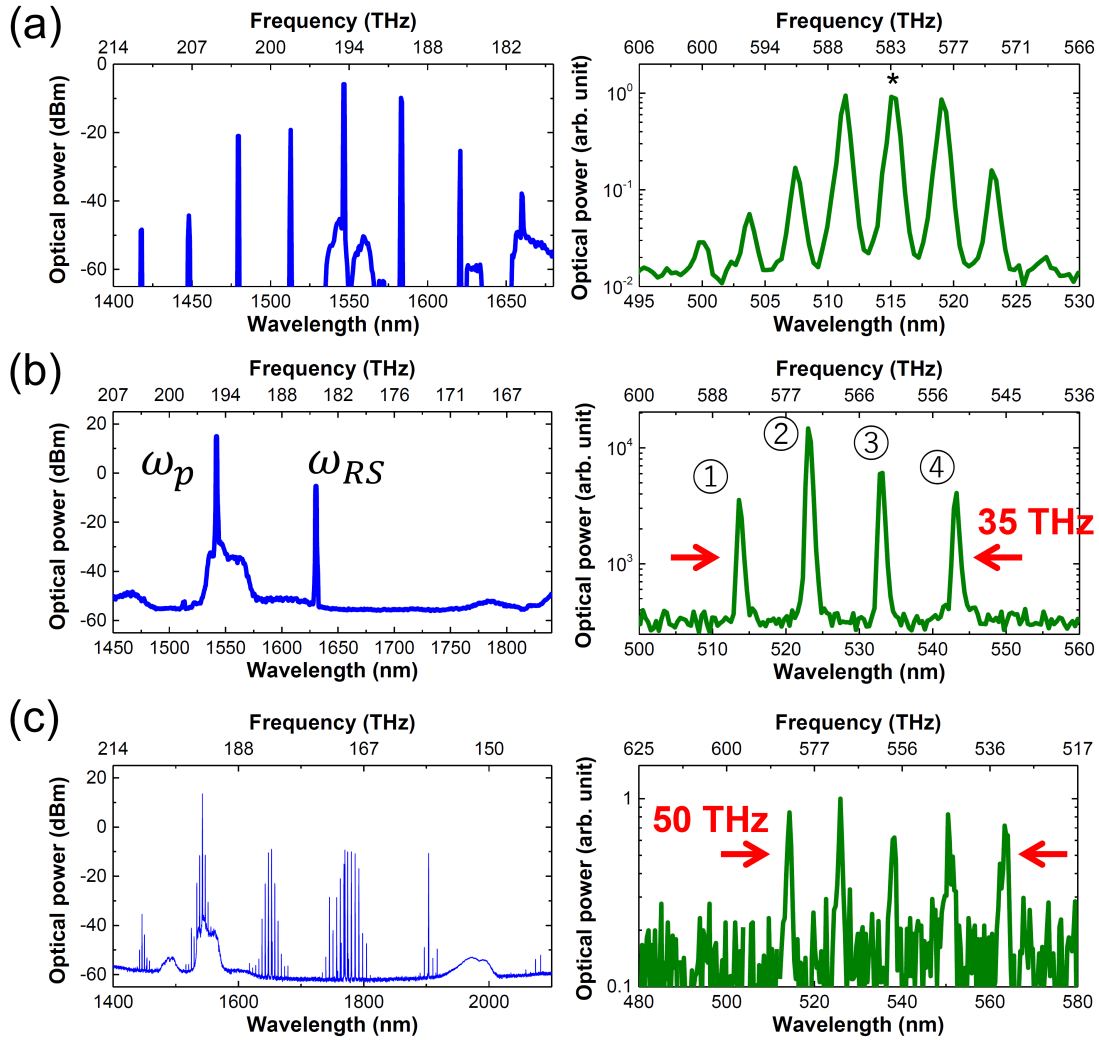


Fig. 6.2: (a) IR and visible spectra when the pump laser operated at 1545.9 nm and 0.94 W. The longitudinal mode spacing of the Kerr comb was 5-FSR. The thick line width of each longitudinal mode was due to the limited wavelength resolution of the spectrometer. (b) Spectra obtained when we pumped the cavity with 1542.2 nm at 0.5 W. A single Stokes signal at 1630 nm was obtained. (c) Measured spectra when the pump laser operated at 1542.56 nm at 0.5 W. High-order SRS at an 11-FSR interval was observed at the IR wavelength. The generated visible light had a bandwidth of 50 THz with a frequency spacing of 11 FSR. The resolution of the spectrometer used to measure the visible light was insufficient to resolve each FSR line, but each spectral component had a frequency spacing of 11 FSR.

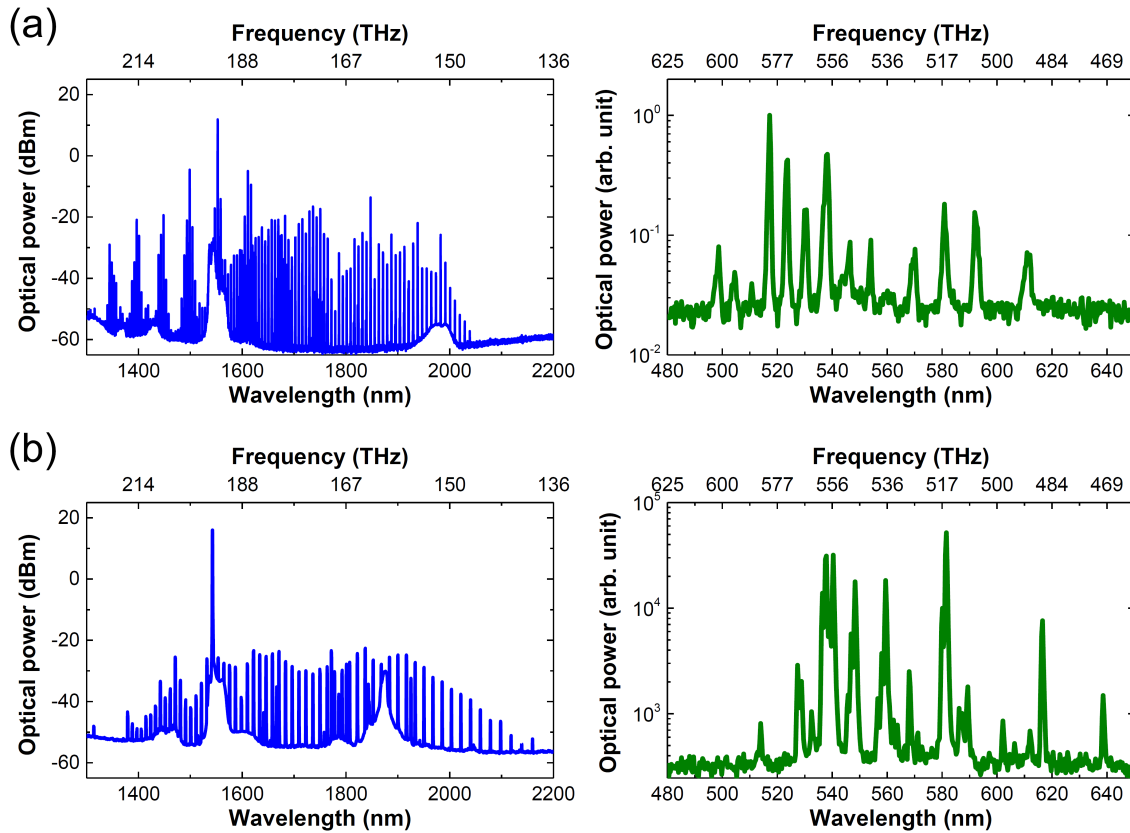


Fig. 6.3: (a) Measured spectra when the pump laser operated at 1551.6 nm and 1 W. The bandwidth of the generated light was very large, at 110 THz. (b) Different pump conditions.

ica toroid microcavity. The 22nd mode is a peak influenced by dispersive wave emission. Figure 6.4(b) describes calculated D_{int} of the fundamental mode of silica toroid microcavities with different major diameters (26, 26.5, and 27 μm) at a 1550-nm pump. Although the peak point strongly depends on the structure of the cavity, it should be noted that engineering of the point is possible when designing the cavity structure. For a silica toroid microcavity with a diameter of around 50 μm , the dispersive wave point tends to be located at a shorter wavelength than the pump. Thus, it is a way to generate high-power short wavelengths (< 1550 nm pump), which contributes to generation of blue and shorter wavelengths.

Figures 6.5(a), (b), and (c) indicate 433- and 457-nm light emissions in a silica toroid microcavity. First, 1300- and 1860-nm light occurred from a 1550-nm pump. Because the wavelengths are very different from the pump, they should be categorized not as stimulated Raman scattering but as dispersive wave emission, described by Equation 6.12. In the visible region, 433-nm light and third-harmonic generation of the 1300-nm light were observed. Then, the detuning of the input was changed so that more power was coupled to the cavity. As a result, 457-nm light, third-order sum-frequency generation of two 1300-nm lights, and one 1550-nm light occurred, as seen in Figures 6.5(b) and (c). Thus, we found that it is possible to design visible light emission through engineering of dispersive wave emission in a silica toroid microcavity.

6.4 Summary

In this chapter, I described how third-harmonic generation is achieved in a silica toroid microcavity. In particular, attention should be paid to frequency-matching, because the phase-matching is satisfied by the selection of modes given by $l_{\text{TH}} = 3l_{\text{p}}$. Double measurements of near-infrared and visible regions show clear relationships between them, which indicate that four-wave mixing and stimulated Raman scattering affect visible light emission. Dispersive wave emission also affects blue light emission, which shows the possibility of generating purple and ultraviolet light.

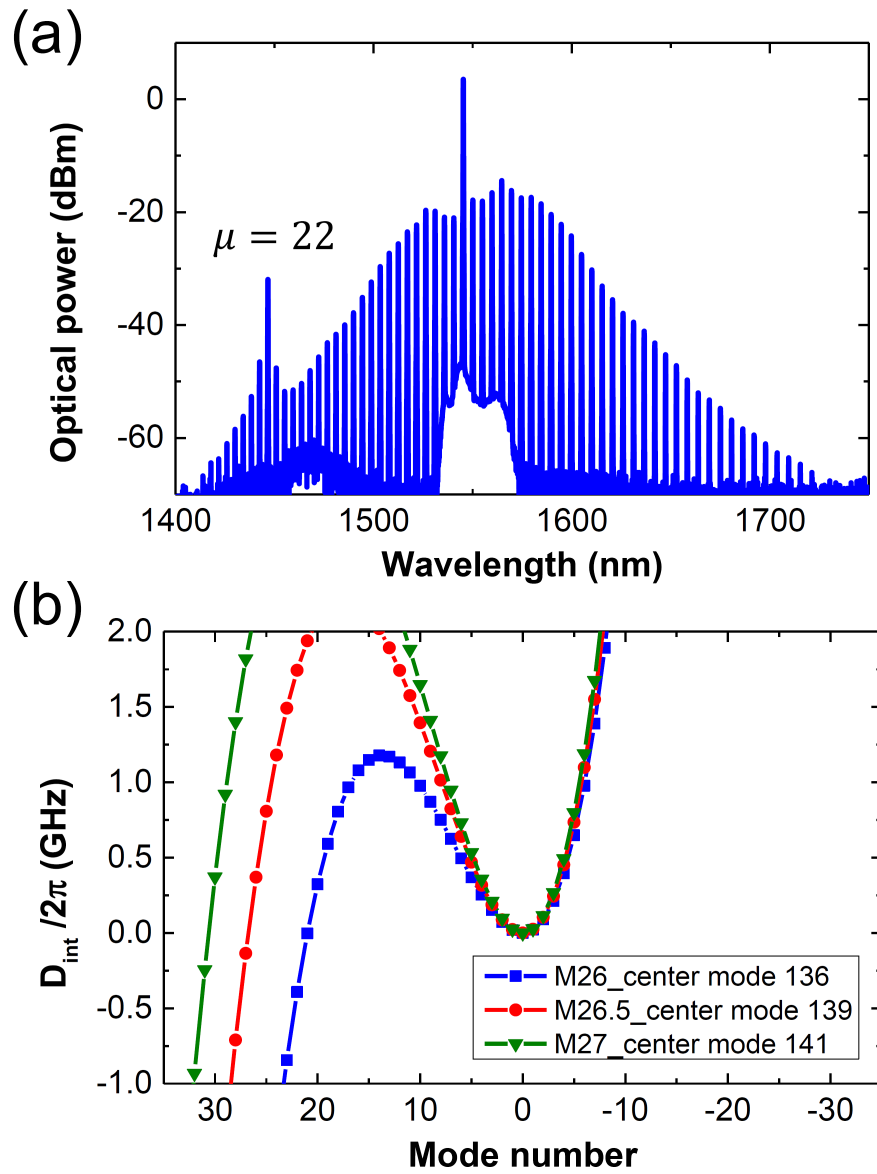


Fig. 6.4: (a) Typical dispersive wave emission with a silica toroid microcavity. Mode number $\mu = 22$ is the emitting point. (b) Calculated dispersion parameters with different geometrical parameters in a silica toroid microcavity.

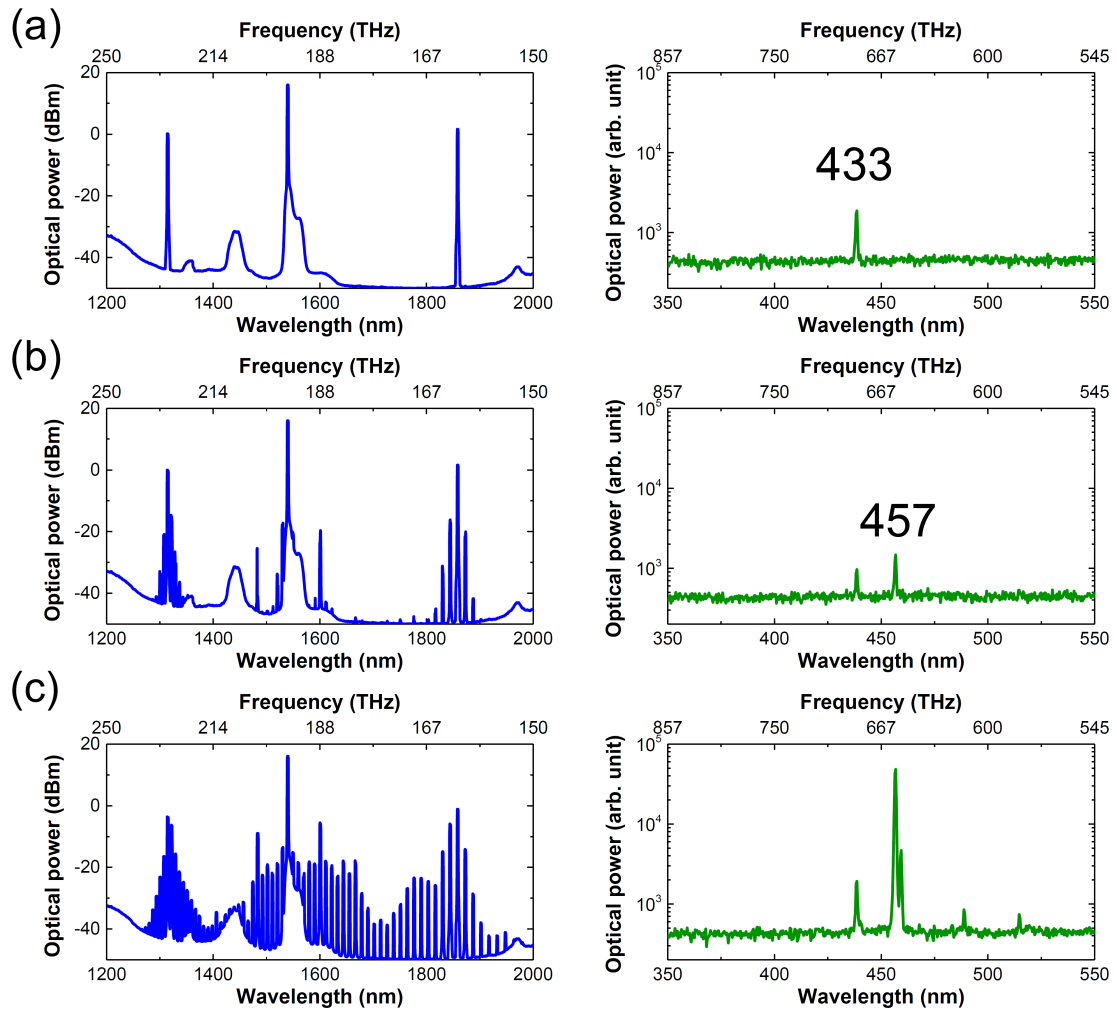


Fig. 6.5: Optical spectra with pump conditions of (a) 1539.72 nm, (b) 1539.75 nm, and (c) 1539.80 nm. As coupled power was increased, dispersive wave emission and blue light emission also increased.

Chapter 7

Summary and outlook

7.1 Summary

This dissertation studied nonlinear optical processes with a silica toroid microcavity for optical frequency comb generation. The underlying physics of the generation of the discrete spectrum from a continuous-wave pump via third-order nonlinearity-based optical effects in silica (four-wave mixing, stimulated Raman scattering, and third-harmonic generation) were investigated. High- Q cavities including a silica toroid microcavity enables application using nonlinear optical effects to be readily accessed. This dissertation paved the way for achieving optical frequency comb generation in the visible and the telecom with a silica toroid microcavity.

Hysteresis behavior of microcomb generation (Chapter 3)

A novel way to achieve a mode-locked microcomb was presented. It was found that input power scanning can induce mode-locking, because it moves the nonlinear cavity system to the upper branch from the lower, which has the same effect of input wavelength sweeping. Input power control is useful in the region where there is no reasonable tunable laser, such as the mid-infrared. This is the first demonstration that a mode-locked microcomb can be generated with a silica toroid microcavity, which, because it exhibits ideally ultrahigh- Q , has the potential to access mode-locked microcombs below 1 mW.

Influence of stimulated Raman scattering on microcomb generation in a silica cavity (Chapter 4)

Gain competition between four-wave mixing and stimulated Raman scattering was studied. Although comparison of maximum gains was conducted, the effect of free-spectral range also affects the competition. It was found that the unknown transition between two states, where either four-wave mixing or Raman scattering is dominant, occurs in a silica cavity. The effect of free-spectral range is striking in a large-FSR silica cavity like a silica toroid microcavity. This study contributed to the development of the method to control Raman lasing and microcomb generation in a large-FSR silica cavity.

Transverse mode interaction via stimulated Raman scattering combs in a silica toroid microcavity (Chapter 5)

A mode interaction via stimulated Raman scattering in a silica toroid microcavity was investigated analytically and experimentally. Mode interaction depends on the relationship of Q s of the pump mode and the Raman mode. When the pump is in a low- Q mode family, mode interaction occurs, and the Raman comb is excited in a higher- Q mode family. As a result of mode interaction, a dual-comb-like spectrum was obtained. Numerical simulation was also performed, and the calculated results agreed well with the experimental results. This study gave a deep understanding of the mode interaction and contributed to the development of the method to generate broad Raman comb or dual-mode combs in a silica toroid microcavity.

Broad bandwidth third-harmonic generation via four-wave mixing and stimulated Raman scattering (Chapter 6)

In a silica toroid microcavity, third-harmonic and third-order sum-frequency generation were presented. By measuring spectra in the near-infrared and the visible, clear relationships were found. A comb spectrum in the near-infrared, resulting from four-wave mixing and stimulated Raman scattering, induced a visible comb via third-harmonic generation. Thus, broad spectrum in the near-infrared is required for broadening the visible spectrum. Therefore, engineering a spectrum in the near-infrared is necessary to obtain the desired spectrum in the vis-

ible. It was also found that dispersive wave emission is one method of achieving blue light emission. This study paves the way to generate broad visible spectrum with a continuous-wave input, which is useful for biological imaging and optical clocks.

7.2 Outlook

Nonlinear optical processes with high- Q cavities has been extensively researched. With the knowledge accumulated so far, some applications are foreseen and may be realized in the near future.

Visible combs

Although microcomb generation in the near-infrared has been investigated for a decade, microcomb generation in the visible and ultraviolet are still in progress. Silica toroid microcavities have high high- Q even in the visible because the surface scattering is ultimately low, due to the laser reflow process. Rayleigh scattering is the main cause of decreased high- Q in the short wavelengths because the scattering loss is inversely proportional to the fourth power of the wavelength. Therefore, silica toroid microcavities, which have the ultimate smooth surface, are promising for achieving microcomb generation in the visible. Recently, microcomb generation in the normal dispersion has been extensively researched; these studies should provide useful information for our objectives, because strong material dispersion is inevitable in silica toroid microcavities.

Mode-locked Raman combs

Broad bandwidth of Raman gain is a unique characteristic of silica toroid cavities. Although single-mode Raman lasing has been much researched, multi-mode Raman lasing is still unclear, though interesting from the point of view of mode-locking. Recently, some groups have reported mode-locking operations of Raman combs^{94,95}). Thus, if a broad Raman comb generated in a silica toroid microcavity can be mode-locked, this is also a reasonable way to obtain a mode-locked comb in the long wavelengths. The dual-mode family, as discussed, may be used for dual-comb generation if we can obtain mode-locking at both modes.

Engineering of visible light emission

Visible light emission via third-harmonic generation is controlled by the spectrum in the near-infrared. By engineering the spectrum in the near-infrared, arbitrary visible light emission is achieved. For example, dispersive wave emission is a strong way to generate blue and shorter-wavelength lights. Purple and ultraviolet light generation with a silica toroid microcavity is a topic of interest.

This dissertation investigated nonlinear optical processes (four-wave mixing, stimulated Raman scattering, and third-harmonic generation) with a silica toroid microcavity for optical frequency comb generation. Silica toroid microcavities have great potential to be used as comb sources. The cavity with the Q of beyond 100 million realizes a low-consumption comb source, which requires a continuous-wave input below 1-mW. The finding of the method to achieve mode-locking in the thesis eliminates the necessity of tunable laser. Thus, fixed wavelength lasers such as semiconductor lasers can work as the input, which makes the setup simple and compact. A coupling with a tapered fiber contributes high efficiency. However, the integration of a silica waveguide for a silica toroid microcavity is demonstrated¹⁴²⁾. Thus, the silica toroid microcavity will be a compact and highly efficient comb source for the near future. This study may be a guide and reference for future research on nonlinear optical processes, and it paves the way for achieving practical applications with a compact comb source.

Appendix A

Polygonal silica toroid microcavities for stable coupling

A.1 Polygonal cavities

In this section, octagonal-shaped cavities are analyzed. Unlike circles, octagons have several corners and sides. Using an analogy of directional couplers, a coupling with a side should be different from that with a corner. With an FDTD calculation, the performance of octagonal cavities is evaluated.

First, a representative model is shown in Figure A.1(a). I modeled a curved octagonal shape because the edges are smoothed by laser reflow. The radius r , the side length d , and curvature radius r_p were 50 μm , 10 μm , and 38.1 μm , respectively. Calculated areas were $3r \times 3r$, and the thickness of a perfect matching layer was 3, as shown in Figure A.1(b). The resolution was defined as $1/\Delta x$, which determined the time step $\Delta t = 0.5\Delta x$. In this appendix, $\Delta x = 0.05$ was used.

Using an FDTD calculation, two whispering gallery modes were calculated as shown in Figure A.2. A quasi-whispering-gallery mode with a Q of 4.5×10^4 , which reflects from each side, is shown in Figure A.2(b). On the other hand, the perturbed whispering gallery mode in Figure A.2(a) exhibits a Q of 8.8×10^6 . Note that the trajectory is close to the surface at the corner and far from the surface at the side. The latter has a reasonably high Q for nonlinear optics. It should be noted that both modes propagate in a unique trajectory. For a quasi-whispering gallery mode, each side is a reflection point at which the evanescent field strongly

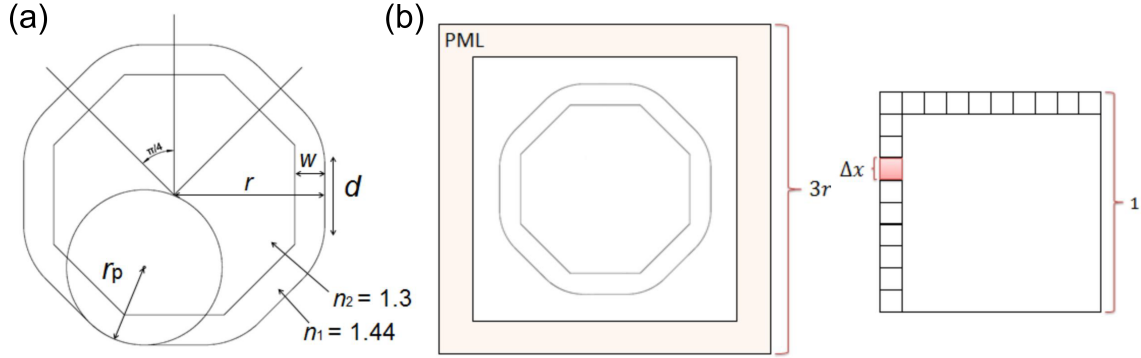


Fig. A.1: (a) Calculated model of a polygonal cavity. The profile of the refractive index is set for silica toroid cavities. The curvature radius is formed by a laser reflow process. (b) Calculation area in the FDTD simulation. Resolution is defined as Δx .

leaks. In contrast, a large evanescent field occurred at the corners in a perturbed whispering gallery mode, as shown in an inset in Figure A.2. By utilizing these differences, the control of coupling coefficient should be achieved.

Figure A.3 shows coupling Q factors of a perturbed whispering gallery mode with different cavity-fiber gaps. The waveguide is assumed to be a 1- μm tapered fiber of which the refractive index is 1.44. Blue stars and red dots are coupling Q s when it is at parallel coupling and corner coupling, respectively. Note that every point with parallel coupling is higher than those with corner coupling at the same gap. Coupling Q s when there is contact between the cavity and the fiber are 3.2×10^5 for a parallel coupling and 3.5×10^4 for a corner coupling. With a further optimally designed cavity, a much higher Q should be obtained even when in the contact condition, which provides stable operation of a silica toroid cavity, thus maintaining high Q .

A.2 Fabrication process

In this section, the fabrication process of an octagonal silica toroid cavity is outlined. A solution for anisotropic etching was used and, as a result, an octagonal silicon post was formed. The silica toroid shape was fabricated after CO_2 laser reflow. The fabricated cavity exhibited an experimental Q of 2.2×10^4 .

The shape of a silica toroid cavity is defined by the shape of the silicon post

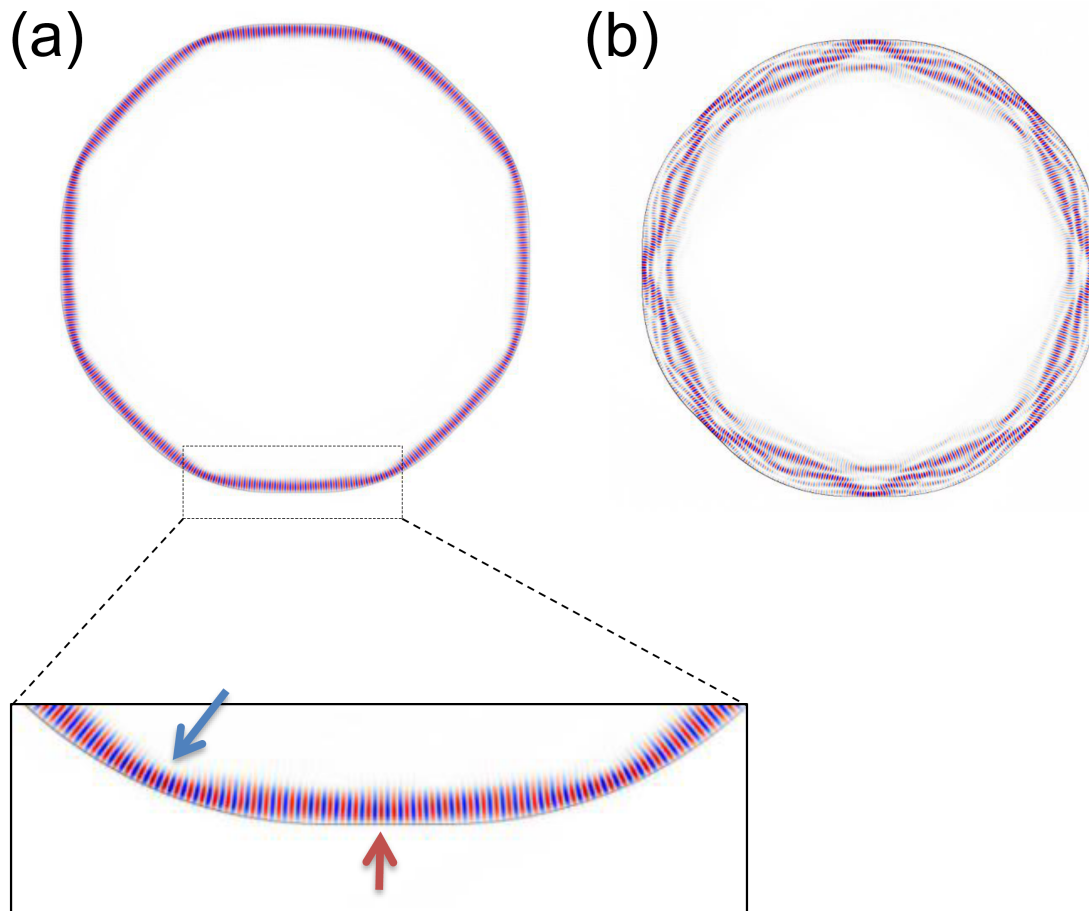


Fig. A.2: Calculated whispering gallery mode an octagonal cavity exhibits. (a) Perturbed whispering gallery mode. (b) Quasi-whispering gallery mode. Inset: the trajectory of the perturbed whispering gallery mode.

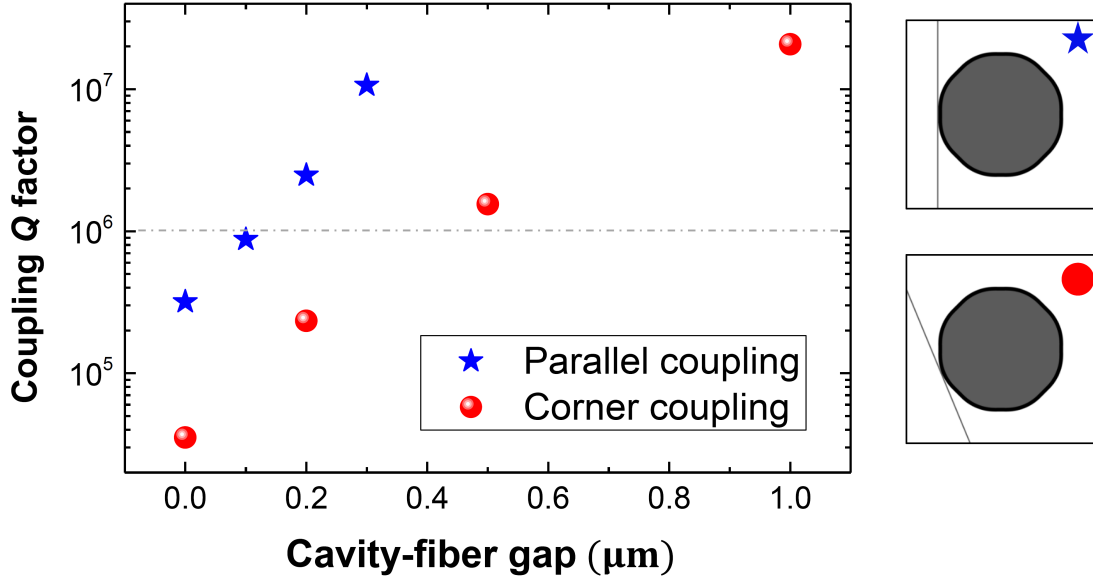
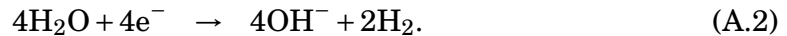
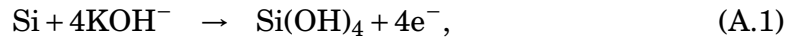


Fig. A.3: Coupling Q with different-sized gaps between the fiber and the cavity. Parallel coupling is robust with respect to the gap. Right panels show schematic images of parallel and corner coupling.

supporting the silica disk before the laser reflow process. The post works as a heat sink for the heat caused by absorption of the CO_2 laser by the silica disk. Therefore, the heat distribution depends on the capacity of the heat sink. Generally, a silica toroid microcavity is formed from a circular photomask pattern and an isotropic etching, which makes a complete cavity circle that exhibits the highest Q . A kind of anisotropic etchant is used for making a polygonal silicon post.

The solution used for anisotropic etching is potassium hydroxide (KOH). The reaction of KOH with silicon exhibits anisotropy. The reaction system is as follows:



This reaction directly etches the silicon, so that the bond structure of the silicon influences the etching. According to Seidel *et al.*¹⁴³⁾, the etching speed of KOH

on each crystal plane of the silicon, which is classified as having a diamond cubic crystal structure, has a relationship given by

$$\langle 100 \rangle : \langle 110 \rangle = 2 : 3. \quad (\text{A.3})$$

If the orientation of a silicon substrate is set as shown in Figure A.4(a), the part building a silicon post is surrounded by crystal planes $\langle 100 \rangle$ and $\langle 110 \rangle$. So, the crystal plane $\langle 100 \rangle$, for which the etching speed is slow, is dominant. When etching time is relatively long, a square shape covered by $\langle 100 \rangle$ should be made. For the three dimensional structure, the etching rate $\langle 100 \rangle : \langle 111 \rangle = 400 : 1$ is known. However, with respect to two dimensions, we can obtain an octagonal shape by using relevant-time KOH etching, as shown in Figure A.4(b).

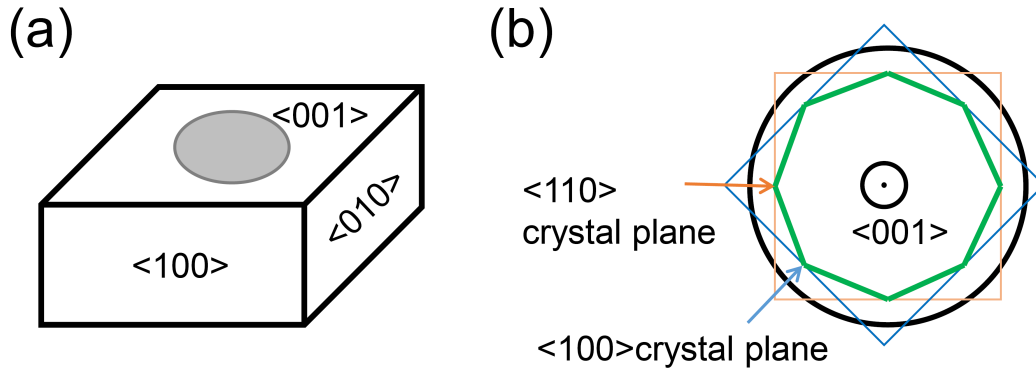


Fig. A.4: (a) A profile of crystal planes for fabricating an octagonal cavity. (b) Crystal planes from the top view.

The fabrication method is as follows:

1. KOH solution (48%) is prepared in a Teflon beaker.
2. The solution temperature is controlled at $^{\circ}\text{C}$ with a thermostat chamber.
3. A silicon chip placed in a Teflon cage and put in the beaker.
4. After a certain time, the cage is withdrawn and rinsed with ultra-pure water.

Figures A.5(a) and (b) show optical images after 4.5 h and 6h of KOH etching, respectively. Although octagonal shapes were obtained, the amount of under-etching was not enough to move the next step, the laser reflow. It does not work

to use a longer etching time, because the octagonal post will collapse and become a square post. Thus, to obtain better under-etching with an octagonal post, a combination of isotropic and anisotropic etching was used.

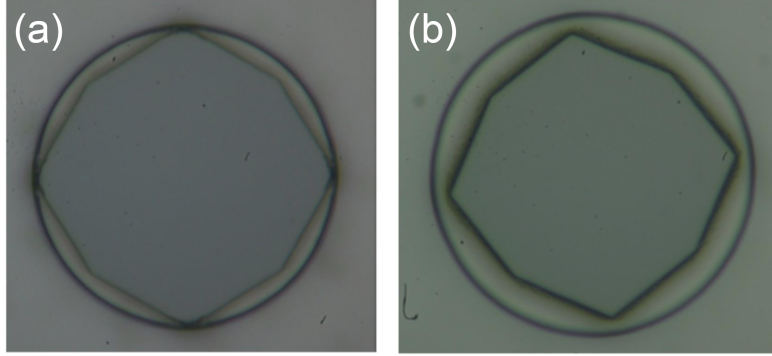


Fig. A.5: Optical images after KOH etching in which the etching time is (a) 4.5 hours and (b) 6 hours.

Figure A.6(a) shows optical images after photolithography, after isotropic etching, and after anisotropic etching. Due to additional isotropic etching, enough underetch was obtained after the anisotropic etching so that an octagonal post remained. With a laser reflow process, an octagonal silica toroid microcavity can be fabricated, as shown in Figure A.6(b).

Finally, an experimental result is shown in Figure A.7. Red and black lines are transmittance spectra with tapered-fiber contact around a reasonably high- Q mode supposed as a perturbed whispering gallery mode. The loaded Q s were 2.2×10^4 with parallel coupling and 6.3×10^3 with corner coupling. These values are in close agreement with the numerical results, which suggests that parallel coupling has a high coupling Q because the evanescent field on a side leaks less than that on a corner. This proves that coupling efficiency is controlled by changing the coupling point, because a deformed polygonal cavity with a perturbed whispering gallery mode has a unique trajectory.

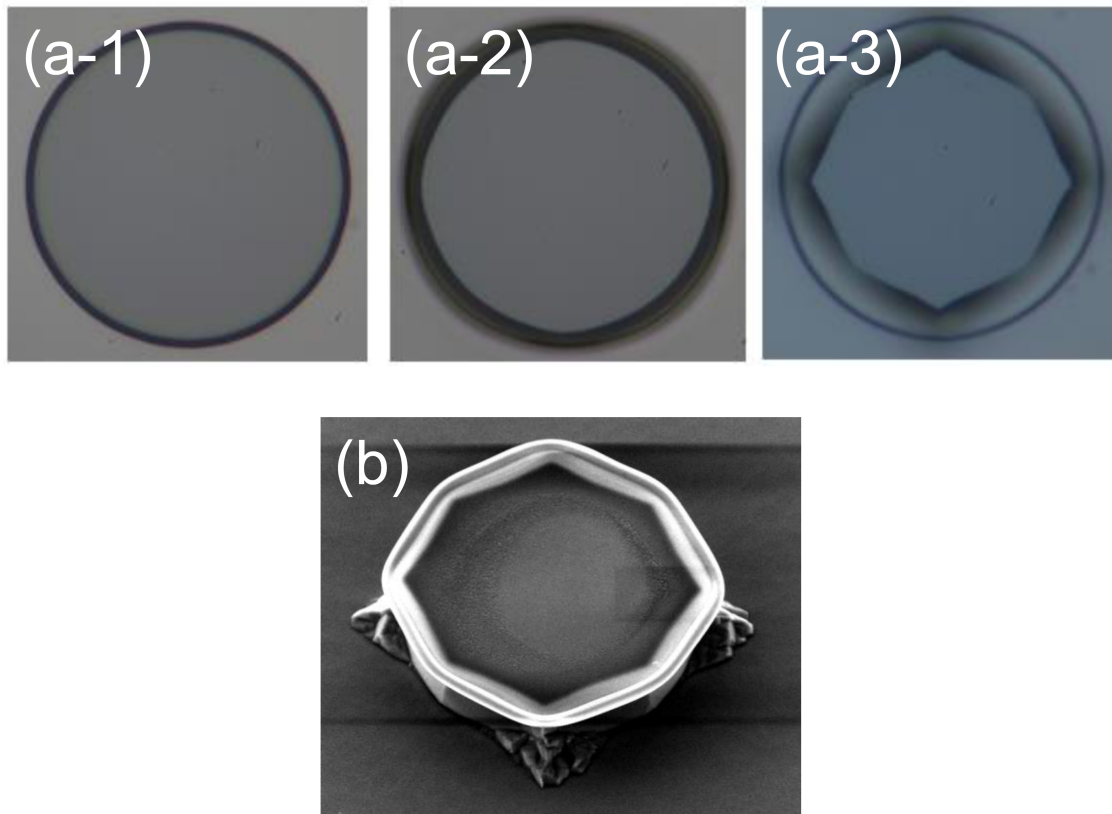


Fig. A.6: (a) Optical microscope images of a disk cavity for forming an octagonal silicon post. (a-1) After photolithography. (a-2) After isotropic etching. (a-3) After anisotropic etching. (b) Scanning electron microscope image of a fabricated octagonal toroidal microcavity after the laser reflow.

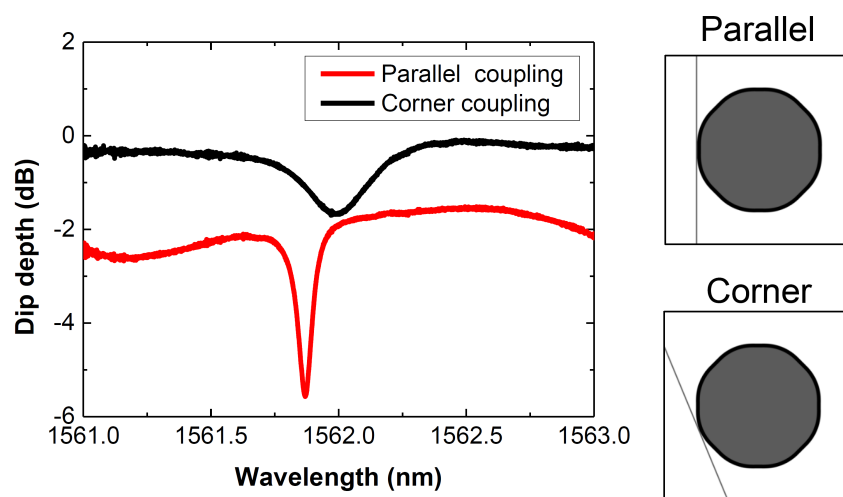


Fig. A.7: Experimental transmittance spectra with a fiber-contact condition at a parallel coupling and a corner coupling.

Appendix B

Theory of optical cavity

B.1 Derivation of a relationship between FWHM and Q -factor

To understand the theory of optical microcavities clearly, it is helpful to use a model of a Fabry-Perot cavity with two mirrors placed parallel to each other in space. In the model, light is propagated in the space and reflects off the mirrors repeatedly. The cavity confines light that satisfies a condition determined by the cavity length L . The condition is that the amount of phase shift the light experiences during a round trip is proportional to $2\pi \cdot n$, where n is an integer. Therefore, the resonant condition is expressed as follows:

$$k \cdot 2L = m \cdot 2\pi, \quad (\text{B.1})$$

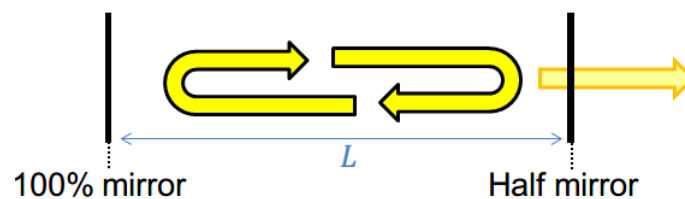


Fig. B.1: Fabry-Perot resonator model. The cavity length per one round trip is $2L$.

where k is the wavenumber of the light, and m is an integer. From here, resonant conditions with respect to frequency and wavelength are described as

$$\nu_m = m \cdot \frac{c}{2L}, \quad (\text{B.2})$$

$$\lambda_m = \frac{2L}{m}. \quad (\text{B.3})$$

Equations B.2 and B.3 show that the resonant frequencies in a Fabry-Perot cavity are spaced equidistantly, whereas the resonant wavelengths are not. The distance of the mode spacing is called the "Free Spectral Range" (FSR):

$$\nu_{\text{FSR}} = \frac{c}{2L}, \quad (\text{B.4})$$

$$\lambda_{\text{FSR}} = \frac{\lambda^2}{2L}. \quad (\text{B.5})$$

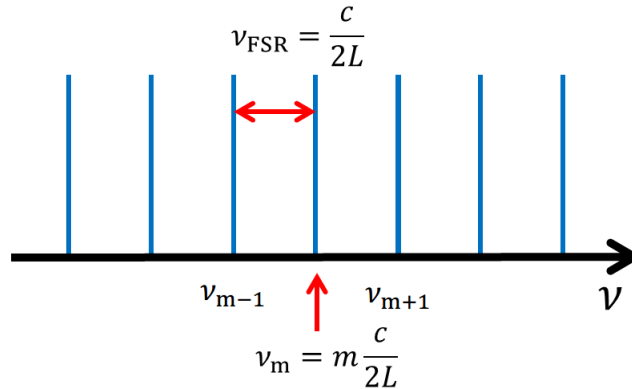


Fig. B.2: Schematic of a resonant frequency spectrum. In the frequency domain, the resonant frequencies are spaced equidistantly at intervals of ν_{FSR} .

Theoretically, the linewidth of a resonance is zero, namely the resonant spectrum is a delta function. But, when a cavity exhibits light loss, the linewidth of the resonant frequency broadens. When α and $\varphi = k \cdot 2L = \frac{4\pi\nu L}{c}$ stand for propagation loss coefficient and an amount of phase change per a round trip ($2L$) in a cavity, an electric amplitude in the cavity is described as

$$E = E_0 + \alpha e^{-i\varphi} E_0 + (\alpha e^{-i\varphi})^2 E_0 + (\alpha e^{-i\varphi})^3 E_0 \dots \quad (\text{B.6})$$

$$= \frac{E_0}{1 - \alpha e^{-i\varphi}}. \quad (\text{B.7})$$

With this infinite geometric series, the electric intensity in the cavity yields

$$I = |E|^2 = \frac{|E_0|^2}{|1 - \alpha e^{-i\varphi}|^2} = \frac{I_0}{(1 + \alpha^2 - 2\alpha \cos \varphi)} \quad (\text{B.8})$$

$$= \frac{I_0}{[(1 - \alpha)^2 + 4\alpha \sin^2 \frac{\varphi}{2}]}, \quad (\text{B.9})$$

$$I_{\max} = \frac{I_0}{(1 - \alpha)^2}. \quad (\text{B.10})$$

Here, at a point approximately near the peak of the intensity, $\sin(\varphi/2)$ can be approximated as $\varphi/2$. Note that the electric intensity near the peak is a Lorentz function of the phase change φ or the wave number k . Now, it is possible to derive a full-width half-maximum (FWHM) of the Lorentz function as

$$\Delta\nu = \frac{c(1 - \alpha)}{2\pi L \sqrt{\alpha}}, \quad (\text{B.11})$$

$$\Delta\lambda = \frac{\lambda^2(1 - \alpha)}{2\pi L \sqrt{\alpha}}. \quad (\text{B.12})$$

A detailed description of propagation loss follows. The decay rate of electric amplitude per round trip can be regarded as an exponential function, described as

$$\alpha = \exp(-\alpha_r \cdot 2L), \quad (\text{B.13})$$

where α_r is the decay rate per unit length. The counterpart per unit time yields

$$\alpha_t = c\alpha_r. \quad (\text{B.14})$$

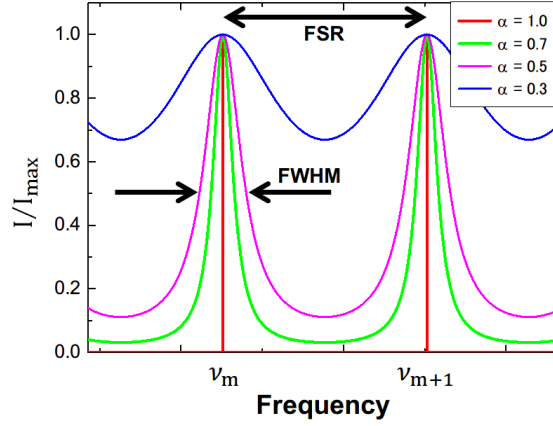


Fig. B.3: FWHM of resonant frequency spectrum. $\alpha = 1.0$ means no propagation loss.

Here, a photon lifetime is defined as the time required for the decay of the intensity to $1/e$. The photon lifetime τ_{photon} yields

$$\exp\left(-\frac{1}{2}\right) = \exp(-\alpha_t \cdot t) = \exp\left(-\alpha_t \cdot \frac{1}{2\alpha_t}\right), \quad (\text{B.15})$$

$$\tau_p = \frac{1}{2\alpha_t} = \frac{1}{2c\alpha_r}. \quad (\text{B.16})$$

Note that photon lifetime is an indicator of how strongly the cavity confines the light. With the photon lifetime τ_{photon} and energy of the resonant light $\hbar\omega_r$, the guide to the stored energy in the cavity, called a quality factor (Q), is described as

$$Q = \omega_r \tau_p \quad (\text{B.17})$$

Q , a dimensionless number, is a common index for expressing performance of a cavity. In this thesis, Q is representative of other parameters, such as photon lifetime. To obtain Q experimentally, one would measure the time required for decay of the intensity in the cavity to $1/e$, which is called the "ringdown" method. Another interpretation of Q is as follows:

$$Q = \omega_r \frac{\text{Stored energy[J]}}{\text{Power loss[W]}}. \quad (\text{B.18})$$

Since the decay of electric amplitude per unit time in the cavity is $\exp(-\alpha_t t)$, the decay of intensity per unit time yields

$$I(t + \Delta t) = \exp(-2\alpha_t \Delta t) \times I(t), \quad (\text{B.19})$$

$$\frac{dI}{dt} = -2\alpha_t \times I, \quad (\text{B.20})$$

$$Q = \omega_r \frac{I}{\frac{dI}{dt}} = \omega_r \frac{I}{-2\alpha_t \times I}. \quad (\text{B.21})$$

Note that Equation B.21 has the same meaning as B.18. Also, Q relates to the spectrum of a resonant frequency. The FWHM of the resonant frequency is described as

$$\Delta\nu = \frac{c(1-\alpha)}{2\pi L\sqrt{\alpha}} = v_{\text{FSR}} \frac{(1-\alpha)}{\pi\sqrt{\alpha}}. \quad (\text{B.22})$$

Here, given that the propagation loss α is regarded as $\exp(-\alpha_r \cdot 2L)$, with the condition that $(-\alpha_r \cdot 2L) \ll 1$, an approximation of $\exp(-\alpha_r \cdot 2L) \approx (1 - \alpha_r \cdot 2L)$ is sufficient. With the approximation, a common description indicating the relationship between Q and a spectrum of the resonant frequency yields the following:

$$\Delta\nu = v_{\text{FSR}} \frac{[1 - \exp(-\alpha_r \cdot 2L)]}{\pi \exp(-\alpha_r \cdot L)} \approx v_{\text{FSR}} \frac{1 - (1 - \alpha_r \cdot 2L)}{\pi(1 - \alpha_r \cdot L)} \approx v_{\text{FSR}} \frac{\alpha_r \cdot 2L}{\pi}, \quad (\text{B.23})$$

$$Q = \omega_r \tau_p = \omega_r \frac{1}{2c\alpha_r} = \frac{2\pi\nu_r}{2c\alpha_r} = \nu_r \frac{\pi}{c\alpha_r} \approx \frac{\nu_r}{\Delta\nu_r} \approx \frac{\lambda_r}{\Delta\lambda_r}. \quad (\text{B.24})$$

B.2 Theory of whispering gallery mode

This section describes a mathematical expression of a whispering gallery mode in a microsphere cavity^{104, 105, 144, 145}.

A description of a whispering gallery mode starts from a wave equation as follows:

$$\left(\nabla^2 - \frac{1}{v} \frac{\partial^2}{\partial t^2} \right) \psi(r, t) = 0. \quad (\text{B.25})$$

Given that light vibrates with a frequency, a differentiation of Equation B.25 with respect to time can be calculated independently. It is described as

$$(\nabla^2 + k_0^2 n^2) \psi(r) = 0, \quad (\text{B.26})$$

where ψ , k , and n are a function of light, a wavenumber of the light in a vacuum, and the refractive index of the material, respectively. This form is called the "Helmholtz equation". Next, a spherical coordinate form of this equation is given by

$$\begin{aligned} \frac{1}{r^2} \frac{\partial}{\partial r} \left(r^2 \frac{\partial}{\partial r} \psi \right) + \frac{1}{r^2 \sin \theta} \frac{\partial}{\partial \theta} \left[\sin \theta \frac{\partial}{\partial \theta} \psi \right] \\ + \frac{1}{r^2 \sin^2 \theta} \frac{\partial^2}{\partial \phi^2} \psi + k_0^2 n^2 \psi = 0. \end{aligned} \quad (\text{B.27})$$

Here, considering a separation of variables such as $\psi(r, \theta, \phi) = \psi_r(r) \psi_\theta(\theta) \psi_\phi(\phi)$, the function is as follows:

$$\frac{r^2}{\psi_r(r) \psi_\theta(\theta) \psi_\phi(\phi)}, \quad (\text{B.28})$$

and multiplies both sides of Equation B.27.

$$\begin{aligned} \frac{1}{\psi_r(r)} \frac{\partial}{\partial r} \left(r^2 \frac{\partial}{\partial r} \psi_r(r) \right) + \frac{1}{\psi_\theta(\theta) \sin \theta} \frac{\partial}{\partial \theta} \left[\sin \theta \frac{\partial}{\partial \theta} \psi_\theta(\theta) \right] \\ + \frac{1}{\psi_\phi(\phi) \sin^2 \theta} \frac{\partial^2}{\partial \phi^2} \psi_\phi(\phi) + k_0^2 n^2 r^2 = 0. \end{aligned} \quad (\text{B.29})$$

Here, considering the independent variable ϕ , a relationship is derived as

$$\frac{1}{\psi_\phi(\phi)} \frac{\partial^2}{\partial \phi^2} \psi_\phi(\phi) = \text{const..} \quad (\text{B.30})$$

Therefore, a constant m as follows:

$$\frac{1}{\psi_\phi(\phi)} \frac{\partial^2}{\partial \phi^2} \psi_\phi(\phi) = -m^2. \quad (\text{B.31})$$

can be set. Next, considering θ as well, relationships are given by

$$\frac{1}{\psi_\theta(\theta) \sin \theta} \frac{\partial}{\partial \theta} \left[\sin \theta \frac{\partial}{\partial \theta} \psi_\theta(\theta) \right] - \frac{m^2}{\sin^2 \theta} = \text{const.}, \quad (\text{B.32})$$

$$\frac{1}{\psi_\theta(\theta) \sin \theta} \frac{\partial}{\partial \theta} \left[\sin \theta \frac{\partial}{\partial \theta} \psi_\theta(\theta) \right] - \frac{m^2}{\sin^2 \theta} = -l(l+1), \quad (\text{B.33})$$

where, l is a constant. A solution of Equation B.33 is the Legendre polynomial, as follows:

$$\psi_\theta(\theta) = P_l^m(\cos \theta). \quad (\text{B.34})$$

Since the angle components ϕ and θ can be merged, the form is called a "spherical harmonics", which is given by

$$Y_l^m(\theta, \phi) = p(l, m) \cdot P_l^m(\cos \theta) \cdot e^{im\phi}, \quad (\text{B.35})$$

where l , m , and p correspond polar quantum number and azimuthal quantum number, and a constant depending on l and m , respectively.

Next, the radial direction r is considered. With the equations given so far, Equation B.29 is transformed into

$$\frac{1}{\psi_r(r)} \frac{d}{dr} \left(r^2 \frac{d}{dr} \psi_r(r) \right) + k_0^2 n^2 r^2 - l(l+1) = 0, \quad (\text{B.36})$$

$$\frac{d}{dr} \left(r^2 \frac{d}{dr} \psi_r(r) \right) + [k_0^2 n^2 r^2 - l(l+1)] \psi_r(r) = 0, \quad (\text{B.37})$$

$$r^2 \frac{d^2}{dr^2} \psi_r(r) + 2r \frac{d}{dr} \psi_r(r) + [k_0^2 n^2 r^2 - l(l+1)] \psi_r(r) = 0, \quad (\text{B.38})$$

$$\frac{d^2}{dr^2} \psi_r(r) + \frac{2}{r} \frac{d}{dr} \psi_r(r) + [k_0^2 n^2 - \frac{l(l+1)}{r^2}] \psi_r(r) = 0. \quad (\text{B.39})$$

Here, the solution of Equation B.39 is a spherical Bessel function, as follows:

$$\psi_r(r) = j_l(kr). \quad (\text{B.40})$$

Given that a dielectric sphere with a radius of a is located in the air, the solutions for radial direction are described as

$$\begin{cases} A_l j_l(kr) & \cdots r \leq a, \\ B_l h_l(kr) & \cdots r > a, \end{cases} \quad (\text{B.41})$$

where $h_l(r)$ is a Hankel function. Since whispering gallery modes overlap the boundary between a dielectric material and the outside, conditions that satisfy the equation of continuity are required, as follows:

$$s \frac{\frac{\partial}{\partial x_r} [x_r j_l(n x_r)]}{j_l(n x_r)} \Big|_{r=a} = \frac{\frac{\partial}{\partial x_r} [x_r h_l(x_r)]}{h_l(x_r)} \Big|_{r=a}, s = \begin{cases} m & \text{for TE} \\ 1/m & \text{for TM} \end{cases}, \quad (\text{B.42})$$

where n is the refractive index of the material and $x_r = k_0 r$, k_0 is the wavenumber. From these relationships, transverse electric (TE) mode satisfies

$$n \frac{j_{l-1}(n x_a)}{j_l(n x_a)} = \frac{h_{l-1}(x_a)}{h_l(x_a)}, \quad (\text{B.43})$$

where $x_a = k_0 a$. In contrast, transverse magnetic (TM) mode follows

$$\frac{j_{l-1}(n x_a)}{j_l(n x_a)} = n \frac{h_{l-1}(x_a)}{h_l(x_a)} - \frac{n l}{x_a} + \frac{l}{n x_a}. \quad (\text{B.44})$$

These are the mathematical expressions of a whispering gallery mode. Figure 2.3 shows intensity mode profiles in the radial direction for a microsphere and azimuthal mode number $l = 280$ for the first three radial mode numbers ($r = 1, 2, 3$). Note that the high-order modes are more affected by the surface condition of the microsphere because the ratio of the evanescent field is higher than that for low-order modes, which causes larger surface scattering loss. Thus, the fundamental mode ($r = 1$) is usually the highest- Q mode in the cavity.

Whispering gallery modes have been analyzed as morphology-dependent resonance in the context of Mie scattering from the beginning^{146,147}. Using Mie scattering theory, the resonance frequency of a whispering gallery mode in a microsphere can be calculated as an asymptotic expansion as follows:

$$f_{n,l,m,p} = \frac{c}{2\pi n_{\text{out}} R} \left[\frac{l + \frac{1}{2}}{m} + \frac{t_n^0}{m} \left(\frac{l + \frac{1}{2}}{2} \right)^{\frac{1}{3}} + \frac{-p}{\sqrt{m^2 - 1}} + \left(\frac{l + \frac{1}{2}}{2} \right)^{-\frac{1}{3}} \frac{(t_n^0)^2}{20m} + O \left(\frac{l + \frac{1}{2}}{2} \right)^{-\frac{2}{3}} \right], \quad (\text{B.45})$$

where, n_{out} is the refractive index of the outside of a microsphere, $m = n_{\text{mat}}/n_{\text{out}}$,

R is the radius of a microsphere, l is the angular momentum, $p = 1$ for TE mode, $p = 1/m^2$ for TM mode, t_n^0 is the n_{th} root of Airy function. The number n indicates a radial mode, such as a first-order mode or a second-order mode. From the equations given so far, a profile of a whispering gallery mode can be expressed.

Appendix C

Derivation of Lugiato-Lefever equation

C.1 Nonlinear Schrödinger equation

Before developing a Lugiato-Lefever model to analyze the microcomb, I describe here a common numerical model for calculating the propagation of an optical pulse⁵¹). A split-step Fourier algorithm is also mentioned for solving a nonlinear Schrödinger equation numerically.

The propagation of light follows a wave equation:

$$\nabla^2 \tilde{E} + \epsilon(\omega)k_0^2 \tilde{E} = 0, \quad (\text{C.1})$$

where ϵ is a dielectric constant of a material with frequency dependence. This equation can be solved with separation of variables. A solution is assumed as

$$\tilde{E}(\mathbf{r}, \omega - \omega_0) = F(x, y) \tilde{A}(z, \omega - \omega_0) \exp(i\beta_0 z). \quad (\text{C.2})$$

$\tilde{A}(z, \omega)$ is a slowly varying function with z direction. $F(x, y)$ refers to a spatial distribution. β_0 is a propagation constant. With Equation C.2, Equation C.1 is divided into two parts as follows:

$$\frac{\partial^2 F}{\partial x^2} + \frac{\partial^2 F}{\partial y^2} + [\epsilon(\omega)k_0^2 - \tilde{\beta}^2]F = 0, \quad (\text{C.3})$$

$$2i\beta_0 \frac{\partial \tilde{A}}{\partial z} + (\tilde{\beta}^2 - \beta_0^2)\tilde{A} = 0, \quad (\text{C.4})$$

where Equation C.3 can be solved in the same manner as a common propagation in a fiber, as in Equation (2.79). A slowly varying envelope approximation is applied, which neglects $\frac{\partial^2 \tilde{A}}{\partial z^2}$ in Equation C.4. Next, a nonlinear term is implemented as follows:

$$\tilde{\beta}(\omega) = \beta(\omega) + \Delta\beta, \quad (\text{C.5})$$

where $\Delta\beta$ derives from a refractive index change $\Delta n = n_2|E|^2 + \frac{i\alpha}{2k_0}$, of which the real and imaginary parts mean nonlinearity and absorption loss, respectively. Considering an approximation described as

$$\tilde{\beta}^2 - \beta_0^2 \approx 2\beta_0(\tilde{\beta} - \beta_0), \quad (\text{C.6})$$

Equation C.4 is simplified to the following:

$$\frac{\partial \tilde{A}}{\partial z} = i[\beta(\omega) + \Delta\beta - \beta_0]\tilde{A}. \quad (\text{C.7})$$

$A(z, t)$ can be obtained from an inverse Fourier transformation of Equation C.7. To do that, $\beta(\omega)$ is expanded to a Taylor series around a carrier frequency ω as follows:

$$\beta(\omega) = \beta_0 + (\omega - \omega_0)\beta_1 + \frac{1}{2}(\omega - \omega_0)^2\beta_2 + \frac{1}{6}(\omega - \omega_0)^3\beta_3 + \dots, \quad (\text{C.8})$$

$$\beta_n = \left(\frac{d^n \beta}{d\omega^n} \right)_{\omega=\omega_0}. \quad (\text{C.9})$$

Although Taylor series mean an infinite sum of terms, high-order terms can generally be neglected. Here, the first, second, and third terms are considered.

$$\beta_1 = \frac{1}{c} \left[n + \omega \frac{dn}{d\omega} \right] = \frac{n_g}{c} = \frac{1}{v_g}, \quad (\text{C.10})$$

$$\beta_2 = \frac{d\beta_1}{d\omega} = \frac{1}{c} \left[2 \frac{dn}{d\omega} + \omega \frac{d^2n}{d\omega^2} \right] \approx \frac{\omega}{c} \frac{d^2n}{d\omega^2} \approx \frac{\lambda^3}{2\pi c^2} \frac{d^2n}{d\lambda^2}. \quad (\text{C.11})$$

With Equations C.10 and C.11, an inverse Fourier transformation of Equation C.7 is given by

$$\frac{\partial A}{\partial z} = -\beta_1 \frac{\partial A}{\partial t} - \frac{i}{2} \beta_2 \frac{\partial^2 A}{\partial t^2} + i\Delta\beta A. \quad (\text{C.12})$$

With the division of $\Delta\beta$ into a nonlinear term and a loss term, a general form of the propagation is derived as

$$\frac{\partial A}{\partial z} + \beta_1 \frac{\partial A}{\partial t} + \frac{i}{2} \beta_2 \frac{\partial^2 A}{\partial t^2} + \frac{\alpha}{2} A = i\gamma |A|^2 A, \quad (\text{C.13})$$

where α means propagation loss, γ is a nonlinear coefficient defined as

$$\gamma = \frac{n_2 \omega_0}{c A_{\text{eff}}}, \quad (\text{C.14})$$

and n_2 and A_{eff} are a nonlinear refractive index and an effective mode area, respectively. To further simplify, a frame of reference moving with the pulse at the group velocity v_g (called a retarded frame) is used as follows:

$$T = t - \frac{z}{v_g} = t - \beta_1 z. \quad (\text{C.15})$$

With Equation C.15, Equation C.13 is derived as

$$\frac{\partial A}{\partial z} + \frac{i}{2}\beta_2 \frac{\partial^2 A}{\partial T^2} + \frac{\alpha}{2}A = i\gamma|A|^2 A. \quad (\text{C.16})$$

$$\frac{\partial A}{\partial z} = -\frac{\alpha}{2}A - \frac{i}{2}\beta_2 \frac{\partial^2 A}{\partial T^2} + i\gamma|A|^2 A. \quad (\text{C.17})$$

Here, the first, second, and third terms in the right side indicate propagation loss, dispersion, and self-phase modulation, respectively. Note that the derived equation is a kind of nonlinear Schrödinger equation and, in general, cannot be solved analytically. Thus, to understand a pulse propagation with nonlinearity, a numerical analysis is often used. A number of calculation methods have been proposed. Among them, a split-step Fourier algorithm is reasonable with respect to calculation time, because it employs a fast Fourier transform (FFT) algorithm. A split-step algorithm divides Equation C.17 into two parts as follows:

$$\frac{\partial A}{\partial z} = (\hat{D} + \hat{N})A, \quad (\text{C.18})$$

where \hat{D} and \hat{N} indicate linear effects (loss and dispersion) and a nonlinear effect, respectively.

$$\hat{D} = -\frac{\alpha}{2} - \frac{i}{2}\beta_2 \frac{\partial^2}{\partial T^2}, \quad (\text{C.19})$$

$$\hat{N} = i\gamma|A|^2. \quad (\text{C.20})$$

Generally, linear and nonlinear effects occur simultaneously during a propaga-

tion. A split-step algorithm considers them to be independent and occurring alternately over a short distance h . Thus, a simple calculation has two steps. The first step considers only the nonlinear terms, so that \hat{D} is set to zero. The next step calculates only the linear terms, so that \hat{N} is set to zero. The expressions are given by

$$A(z+h, T) \approx \exp(h\hat{D})\exp(h\hat{N})A(z, T), \quad (\text{C.21})$$

where the exponential operator $\exp(h\hat{D})$ can be evaluated in the frequency domain as follows:

$$\exp(h\hat{D})B(z, T) = \{F^{-1}\exp[h\hat{D}(i\omega)]F\}B(z, t) \quad (\text{C.22})$$

where F denotes the Fourier-transform operation, $\hat{D}(i\omega)$ is obtained by replacing the differential operator $\partial/\partial T$ by $i\omega$, and ω is the angular frequency. In the frequency domain, $\hat{D}(i\omega)$ becomes constant, so that calculation time can be compressed using an FFT algorithm. Since the accuracy of the numerical simulation depends on a calculation step h , the calculation time becomes longer if a high accuracy is required. However, some improved calculation methods (symmetrized split-step⁵¹⁾, RKIP¹⁴⁸⁾, etc.) have been proposed, which require comparatively short calculation times.

C.2 Lugiato-Lefever equation

A derivation of a Lugiato-Lefever equation is described in this section. A Lugiato-Lefever equation can be calculated with a split-step Fourier algorithm, and it clearly describes the behavior of a nonlinear cavity.

A system for microcomb generation consists of a ring cavity and a waveguide providing energy to the ring cavity. First, an electric field E_z is described as

$$E_{z+dz} = E_z + \frac{dE}{dz} \cdot dz. \quad (\text{C.23})$$

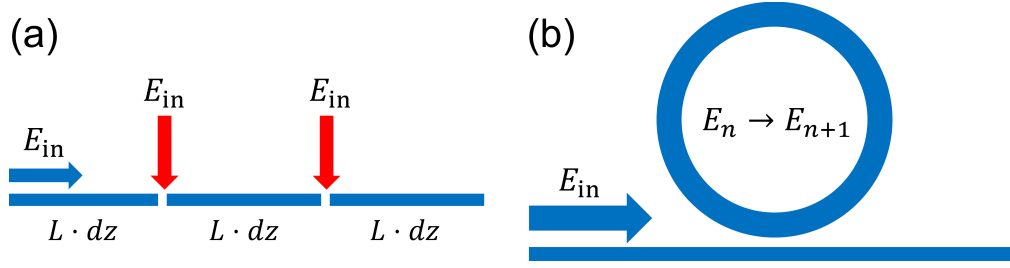


Fig. C.1: (a) Schematic image of calculation of a Lugiato-Lefever equation. (b) Schematic image of the relationship between a side coupling system and Lugiato-Lefever equation.

In a ring cavity, an electric field in the n_{th} round trip is considered in the same manner, as follows:

$$E^n = E^{n-1} + \frac{dE}{dz} \cdot L, \quad (C.24)$$

where n is a roundtrip number. When n increases by 1, it denotes a propagation around a cavity with length L . For a waveguide and a continuous-wave-driving field E_{in} , a relationship is given by

$$E^n = [E^{n-1} + \frac{dE}{dz} \cdot L] \sqrt{R} e^{-i\delta} + \sqrt{T} E_{in}, \quad (C.25)$$

where R is an intensity reflection coefficient from a cavity to a waveguide, and T is an intensity transmittance coefficient from the waveguide to the cavity. δ expresses the amount of phase shift that the field accumulates in a round trip. Thus, the phase of the driving field is a standard. The relationship between R and T is described as

$$R = 1 - T. \quad (C.26)$$

Given that T is very small (R is much higher), an approximation $\sqrt{R} = \sqrt{1 - T} \approx 1 - \frac{1}{2}T$ is adequate; it assumes that a ring cavity exhibits a high Q because R is nearly 1. In addition to this approximation, another approximation of $e^{-i\delta}$ is considered. When the phase shift δ is an integer multiplied by 2π , the phase shift

can be practically zero in the ring cavity. Thus, a deviation from the integer multiplied by 2π should be noted. With the assumption that the deviation is small, an approximation $e^{-i\delta} \approx 1 - i\delta$ is used. Using two approximations, Equation C.25 is derived as

$$E^n = [E^{n-1} + \frac{dE}{dz} \cdot L](1 - \frac{1}{2}T)(1 - i\delta) + \sqrt{T}E_{\text{in}}. \quad (\text{C.27})$$

Note that we can neglect the term of a small T multiplied by a small δ , so that Equation C.27 is simplified as follows:

$$E^n = [E^{n-1} + \frac{dE}{dz} \cdot L](1 - \frac{1}{2}T - i\delta) + \sqrt{T}E_{\text{in}}. \quad (\text{C.28})$$

Here, with the assumption that a change in propagation during a round is small, the further simplified form is derived as

$$E^n = E^{n-1}(1 - \frac{1}{2}T - i\delta) + \frac{dE}{dz} \cdot L + \sqrt{T}E_{\text{in}}. \quad (\text{C.29})$$

With Equations C.17 and C.29, a Lugiato-Lefever equation is derived as

$$E^n - E^{n-1} = (-\frac{\alpha L}{2} - \frac{T}{2} - i\delta - \frac{i}{2}\beta_2 L \frac{\partial^2}{\partial T^2} + i\gamma L |E|^2)E + \sqrt{T}E_{\text{in}}. \quad (\text{C.30})$$

Considering the relationship of a round trip time t_R and a cavity length L , the form $E(n, \tau)$, in which τ is a short time, is expressed as follows:

$$t_R \frac{\partial E(n, \tau)}{\partial n} = (-\frac{\alpha L}{2} - \frac{T}{2} - i\delta - \frac{i}{2}\beta_2 L \frac{\partial^2}{\partial \tau^2} + i\gamma L |E|^2)E + \sqrt{T}E_{\text{in}}. \quad (\text{C.31})$$

Here, only second-order dispersion is considered. The expression that includes higher-order dispersion is given by

$$t_R \frac{\partial E(n, \tau)}{\partial n} = \left(-\frac{\alpha L}{2} - \frac{T}{2} - i\delta + iL \sum_{k \geq 2} \frac{\beta_k}{k} \left(-i \frac{\partial}{\partial \tau} \right)^k + i\gamma L |E|^2 \right) E + \sqrt{T} E_{\text{in}}. \quad (\text{C.32})$$

With a Lugiato-Lefever equation, nonlinear dynamics in a fiber ring cavity has been studied at the beginning. In 2013, Coen *et al.*⁶⁰⁾ proposed that the equation could be applied to microcomb generation in a nonlinear microcavity. On the other hand, spatial soliton research has also employed the same equation¹⁴⁹⁾. In the context of spatial solitons, the dispersion and self-phase modulation terms correspond to the diffraction and self-focusing effects in space.

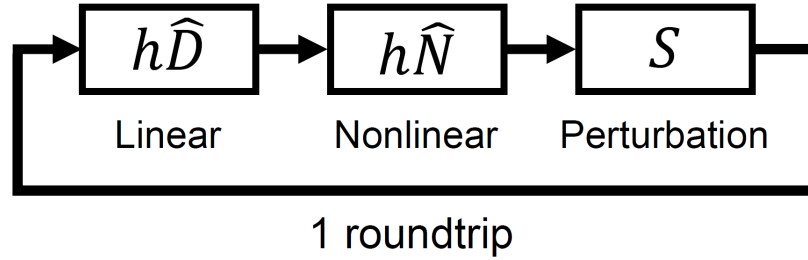


Fig. C.2: Split-step calculation for a Lugiato-Lefever equation.

謝辞 Acknowledgement

本研究は、慶應義塾大学工学部電子工学科准教授 田邊孝純博士のご指導のもとで行われました。本研究を遂行するにあたり筆者に研究の場を与えてくださり、研究の全体を通じて貴重な助言をして頂いた田邊孝純博士に心から感謝の意を表します。筆者は研究室の第1期生ということもあり、研究環境の構築、研究テーマの考案、研究の進め方、発表の仕方など研究生活に関わるほぼ全ての事柄を博士から学ばせて頂きました。常日頃より、直感的に、物理的に物事をとらえる姿勢は、筆者にも根付いていると考えています。また、研究室内、学内に留まらず、外部の研究会で発表する機会、海外へ留学する機会、に恵まれたのは、ひとえに博士のご理解と多大なご尽力に他なりません。筆者が、博士課程を修了するに至ったのは、田邊孝純博士のご支援あってこそだと考えます。本研究を通じて学び経験した事は筆者のこれからの人生において大きな財産です。

本論文を執筆するにあたり粗筆を丁寧に見て頂き、本論文を査読して頂いた、慶應義塾大学工学部物理学科教授 佐々田博之博士、同大学工学部電子工学科教授 神成文彦博士、同大学工学部電子工学科教授 津田裕之博士には心から感謝致します。佐々田博之博士には、光物理の理論的な視点から本研究を見て頂き、筆者の見落とししていた点を、十分に指摘して頂きました。ディスカッションを通じて筆者は新たなことを学ぶことができました。神成文彦博士には、本研究を開始した当初から多くの貴重な知識を与えて頂きました。本研究の内容に対しても、明快なご指摘を頂きました。研究外でお会いすることも多く、博士の柔軟に物事に取り組む姿勢をたびたび拝見し、学ばせて頂きました。津田裕之博士には、光通信応用の観点から本研究を見て頂きました。微小光共振器を研究している中で、物理的には興味深いですが、実用的にはどうなのか、と疑問を持つことがしばしばありましたが、博士とのディスカッションを通じて、その懸念は氷塊しました。心から感謝申し上げます。 I greatly appreciate Prof. Marko Lončar (Distinguished Visiting Professor, Tiant sai Lin Professor of Electrical Engineering, School of En-

Acknowledgement

gineering and Applied Science, Harvard University) who joined the committee of my defense. He gave me a lot of valuable advice about hysteresis behavior of microcavities, the gain competition between FWM and SRS, and phase-matching for third-harmonic generation.

さらに、筆者は共同研究を通じて研究の幅を広げることができました。明治大学研究・知財戦略機構特任講師 宮路智行博士には、Lugiato-Lefever 方程式の理論的な面をサポートして頂きました。筆者が、LL 方程式に関する理論の理解に苦しんでいた時、インターネット上でお名前を見つけ、連絡を取らせて頂いたのが、共同研究のきっかけでした。定期的にディスカッションの機会を頂き、筆者の拙い理解を、いつも正して頂きました。論文を投稿する際にも、ご厚意で査読して頂き、数式の間違いを指摘して頂いた事など感謝以外の言葉がありません。

研究室に配属されて以来、同輩、後輩とかけがえのない友人に恵まれました。第1期生であるため先輩がいないのが残念に思われますが、それを補って余りある関係を築くことができました。同輩である吉岐航氏（慶應義塾大学理工学研究科後期博士課程）、小川陽平氏（OKI データ）、工藤寛史氏には心より感謝致します。吉岐航氏は、数少ない後期博士課程の友人であり、博士課程教育リーディングプログラム（オールラウンド型）でも同期として、多くの時間を共有しました。氏の研究に取り組む姿勢は素晴らしく、多くを見習わせて頂きました。筆者にとって、常に先導してくれる氏は、後期博士課程の長い道のを明るく照らしてくれる存在でした。小川陽平氏には、多くの事を学ばせて頂きました。FDTD 法のプログラムのベースとなる設定を教えて頂くなど、当時コンピュータ周りに疎かった筆者は、多くの点で氏のお世話になりました。工藤寛史氏には、粘り強く研究に取り組む姿勢、オンオフをしっかりと分けてメリハリのある生活を送る姿勢など、多くの事を学ばせて頂きました。2013年に国際学会の発表のためアメリカのロチェスターと一緒にいき、楽しく過ごしたことを鮮明に覚えています。第1期生として、実験装置も何もない所からスタートし、右も左も分からないながらも充実して過ごせてくれたのは、3人のおかげです。またその他の電子工学科ならびにリーディングプログラムの同輩にも心より感謝致します。筆者が後期博士課程を進んでくれたのは、多くの友人の助言やサポートのおかげです。

研究室の後期博士課程の後輩である、鈴木良氏（慶應義塾大学理工学研究科後期博士課程）、鐵本智大氏（慶應義塾大学理工学研究科後期博士課程）、Nurul Ashikin Binti Daud さん（慶應義塾大学理工学研究科後期博士課程）には心より感謝致します。鈴木良氏は、同じ研究班で取り組む仲間であり、研究に関して最も

多くの時間を共有させて頂きました。氏からは、丁寧に実験をおこなう姿勢、不明な点をそのままにしない姿勢などを見習わせて頂きました。氏の適格な発言は、いつも筆者の不足している部分を補ってくれました。筆者にとって、氏は筆者が困っている時にふとサポートしてくれるかけがえのない存在でした。鐵本智大氏には、ファブリケーションを中心にして、多くの事を学ばせて頂きました。氏の何にでも興味を持って取り組む姿勢は、いつも見習っていました。Nurul Ashikin Binti Daudさんは、研究室唯一のEnglish speakerであり、発表の時の言い回しなどを見習わせて頂いておりました。

同じ研究班として過ごした、小畠知也氏（東芝）、陣内哲倫氏（東芝）、岡部悠介氏（慶應義塾大学理工学研究科前期博士課程）、長野拓真氏（慶應義塾大学理工学研究科前期博士課程）、藤井瞬氏（慶應義塾大学理工学研究科前期博士課程）、堀敦裕氏（慶應義塾大学理工学研究科前期博士課程）、久保田啓寛氏（慶應義塾大学理工学部学士課程）には心より感謝致します。半学半教の言葉があるように、後輩から多くの事を学ばせて頂きました。小畠知也氏とは、シミュレーションを共に研究させて頂きました。氏はプログラムの構築が早く、研究の提案をするとすぐに実装し結果を持ってきてくれました。本研究のChapter 5は彼が基礎となるアルゴリズムを構築したシミュレーションを含んでおり、彼の貢献は非常に大きいものです。陣内哲倫氏とは、実験を共に研究させて頂きました。氏はとにかく行動力があり、養生テープやUV硬化剤を駆使して自前の実験器具を作るなど、筆者には信じ難いことが多くありました。しかし、氏の行動や発言が思いもよらぬ結果を引き寄せることを目撃し、筆者は氏から多くを学ばせて頂きました。Chapter 6の実験系は彼の発案によるものであり、その貢献は大きいものです。岡部悠介氏、長野拓真氏は、研究のディスカッションを通じて、筆者の理解を高めてくれました。筆者の想定していない観点に気付かせてくれたことに感謝致します。藤井瞬氏には、最後の1年間、研究室内外で大変お世話になりました。氏は、修士課程の学生とは思えないほどの深い知識と高い行動力を兼ね備えており、筆者もときに圧倒されることがありました。Chapter 6の実験は、氏と共にデータを取得したものであり、実験室の照明を消した状態の長い実験を耐えられたのは氏のおかげです。堀敦裕氏とは、シミュレーションを共に研究させて頂きました。氏は無駄のないアルゴリズムを作る能力が高く、計算時間の大幅な削減に貢献してくれました。公聴会などの博士論文審査の際には、多くの支援を頂いたこと感謝致します。久保田啓寛氏には、日々ひたむきに実験する姿勢を学ばせて頂きました。研究をスタートした5年前の初心を思い出させてくれまし

Acknowledgement

た。またその他の後輩にも感謝致します。皆さんのおかげで楽しく、充実した研究生生活を送ることができました。

筆者は2014年2~3月に、カナダのINRS (Institut national de la recherche scientifique)に留学する機会に恵まれました。モントリオールに位置する大学院大学であり、Prof. Roberto Morandottiグループに滞在し、初めての国外滞在ということで多くの貴重な体験をさせて頂きました。Chapter 3の内容は、Dr. Michael Kuesとのディスカッションから得られた気づきも含まれております。心より感謝致します。本滞在は、リーディングプログラムの援助の基に実現しました。プログラムのコーディネータである神成文彦博士には重ね重ね感謝致します。I appreciate Prof. Roberto Morandotti (INRS) who accepted me as a research intern. I stayed from February to March in 2014. I'd like to thank Dr. Michael Kues and Mr. Christian Reimer for supervising and collaborating with me. I learned a lot about hydex-glass microring resonators.

また、筆者は2016年1~4月に、アメリカのHarvard大学に留学する機会にも恵まれました。副査にも入って頂いたProf. Marko Lončarグループに滞在し、ファブリケーションを中心に貴重な体験をさせて頂きました。また留学するにあたって、北翔太博士 (Shota Kita, NTT物性科学基礎研究所)には、多大なご支援を頂きました。博士はLončarグループに長い間滞在されており、その現地の実情を事細かに教えて頂きました。心より感謝致します。本滞在もまた、リーディングプログラムの援助の基に実現しました。重ね重ね感謝致します。I appreciate Prof. Marko Lončar (Harvard University) who accepted me as a short-term scholar. I stayed from January to April in 2016. I'd like to thank Dr. Stefan Kalchmair for supervising me. He educated me many things about not only silicon-on-sapphire microrings but also Boston life. I remember that he spent much time in educating me in cleanroom. I also thank Dr. Vivek Venkataraman, Dr. Boris Desiatov, Mr. Pawel Latawiec, and Mr. Cheng Wang for discussing comb generation with me. I was deeply impressed by them because of their intelligence and open-mind. I'm grateful to Mr. Zin Lin, Mr. Young Ik Sohn, and Mr. Linbo Shao for their kindness. I appreciate Dr. Janise Alomar who was my roommate in Boston. I remember that she cooked me many times and she talked to me every day. Thanks to her, I lived a happy Boston life.

筆者は、2012年4月より、慶應義塾大学の博士課程教育リーディングプログラム (オールラウンド型) のRAでありました。関係各位に感謝申し上げます。プロ

Acknowledgement

グラムの一環として、2015年度は慶應義塾大学医学研究科医科学専攻に所属し、眼科学教室にて生物学の一端を経験致しました。チタンサファイアレーザを用いた網膜のイメージングの研究は、生物学だけでなく光物理の理解を深める上でもとても貴重な体験となりました。慶應義塾大学医学部眼科学教室教授 坪田一男博士ならびに理化学研究所光量子工学研究領域光量子制御技術開発チーム 和田智之博士に心より感謝致します。

最後に本研究を遂行するにあたり、理解を示して頂いた家族に感謝致します。大学院の5年間を不自由なく過ごしてこれたのは、家族の支援があったからに他なりません。本研究の完成は、両親に捧げたいと思います。ここまで支えて頂いたことに心より感謝致します。

2017年2月2日

加藤拓巳

List of achievements

Publications (related to thesis)

1. T. Kato, A. Hori, R. Suzuki, S. Fujii, T. Kobatake, and T. Tanabe, “Transverse mode interaction via stimulated Raman scattering comb in a silica microcavity,” *Optics Express* **25**, 857-866 (2017).
2. T. Kato, A. C.-Jinnai, T. Nagano, T. Kobatake, R. Suzuki, W. Yoshiki, and T. Tanabe, “Hysteresis behavior of Kerr frequency comb generation in a high-quality-factor whispering gallery mode microcavity,” *Japanese Journal of Applied Physics* **55**, 072201 (5 pages) (2016).
3. 加藤拓巳, 陣内哲倫, 小島知也, 田邊孝純, 「シリカトロイド微小光共振器を用いたモード同期マイクロコム発生とその理論検討」, *レーザー研究* **44**, 532-536 (2016).
4. A. C.-Jinnai, T. Kato, S. Fujii, T. Nagano, T. Kobatake, and T. Tanabe, “Broad bandwidth third-harmonic generation via four-wave mixing and stimulated Raman scattering in a microcavity,” *Optics Express* **24**, 26322-26331 (2016).

Other publications

1. Y. Nakagawa, Y. Mizumoto, T. Kato, T. Kobatake, H. Itobe, Y. Kakinuma, and T. Tanabe, “Dispersion tailoring of a crystalline whispering gallery mode microcavity for a wide-spanning optical Kerr frequency comb,” *Journal of Optical Society of America B* **33**, 1913-2920 (2016).
2. T. Kobatake, T. Kato, H. Itobe, Y. Nakagawa, and T. Tanabe, “Thermal effects on Kerr comb generation in a CaF₂ whispering gallery mode microcavity,” *IEEE Photonics Journal* **8**, 4501109 (2016).
3. R. Suzuki, T. Kato, T. Tetsumoto, and T. Tanabe, “Octagonal toroid microcavity for mechanically robust optical coupling,” *AIP Advances* **5**, 057127 (2015).
4. H. Kudo, Y. Ogawa, T. Kato, A. Yokoo, and T. Tanabe, “Fabrication of whispering gallery mode cavity using crystal growth,” *Applied Physics Letters* **102**, 211105 (2013).
5. T. Kato, W. Yoshiki, R. Suzuki, and T. Tanabe, “Octagonal silica toroidal microcavity for controlled optical coupling,” *Applied Physics Letters* **101**, 121101 (2012).

Presentations (international conferences)

1. T. Kato*, A. C. Jinnai, S. Fujii, and T. Tanabe, “Broadband visible comb generation via third harmonic generation assisted by stimulated Raman scattering,” the conference on Laser Electro-Optics:2016, STu4Q.2, San Jose, June 5-10 (2016).
2. T. Kato*, T. Kobatake, R. Suzuki, and T. Tanabe, “Analysis of effect of interaction between transverse modes on Kerr frequency comb generation,” the conference on Laser Electro-Optics:2016, JTU5A.48, San Jose, June 5-10 (2016).
3. T. Kato*, T. Kobatake, Z. Chen, R. Suzuki, and T. Tanabe, “Influence of Raman scattering on Kerr frequency comb in a silica toroidal microcavity,” *Frontiers in Optics/Laser Science Conference (FiO/LS)*, FTu2E.4, San Jose, October 18-22 (2015).

List of achievements

4. T. Kato*, R. Suzuki, T. Kobatake, and T. Tanabe, "Analysis and experiments on harmonic mode locking in an optical microcavity," the conference on Laser Electro-Optics:2014, SM1M.7, San Jose, June 6-13 (2014).
5. T. Kato*, R. Suzuki, and T. Tanabe, "Analysis of Various Whispering Gallery Modes in an Octagonal Silica Toroidal Microcavity," The 10th Conference on Lasers and Electro-Optics Pacific Rim (CLEO-PR & OECC/PS), TuPM-12, Kyoto, June 30-July 4 (2013).
6. T. Kato*, W. Yoshiki, Y. Ogawa, and T. Tanabe, "Polygonal silica toroidal microcavity for easy and stable coupling with waveguides," Frontiers in Optics/Laser Science XXVIII meeting (FiO/LS), FTu4A.5, Rochester, October 14-18 (2012).

Presentations (Domestic conferences)

1. 加藤拓巳, 陣内哲倫*, 小島知也, 田邊孝純, 「シリカトロイド共振器におけるカスケードラマン散乱による広帯域マイクロコム」レーザー学会学術講演会第36回年次大会, 11aE6-6, 名城大学天白キャンパス, 平成28年1月9日~11日
2. 加藤拓巳*, 小島知也, 陣内哲倫, 長野拓真, 田邊孝純, 「シリカトロイド共振器の光カーコム発生におけるラマン散乱の影響」第76回応用物理学会秋季学術講演会, 13p-2G-15, 名古屋国際会議場, 平成27年9月13日~16日
3. 加藤拓巳, 小島知也, 鈴木良, 田邊孝純*, 「微小光共振器における光カーコムの高調波モード同期制御」第75回応用物理学会秋季学術講演会, 20a-C2-6, 北海道大学札幌キャンパス, 平成26年9月17日~20日.
4. 加藤拓巳*, 鈴木良, 小島知也, 田邊孝純, 「微小光共振器光カーコム-超高繰り返し光パルス列の繰り返し周波数の能動制御」レーザー学会創立40周年記念学術講演会第34回年次大会, 21aVII-2, 北九州国際会議場, 平成26年1月20日~22日.

Bibliography

- [1] K. J. Vahala, "Optical microcavities," *Nature* **424**, 839–846 (2003).
- [2] A. A. Savchenkov, A. B. Matsko, D. Strekalov, M. Mohageg, V. S. Ilchenko, and L. Maleki, "Low threshold optical oscillations in a whispering gallery mode CaF₂ resonator," *Physical Review Letters* **93**, 243905 (2004).
- [3] T. Kippenberg, S. Spillane, and K. Vahala, "Kerr-nonlinearity optical parametric oscillation in an ultrahigh-*Q* toroid microcavity," *Physical Review Letters* **93**, 083904 (2004).
- [4] H. Rong, R. Jones, A. Liu, O. Cohen, D. Hak, A. Fang, and M. Paniccia, "A continuous-wave Raman silicon laser," *Nature* **433**, 725–728 (2005).
- [5] T. J. Kippenberg, S. M. Spillane, B. Min, and K. J. Vahala, "Theoretical and experimental study of stimulated and cascaded Raman scattering in ultrahigh-*Q* optical microcavities," *IEEE Journal of Selected Topics in Quantum Electronics* **10**, 1219–1228 (2004).
- [6] I. S. Grudinin and L. Maleki, "Ultralow-threshold Raman lasing with CaF₂ resonators," *Optics Letters* **32**, 166–168 (2007).
- [7] S. Spillane, T. Kippenberg, and K. Vahala, "Ultralow-threshold Raman laser using a spherical dielectric microcavity," *Nature* **415**, 621–623 (2002).
- [8] B. Corcoran, C. Monat, C. Grillet, D. J. Moss, B. J. Eggleton, T. White, L. O'Faolain, and T. F. Krauss, "Green light emission in silicon through slow-light enhanced third-harmonic generation in photonic-crystal waveguides," *Nature Photonics* **3**, 206–210 (2009).
- [9] T. Carmon and K. J. Vahala, "Visible continuous emission from a silica microphotonic device by third-harmonic generation," *Nature Physics* **3**, 430–435 (2007).
- [10] P. Del'Haye, A. Schliesser, O. Arcizet, T. Wilken, R. Holzwarth, and T. J. Kippenberg, "Optical frequency comb generation from a monolithic microresonator," *Nature* **450**, 1214–1217 (2007).
- [11] T. J. Kippenberg, R. Holzwarth, and S. Diddams, "Microresonator-based optical frequency combs," *Science* **332**, 555–559 (2011).
- [12] T. Udem, R. Holzwarth, and T. W. Hänsch, "Optical frequency metrology," *Nature* **416**, 233–237 (2002).
- [13] N. R. Newbury, "Searching for applications with a fine-tooth comb," *Nature Photonics* **5**, 186–188 (2011).
- [14] F. Tauser, A. Leitenstorfer, and W. Zinth, "Amplified femtosecond pulses from an Er: fiber system: Nonlinear pulse shortening and selfreferencing detection of the carrier-envelope phase evolution," *Optics Express* **11**, 594–600 (2003).
- [15] F.-L. Hong, K. Minoshima, A. Onae, H. Inaba, H. Takada, A. Hirai, H. Matsumoto, T. Sugiura, and M. Yoshida, "Broad-spectrum frequency comb generation and carrier-envelope offset frequency measurement by second-harmonic generation of a mode-locked fiber laser," *Optics Letters* **28**, 1516–1518 (2003).

Bibliography

- [16] B. R. Washburn, S. A. Diddams, N. R. Newbury, J. W. Nicholson, M. F. Yan, and C. G. Jørgensen, “Phase-locked, erbium-fiber-laser-based frequency comb in the near infrared,” *Optics Letters* **29**, 250–252 (2004).
- [17] T. Herr, V. Brasch, J. Jost, C. Wang, N. Kondratiev, M. Gorodetsky, and T. Kippenberg, “Temporal solitons in optical microresonators,” *Nature Photonics* **8**, 145–152 (2014).
- [18] P. Del’Haye, O. Arcizet, A. Schliesser, R. Holzwarth, and T. J. Kippenberg, “Full stabilization of a microresonator-based optical frequency comb,” *Physical Review Letters* **101**, 053903 (2008).
- [19] T. Herr, K. Hartinger, J. Riemensberger, C. Wang, E. Gavartin, R. Holzwarth, M. Gorodetsky, and T. Kippenberg, “Universal formation dynamics and noise of Kerr-frequency combs in microresonators,” *Nature Photonics* **6**, 480–487 (2012).
- [20] M. Ferrera, L. Razzari, D. Duchesne, R. Morandotti, Z. Yang, M. Liscidini, J. Sipe, S. Chu, B. Little, and D. Moss, “Low-power continuous-wave nonlinear optics in doped silica glass integrated waveguide structures,” *Nature Photonics* **2**, 737–740 (2008).
- [21] J. S. Levy, A. Gondarenko, M. A. Foster, A. C. Turner-Foster, A. L. Gaeta, and M. Lipson, “CMOS-compatible multiple-wavelength oscillator for on-chip optical interconnects,” *Nature Photonics* **4**, 37–40 (2010).
- [22] B. Hausmann, I. Bulu, V. Venkataraman, P. Deotare, and M. Lončar, “Diamond nonlinear photonics,” *Nature Photonics* **8**, 369–374 (2014).
- [23] A. G. Griffith, R. K. Lau, J. Cardenas, Y. Okawachi, A. Mohanty, R. Fain, Y. H. D. Lee, M. Yu, C. T. Phare, C. B. Poitras, A. Gaeta, and M. Lipson, “Silicon-chip mid-infrared frequency comb generation,” *Nature Communications* **6**, 6299 (2015).
- [24] C. Y. Wang, T. Herr, P. Del’Haye, A. Schliesser, J. Hofer, R. Holzwarth, T. Hänsch, N. Picqué, and T. J. Kippenberg, “Mid-infrared optical frequency combs at 2.5 μm based on crystalline microresonators,” *Nature Communications* **4**, 1345 (2013).
- [25] J. Pfeifle, V. Brasch, M. Laueremann, Y. Yu, D. Wegner, T. Herr, K. Hartinger, P. Schindler, J. Li, D. Hillerkuss, R. Schmogrow, C. Weimann, R. Holzwarth, W. Freude, J. Leuthold, T. J. Kippenberg, and C. Koos, “Coherent terabit communications with microresonator Kerr frequency combs,” *Nature Photonics* **8**, 375–380 (2014).
- [26] X. Xue, Y. Xuan, H.-J. Kim, J. Wang, D. E. Leaird, M. Qi, and A. M. Weiner, “Programmable single-bandpass photonic RF filter based on Kerr comb from a microring,” *Journal of Light-wave Technology* **32**, 3557–3565 (2014).
- [27] C. Hood, T. Lynn, A. Doherty, A. Parkins, and H. Kimble, “The atom-cavity microscope: Single atoms bound in orbit by single photons,” *Science* **287**, 1447–1453 (2000).
- [28] D. Hunger, T. Steinmetz, Y. Colombe, C. Deutsch, T. W. Hänsch, and J. Reichel, “A fiber Fabry–Perot cavity with high finesse,” *New Journal of Physics* **12**, 065038 (2010).
- [29] J. Gerard, D. Barrier, J. Marzin, R. Kuszelewicz, L. Manin, E. Costard, V. Thierry-Mieg, and T. Rivera, “Quantum boxes as active probes for photonic microstructures: The pillar microcavity case,” *Applied Physics Letters* **69**, 449–451 (1996).
- [30] M. Pelton, C. Santori, J. Vučković, B. Zhang, G. S. Solomon, J. Plant, and Y. Yamamoto, “Efficient source of single photons: a single quantum dot in a micropost microcavity,” *Physical Review Letters* **89**, 233602 (2002).
- [31] J. Foresi, P. R. Villeneuve, J. Ferrera, E. Thoen, G. Steinmeyer, S. Fan, J. Joannopoulos, L. Kimerling, H. I. Smith, and E. Ippen, “Photonic-bandgap microcavities in optical waveguides,” *Nature* **390**, 143–145 (1997).
- [32] O. Painter, R. Lee, A. Scherer, A. Yariv, J. O’Brien, P. Dapkus, and I. Kim, “Two-dimensional photonic band-gap defect mode laser,” *Science* **284**, 1819–1821 (1999).

-
- [33] Y. Akahane, T. Asano, B.-S. Song, and S. Noda, "High- Q photonic nanocavity in a two-dimensional photonic crystal," *Nature* **425**, 944–947 (2003).
- [34] T. Tanabe, M. Notomi, E. Kuramochi, A. Shinya, and H. Taniyama, "Trapping and delaying photons for one nanosecond in an ultrasmall high- Q photonic-crystal nanocavity," *Nature Photonics* **1**, 49–52 (2007).
- [35] Y. Ooka, T. Tetsumoto, A. Fushimi, W. Yoshiki, and T. Tanabe, "CMOS compatible high- Q photonic crystal nanocavity fabricated with photolithography on silicon photonic platform," *Scientific reports* **5**, 11312 (2015).
- [36] Q. Xu, S. Manipatruni, B. Schmidt, J. Shakya, and M. Lipson, "12.5 Gbit/s carrier-injection-based silicon micro-ring silicon modulators," *Optics Express* **15**, 430–436 (2007).
- [37] W. Bogaerts, P. De Heyn, T. Van Vaerenbergh, K. De Vos, S. Kumar Selvaraja, T. Claes, P. Dumon, P. Bienstman, D. Van Thourhout, and R. Baets, "Silicon microring resonators," *Laser & Photonics Reviews* **6**, 47–73 (2012).
- [38] D. J. Moss, R. Morandotti, A. L. Gaeta, and M. Lipson, "New CMOS-compatible platforms based on silicon nitride and Hydex for nonlinear optics," *Nature Photonics* **7**, 597–607 (2013).
- [39] A. Gondarenko, J. S. Levy, and M. Lipson, "High confinement micron-scale silicon nitride high Q ring resonator," *Optics Express* **17**, 11366–11370 (2009).
- [40] I. Goykhman, B. Desiatov, and U. Levy, "Ultrathin silicon nitride microring resonator for biophotonic applications at 970 nm wavelength," *Applied Physics Letters* **97**, 081108 (2010).
- [41] C. Xiong, W. H. Pernice, X. Sun, C. Schuck, K. Y. Fong, and H. X. Tang, "Aluminum nitride as a new material for chip-scale optomechanics and nonlinear optics," *New Journal of Physics* **14**, 095014 (2012).
- [42] L. Rayleigh, "CXII. The problem of the whispering gallery," *The London, Edinburgh, and Dublin Philosophical Magazine and Journal of Science* **20**, 1001–1004 (1910).
- [43] R. Richtmyer, "Dielectric resonators," *Journal of Applied Physics* **10**, 391–398 (1939).
- [44] V. Braginsky, M. Gorodetsky, and V. Ilchenko, "Quality-factor and nonlinear properties of optical whispering-gallery modes," *Physics Letters A* **137**, 393–397 (1989).
- [45] A. Matsko, A. Savchenkov, D. Strekalov, V. Ilchenko, and L. Maleki, "Review of applications of whispering-gallery mode resonators in photonics and nonlinear optics," *IPN Progress Report* **42**, 162 (2005).
- [46] W. Liang, A. Savchenkov, A. Matsko, V. Ilchenko, D. Seidel, and L. Maleki, "Generation of near-infrared frequency combs from a MgF_2 whispering gallery mode resonator," *Optics Letters* **36**, 2290–2292 (2011).
- [47] D. Armani, T. Kippenberg, S. Spillane, and K. Vahala, "Ultra-high- Q toroid microcavity on a chip," *Nature* **421**, 925–928 (2003).
- [48] T. Kippenberg, S. Spillane, and K. Vahala, "Demonstration of ultra-high- Q small mode volume toroid microcavities on a chip," *Applied Physics Letters* **85**, 6113–6115 (2004).
- [49] S. A. Diddams, D. J. Jones, J. Ye, S. T. Cundiff, J. L. Hall, J. K. Ranka, R. S. Windeler, R. Holzwarth, T. Udem, and T. Hänsch, "Direct link between microwave and optical frequencies with a 300 THz femtosecond laser comb," *Physical Review Letters* **84**, 5102 (2000).
- [50] R. Holzwarth, T. Udem, T. W. Hänsch, J. Knight, W. Wadsworth, and P. S. J. Russell, "Optical frequency synthesizer for precision spectroscopy," *Physical Review Letters* **85**, 2264 (2000).
- [51] G. P. Agrawal, *Nonlinear Fiber Optics* (Academic, 2007).

Bibliography

- [52] P. Del’Haye, T. Herr, E. Gavartin, M. Gorodetsky, R. Holzwarth, and T. J. Kippenberg, “Octave spanning tunable frequency comb from a microresonator,” *Physical Review Letters* **107**, 063901 (2011).
- [53] I. H. Agha, Y. Okawachi, M. A. Foster, J. E. Sharping, and A. L. Gaeta, “Four-wave-mixing parametric oscillations in dispersion-compensated high- Q silica microspheres,” *Physical Review A* **76**, 043837 (2007).
- [54] I. H. Agha, Y. Okawachi, and A. L. Gaeta, “Theoretical and experimental investigation of broadband cascaded four-wave mixing in high- Q microspheres,” *Optics Express* **17**, 16209–16215 (2009).
- [55] Y. Okawachi, K. Saha, J. S. Levy, Y. H. Wen, M. Lipson, and A. L. Gaeta, “Octave-spanning frequency comb generation in a silicon nitride chip,” *Optics Letters* **36**, 3398–3400 (2011).
- [56] M. Peccianti, A. Pasquazi, Y. Park, B. Little, S. T. Chu, D. Moss, and R. Morandotti, “Demonstration of a stable ultrafast laser based on a nonlinear microcavity,” *Nature Communications* **3**, 765 (2012).
- [57] M. Pu, L. Ottaviano, E. Semenova, and K. Yvind, “Efficient frequency comb generation in AlGaAs-on-insulator,” *Optica* **3**, 823–826 (2016).
- [58] F. Ferdous, H. Miao, D. E. Leaird, K. Srinivasan, J. Wang, L. Chen, L. T. Varghese, and A. M. Weiner, “Spectral line-by-line pulse shaping of on-chip microresonator frequency combs,” *Nature Photonics* **5**, 770–776 (2011).
- [59] A. Matsko, A. Savchenkov, W. Liang, V. Ilchenko, D. Seidel, and L. Maleki, “Mode-locked Kerr frequency combs,” *Optics Letters* **36**, 2845–2847 (2011).
- [60] S. Coen, H. G. Randle, T. Sylvestre, and M. Erkintalo, “Modeling of octave-spanning Kerr frequency combs using a generalized mean-field Lugiato–Lefever model,” *Optics Letters* **38**, 37–39 (2013).
- [61] M. R. Lamont, Y. Okawachi, and A. L. Gaeta, “Route to stabilized ultrabroadband microresonator-based frequency combs,” *Optics Letters* **38**, 3478–3481 (2013).
- [62] T. Hansson, D. Modotto, and S. Wabnitz, “Dynamics of the modulational instability in microresonator frequency combs,” *Physical Review A* **88**, 023819 (2013).
- [63] Y. K. Chembo and C. R. Menyuk, “Spatiotemporal Lugiato-Lefever formalism for Kerr-comb generation in whispering-gallery-mode resonators,” *Physical Review A* **87**, 053852 (2013).
- [64] T. Carmon, L. Yang, and K. Vahala, “Dynamical thermal behavior and thermal self-stability of microcavities,” *Optics Express* **12**, 4742–4750 (2004).
- [65] A. B. Matsko, A. A. Savchenkov, V. S. Ilchenko, D. Seidel, and L. Maleki, “Hard and soft excitation regimes of Kerr frequency combs,” *Physical Review A* **85**, 023830 (2012).
- [66] X. Xue, Y. Xuan, C. Wang, P.-H. Wang, Y. Liu, B. Niu, D. E. Leaird, M. Qi, and A. M. Weiner, “Thermal tuning of Kerr frequency combs in silicon nitride microring resonators,” *Optics Express* **24**, 687–698 (2016).
- [67] J. Jost, T. Herr, C. Lecaplain, V. Brasch, M. Pfeiffer, and T. Kippenberg, “Counting the cycles of light using a self-referenced optical microresonator,” *Optica* **2**, 706–711 (2015).
- [68] P. Del’Haye, A. Coillet, T. Fortier, K. Beha, D. C. Cole, K. Y. Yang, H. Lee, K. J. Vahala, S. B. Papp, and S. A. Diddams, “Phase-coherent microwave-to-optical link with a self-referenced microcomb,” *Nature Photonics* **10**, 516–520 (2016).
- [69] T. Ideguchi, S. Holzner, B. Bernhardt, G. Guelachvili, N. Picqué, and T. W. Hänsch, “Coherent Raman spectro-imaging with laser frequency combs,” *Nature* **502**, 355–358 (2013).
- [70] A. Schliesser, N. Picqué, and T. W. Hänsch, “Mid-infrared frequency combs,” *Nature Photonics* **6**, 440–449 (2012).

-
- [71] C. Lecaplain, C. Javerzac-Galy, M. Gorodetsky, and T. Kippenberg, “Mid-Infrared ultra-high- Q resonators based on fluoride crystalline materials,” *Nature Communication* **7**, 13383 (2016).
- [72] A. A. Savchenkov, V. S. Ilchenko, F. Di Teodoro, P. M. Belden, W. T. Lotshaw, A. B. Matsko, and L. Maleki, “Generation of Kerr combs centered at 4.5 μm in crystalline microresonators pumped with quantum-cascade lasers,” *Optics Letters* **40**, 3468–3471 (2015).
- [73] A. Savchenkov, A. Matsko, W. Liang, V. Ilchenko, D. Seidel, and L. Maleki, “Kerr combs with selectable central frequency,” *Nature Photonics* **5**, 293–296 (2011).
- [74] Y. Yang, X. Jiang, S. Kasumie, G. Zhao, L. Xu, J. M. Ward, L. Yang, and S. N. Chormaic, “Four-wave mixing parametric oscillation and frequency comb generation at visible wavelengths in a silica microbubble resonator,” *Optics Letters* **41**, 5266–5269 (2016).
- [75] P. Latawiec, V. Venkataraman, M. J. Burek, B. J. Hausmann, I. Bulu, and M. Lončar, “On-chip diamond Raman laser,” *Optica* **2**, 924–928 (2015).
- [76] C. Lecaplain, C. Javerzac-Galy, E. Lucas, J. D. Jost, and T. J. Kippenberg, “Quantum cascade laser Kerr frequency comb,” arXiv:1506.00626 (2015).
- [77] A. Matsko, A. Savchenkov, and L. Maleki, “Normal group-velocity dispersion Kerr frequency comb,” *Optics Letters* **37**, 43–45 (2012).
- [78] Y. Liu, Y. Xuan, X. Xue, P.-H. Wang, S. Chen, A. J. Metcalf, J. Wang, D. E. Leaird, M. Qi, and A. M. Weiner, “Investigation of mode coupling in normal-dispersion silicon nitride microresonators for Kerr frequency comb generation,” *Optica* **1**, 137–144 (2014).
- [79] S.-W. Huang, H. Zhou, J. Yang, J. McMillan, A. Matsko, M. Yu, D.-L. Kwong, L. Maleki, and C. Wong, “Mode-locked ultrashort pulse generation from on-chip normal dispersion microresonators,” *Physical Review Letters* **114**, 053901 (2015).
- [80] X. Xue, Y. Xuan, Y. Liu, P.-H. Wang, S. Chen, J. Wang, D. E. Leaird, M. Qi, and A. M. Weiner, “Mode-locked dark pulse Kerr combs in normal-dispersion microresonators,” *Nature Photonics* **9**, 594–600 (2015).
- [81] C. Godey, I. V. Balakireva, A. Coillet, and Y. K. Chembo, “Stability analysis of the spatiotemporal Lugiato-Lefever model for Kerr optical frequency combs in the anomalous and normal dispersion regimes,” *Physical Review A* **89**, 063814 (2014).
- [82] M.-G. Suh, Q.-F. Yang, K. Y. Yang, X. Yi, and K. J. Vahala, “Microresonator soliton dual-comb spectroscopy,” *Science* **354**, 600–603 (2016).
- [83] A. Coillet, I. Balakireva, R. Henriët, K. Saleh, L. Larger, J. M. Dudley, C. R. Menyuk, and Y. K. Chembo, “Azimuthal Turing patterns, bright and dark cavity solitons in Kerr combs generated with whispering-gallery-mode resonators,” *IEEE Photonics Journal* **5**, 6100409 (2013).
- [84] S. Coen and M. Erkintalo, “Universal scaling laws of Kerr frequency combs,” *Optics Letters* **38**, 1790–1792 (2013).
- [85] V. Brasch, M. Geiselmann, T. Herr, G. Lihachev, M. Pfeiffer, M. Gorodetsky, and T. Kippenberg, “Photonic chip-based optical frequency comb using soliton Cherenkov radiation,” *Science* **351**, 357–360 (2016).
- [86] Y. K. Chembo, I. S. Grudinin, and N. Yu, “Spatiotemporal dynamics of Kerr-Raman optical frequency combs,” *Physical Review A* **92**, 043818 (2015).
- [87] A. Matsko, A. Savchenkov, R. Letargat, V. Ilchenko, and L. Maleki, “On cavity modification of stimulated Raman scattering,” *Journal of Optics B: Quantum and Semiclassical Optics* **5**, 272 (2003).
- [88] I. S. Grudinin and L. Maleki, “Efficient Raman laser based on a CaF_2 resonator,” *Journal of the Optical Society of America B* **25**, 594–598 (2008).

Bibliography

- [89] B.-B. Li, Y.-F. Xiao, M.-Y. Yan, W. R. Clements, and Q. Gong, “Low-threshold Raman laser from an on-chip, high-Q, polymer-coated microcavity,” *Optics Letters* **38**, 1802–1804 (2013).
- [90] N. Deka, A. J. Maker, and A. M. Armani, “Titanium-enhanced Raman microcavity laser,” *Optics Letters* **39**, 1354–1357 (2014).
- [91] Y. Takahashi, Y. Inui, M. Chihara, T. Asano, R. Terawaki, and S. Noda, “A micrometre-scale Raman silicon laser with a microwatt threshold,” *Nature* **498**, 470–474 (2013).
- [92] F. Vanier, M. Rochette, N. Godbout, and Y.-A. Peter, “Raman lasing in As₂S₃ high-Q whispering gallery mode resonators,” *Optics Letters* **38**, 4966–4969 (2013).
- [93] H. Rong, S. Xu, O. Cohen, O. Raday, M. Lee, V. Sih, and M. Paniccia, “A cascaded silicon Raman laser,” *Nature Photonics* **2**, 170–174 (2008).
- [94] W. Liang, V. Ilchenko, A. Savchenkov, A. Matsko, D. Seidel, and L. Maleki, “Passively mode-locked Raman laser,” *Physical Review Letters* **105**, 143903 (2010).
- [95] G. Lin and Y. K. Chembo, “Phase-locking transition in Raman combs generated with whispering gallery mode resonators,” *Optics Letters* **41**, 3718–3721 (2016).
- [96] T. Lu, L. Yang, R. V. Van Loon, A. Polman, and K. J. Vahala, “On-chip green silica upconversion microlaser,” *Optics Letters* **34**, 482–484 (2009).
- [97] S. Mehrabani and A. M. Armani, “Blue upconversion laser based on thulium-doped silica microcavity,” *Optics Letters* **38**, 4346–4349 (2013).
- [98] S. Miller, K. Luke, Y. Okawachi, J. Cardenas, A. L. Gaeta, and M. Lipson, “On-chip frequency comb generation at visible wavelengths via simultaneous second- and third-order optical nonlinearities,” *Optics Express* **22**, 26517–26525 (2014).
- [99] H. Jung, R. Stoll, X. Guo, D. Fischer, and H. X. Tang, “Green, red, and IR frequency comb line generation from single IR pump in AlN microring resonator,” *Optica* **1**, 396–399 (2014).
- [100] D. Farnesi, A. Barucci, G. Righini, S. Berneschi, S. Soria, and G. N. Conti, “Optical frequency conversion in silica-whispering-gallery-mode microspherical resonators,” *Physical Review Letters* **112**, 093901 (2014).
- [101] J. Moore, M. Tomes, T. Carmon, and M. Jarrahi, “Continuous-wave cascaded-harmonic generation and multi-photon Raman lasing in lithium niobate whispering-gallery resonators,” *Applied Physics Letters* **99**, 221111 (2011).
- [102] H. A. Haus, *Waves and fields in optoelectronics* (Prentice-Hall, 1984).
- [103] C. Manolatou, M. Khan, S. Fan, P. R. Villeneuve, H. Haus, and J. Joannopoulos, “Coupling of modes analysis of resonant channel add-drop filters,” *IEEE Journal of Quantum Electronics* **35**, 1322–1331 (1999).
- [104] A. N. Oraevsky, “Whispering-gallery waves,” *Quantum Electronics* **32**, 377–400 (2002).
- [105] I. Agha, J. Sharping, M. Foster, and A. Gaeta, “Optimal sizes of silica microspheres for linear and nonlinear optical interactions,” *Applied Physics B* **83**, 303–309 (2006).
- [106] M. L. Gorodetsky and A. E. Fomin, “Geometrical theory of whispering-gallery modes,” *IEEE Journal of Selected Topics in Quantum Electronics* **12**, 33–39 (2006).
- [107] M. L. Gorodetsky and A. E. Fomin, “Eigenfrequencies and Q factor in the geometrical theory of whispering-gallery modes,” *Quantum Electronics* **37**, 167–172 (2007).
- [108] M. Oxborrow, “Traceable 2-D finite-element simulation of the whispering-gallery modes of axisymmetric electromagnetic resonators,” *IEEE Transactions on Microwave Theory and Techniques* **55**, 1209–1218 (2007).
- [109] X.-F. Jiang, Y.-F. Xiao, C.-L. Zou, L. He, C.-H. Dong, B.-B. Li, Y. Li, F.-W. Sun, L. Yang, and Q. Gong, “Highly unidirectional emission and ultralow-threshold lasing from on-chip ultrahigh- Q microcavities,” *Advanced Materials* **24**, 260–264 (2012).

-
- [110] J. Knight, G. Cheung, F. Jacques, and T. Birks, "Phase-matched excitation of whispering-gallery-mode resonances by a fiber taper," *Optics Letters* **22**, 1129–1131 (1997).
- [111] M. Cai, O. Painter, and K. J. Vahala, "Observation of critical coupling in a fiber taper to a silica-microsphere whispering-gallery mode system," *Physical Review Letters* **85**, 74 (2000).
- [112] S. Spillane, T. Kippenberg, O. Painter, and K. Vahala, "Ideality in a fiber-taper-coupled microresonator system for application to cavity quantum electrodynamics," *Physical Review Letters* **91**, 043902 (2003).
- [113] J. S. Levy, M. A. Foster, A. L. Gaeta, and M. Lipson, "Harmonic generation in silicon nitride ring resonators," *Optics Express* **19**, 11415–11421 (2011).
- [114] T. Carmon, S. Y. Wang, E. P. Ostby, and K. J. Vahala, "Wavelength-independent coupler from fiber to an on-chip cavity, demonstrated over an 850nm span," *Optics Express* **15**, 7677–7681 (2007).
- [115] D. Farnesi, A. Barucci, G. Righini, S. Berneschi, S. Soria, and G. N. Conti, "Optical frequency conversion in silica-whispering-gallery-mode microspherical resonators," *Physical Review Letters* **112**, 093901 (2014).
- [116] W. Yoshiki and T. Tanabe, "Analysis of bistable memory in silica toroid microcavity," *Journal of the Optical Society of America B* **29**, 3335–3343 (2012).
- [117] L. A. Lugiato and R. Lefever, "Spatial dissipative structures in passive optical systems," *Physical Review Letters* **58**, 2209 (1987).
- [118] T. Miyaji, I. Ohnishi, and Y. Tsutsumi, "Bifurcation analysis to the Lugiato–Lefever equation in one space dimension," *Physica D: Nonlinear Phenomena* **239**, 2066–2083 (2010).
- [119] M. Haelterman, S. Trillo, and S. Wabnitz, "Dissipative modulation instability in a nonlinear dispersive ring cavity," *Optics Communications* **91**, 401–407 (1992).
- [120] H. Lee, T. Chen, J. Li, K. Y. Yang, S. Jeon, O. Painter, and K. J. Vahala, "Chemically etched ultrahigh- Q wedge-resonator on a silicon chip," *Nature Photonics* **6**, 369–373 (2012).
- [121] L. Zhang, C. Bao, V. Singh, J. Mu, C. Yang, A. M. Agarwal, L. C. Kimerling, and J. Michel, "Generation of two-cycle pulses and octave-spanning frequency combs in a dispersion-flattened micro-resonator," *Optics Letters* **38**, 5122–5125 (2013).
- [122] Y. Okawachi, M. R. Lamont, K. Luke, D. O. Carvalho, M. Yu, M. Lipson, and A. L. Gaeta, "Bandwidth shaping of microresonator-based frequency combs via dispersion engineering," *Optics Letters* **39**, 3535–3538 (2014).
- [123] G. Lin and Y. K. Chembo, "On the dispersion management of fluorite whispering-gallery mode resonators for Kerr optical frequency comb generation in the telecom and mid-infrared range," *Optics Express* **23**, 1594–1604 (2015).
- [124] I. S. Grudin and N. Yu, "Dispersion engineering of crystalline resonators via microstructuring," *Optica* **2**, 221–224 (2015).
- [125] Y. Nakagawa, Y. Mizumoto, T. Kato, T. Kobatake, H. Itobe, Y. Kakinuma, and T. Tanabe, "Dispersion tailoring of a crystalline whispering gallery mode microcavity for a wide-spanning optical Kerr frequency comb," *Journal of the Optical Society of America B* **33**, 1913–1920 (2016).
- [126] K. Y. Yang, K. Beha, D. C. Cole, X. Yi, P. Del’Haye, H. Lee, J. Li, D. Y. Oh, S. A. Diddams, S. B. Papp, and K. J. Vahala, "Broadband dispersion-engineered microresonator on a chip," *Nature Photonics* **10**, 316–320 (2016).
- [127] I. Malitson, "Interspecimen Comparison of the Refractive Index of Fused Silica," *Journal of the Optical Society of America* **55**, 1205–1209 (1965).
- [128] H. Gibbs, S. McCall, and T. Venkatesan, "Differential gain and bistability using a sodium-filled Fabry-Perot interferometer," *Physical Review Letters* **36**, 1135 (1976).

Bibliography

- [129] F. Leo, S. Coen, P. Kockaert, S.-P. Gorza, P. Emplit, and M. Haelterman, “Temporal cavity solitons in one-dimensional Kerr media as bits in an all-optical buffer,” *Nature Photonics* **4**, 471–476 (2010).
- [130] F. Leo, L. Gelens, P. Emplit, M. Haelterman, and S. Coen, “Dynamics of one-dimensional Kerr cavity solitons,” *Optics Express* **21**, 9180–9191 (2013).
- [131] M. Karpov, H. Guo, A. Kordts, V. Brasch, M. H. Pfeiffer, M. Zervas, M. Geiselmann, and T. J. Kippenberg, “Raman self-frequency shift of dissipative Kerr solitons in an optical microresonator,” *Physical Review Letters* **116**, 103902 (2016).
- [132] M. Haelterman, S. Trillo, and S. Wabnitz, “Additive-modulation-instability ring laser in the normal dispersion regime of a fiber,” *Optics Letters* **17**, 745–747 (1992).
- [133] V. Torres-Company, D. CastellÃş-Lurbe, and E. Silvestre, “Comparative analysis of spectral coherence in microresonator frequency combs,” *Optics Express* **22**, 4678–4691 (2014).
- [134] B. Min, L. Yang, and K. Vahala, “Controlled transition between parametric and Raman oscillations in ultrahigh- Q silica toroidal microcavities,” *Applied Physics Letters* **87**, 181109 (2005).
- [135] R. H. Stolen, W. Tomlinson, H. Haus, and J. Gordon, “Raman response function of silica-core fibers,” *Journal of the Optical Society of America B* **6**, 1159–1166 (1989).
- [136] D. Hollenbeck and C. D. Cantrell, “Multiple-vibrational-mode model for fiber-optic Raman gain spectrum and response function,” *Journal of the Optical Society of America B* **19**, 2886–2892 (2002).
- [137] Q.-F. Yang, X. Yi, K. Y. Yang, and K. Vahala, “Stokes solitons in optical microcavities,” *Nature Physics* **13**, 53–57 (2017).
- [138] Q. Lin and G. P. Agrawal, “Raman response function for silica fibers,” *Optics Letters* **31**, 3086–3088 (2006).
- [139] F. Leo, T. Hansson, I. Ricciardi, M. De Rosa, S. Coen, S. Wabnitz, and M. Erkintalo, “Frequency-comb formation in doubly resonant second-harmonic generation,” *Physical Review A* **93**, 043831 (2016).
- [140] I. Agha, M. Davanço, B. Thurston, and K. Srinivasan, “Low-noise chip-based frequency conversion by four-wave-mixing Bragg scattering in SiN_x waveguides,” *Optics Letters* **37**, 2997–2999 (2012).
- [141] N. Akhmediev and M. Karlsson, “Cherenkov radiation emitted by solitons in optical fibers,” *Physical Review A* **51**, 2602 (1995).
- [142] X. Zhang and A. M. Armani, “Silica microtoroid resonator sensor with monolithically integrated waveguides,” *Optics Express* **21**, 23592–23603 (2013).
- [143] H. Seidel, L. Csepregi, A. Heuberger, and H. Baumgärtel, “Anisotropic etching of crystalline silicon in alkaline solutions I. Orientation dependence and behavior of passivation layers,” *Journal of the Electrochemical Society* **137**, 3612–3626 (1990).
- [144] B. E. Little, J.-P. Laine, and H. A. Haus, “Analytic theory of coupling from tapered fibers and half-blocks into microsphere resonators,” *Journal of Lightwave Technology* **17**, 704 (1999).
- [145] V. Datsyuk, “Some characteristics of resonant electromagnetic modes in a dielectric sphere,” *Applied Physics B* **54**, 184–187 (1992).
- [146] S. Schiller, “Asymptotic expansion of morphological resonance frequencies in Mie scattering,” *Applied Optics* **32**, 2181–2185 (1993).
- [147] T. J. A. Kippenberg, “Nonlinear optics in ultra-high- Q whispering-gallery optical microcavities,” Ph.D. thesis, California Institute of Technology (2004).

- [148] J. Hult, "A fourth-order Runge–Kutta in the interaction picture method for simulating supercontinuum generation in optical fibers," *Journal of Lightwave Technology* **25**, 3770–3775 (2007).
- [149] W. J. Firth and G. K. Harkness, "Cavity Solitons," *Asian Journal of Physics* **7**, 665–677 (1998).